The velocity and magnetic field fluctuations of the solar wind at 1 AU: Statistical analysis of Fourier spectra and correlations with plasma properties

Joseph E. Borovsky[1,2]

Received 29 December 2011; revised 11 March 2012; accepted 2 April 2012; published 26 May 2012.

[1] Ten years of ACE plasma and magnetic field measurements are divided into 20,076 subintervals that are 4.55 h long. Each subinterval is Fourier analyzed resulting in a statistical ensemble of 20,076 realizations of the solar wind and its "turbulence." Oxygen charge-state ratios are used to categorize each subinterval as coronal-hole-origin plasma, non-coronal-hole-origin plasma, or ejecta. A number of known properties of the solar wind $\underline{v}$ and $\underline{B}$ fluctuations are statistically confirmed and new informatin as functions of the type of plasma is obtained. For the fluctuations it is found that the coronal-hole-origin versus non-coronal-hole-origin classification is more fundamental than a fast-wind versus slow-wind classification. In the frequency range 4.3×10^{-4}–1.9×10^{-3} Hz, the ensemble the mean spectral indices of the magnetic field, velocity, and total energy are -1.62, -1.41, and -1.52, however the spectral indices vary with changes in the type of plasma. The number of strong current sheets in each subinterval is recorded. The fluctuation amplitudes, Alfvén ratios, and outward-inward Elsasser ratios are all strongly correlated with the properties of the plasma and the density of current sheets. Regions wherein the fluctuation spectra are shallowest correspond to coronal-hole plasma; regions wherein the spectra are steepest correspond to non-coronal-hole plasma and ejecta. The autocorrelation times for the spectral indices and amplitudes are 20–30 h, similar to the autocorrelation times for the proton specific entropy, the carbon charge-state ratio, the density of strong current sheets, and the classification of plasma. Analysis is performed to interpret ensembles of spectra with variance error.

Citation: Borovsky, J. E. (2012), The velocity and magnetic field fluctuations of the solar wind at 1 AU: Statistical analysis of Fourier spectra and correlations with plasma properties, *J. Geophys. Res.*, *117*, A05104, doi:10.1029/2011JA017499.

1. Introduction

[2] The fluctuations $\delta\underline{v}$ and $\delta\underline{B}$ of the magnetic field $\underline{B}$ and plasma flow velocity $\underline{v}$ measured by a spacecraft in the solar wind are produced by a mix of MHD turbulence, current sheets, pressure-balanced structures, plasma blobs, magnetic holes, inhomogeneities, etc. From day to day or even from hour to hour different types of solar wind plasma pass the spacecraft.

[3] Although their amplitudes are similar, the statistics of the $\delta\underline{v}$ fluctuations differ from the statistics of the $\delta\underline{B}$ fluctuations. In Figure 1 a comparison of velocity $\underline{v}$ and magnetic field $\underline{B}$ hodograms for the solar wind shows this difference. The hodograms are constructed from 8 days of measurements by ACE. Figure 1 is a double slice through a three-dimensional velocity hodogram (Figure 1, left) (constructed by plotting v_t versus v_n in blue for -5 km/s $\le (v_r - \langle v_r \rangle) \le +5$ km/s and plotting $(v_r - \langle v_r \rangle)$ versus v_n in red for -5 km/s $\le v_t \le +5$ km/s) and a slice through a three-dimensional magnetic field hodogram (Figure 1, right) (constructed by plotting B_t versus B_n in blue for -2 nT $\le B_r \le +2$ nT and plotting B_r versus B_n in red for -2 nT $\le B_t \le +2$ nT). As can be seen, the hodogram of $\underline{B}$ vectors forms a shell (with radius $|\underline{B}|$) and the hodogram of $\underline{v}$ vectors forms a solid sphere (with radius $\langle \delta\underline{v} \rangle$). (Note that there is a shift in the value of $|B|$ during the time series which results in a double shell.)

[4] Studies of solar wind fluctuations tend to utilize magnetic field measurements because they have higher time resolution (yielding a larger dynamic range of frequencies) and are less subject to noise [e.g., *Johnstone and Krauklis*, 1998; *Borovsky et al.*, 1997].

[5] It is important to know both the properties of the velocity fluctuations $\delta\underline{v}$ and the properties of the magnetic field fluctuations $\delta\underline{B}$. Three examples are as follows: (1) To calculate the eddy viscosity and other turbulent-transport coefficients in MHD, knowledge of both $\delta\underline{v}$ and $\delta\underline{B}$ is required [*Hamba*, 1992; *Yoshizawa and Yokoi*, 1996; *Borovsky*, 2006]. (2) To understand turbulent-dynamo

[1]AOSS Department, University of Michigan, Ann Arbor, Michigan, USA.
[2]Space Science Institute, Boulder, Colorado, USA.

Corresponding author: J. E. Borovsky, AOSS Department, University of Michigan, Ann Arbor, MI 48109, USA. (borovsky@umich.edu)

0148-0227/12/2011JA017499

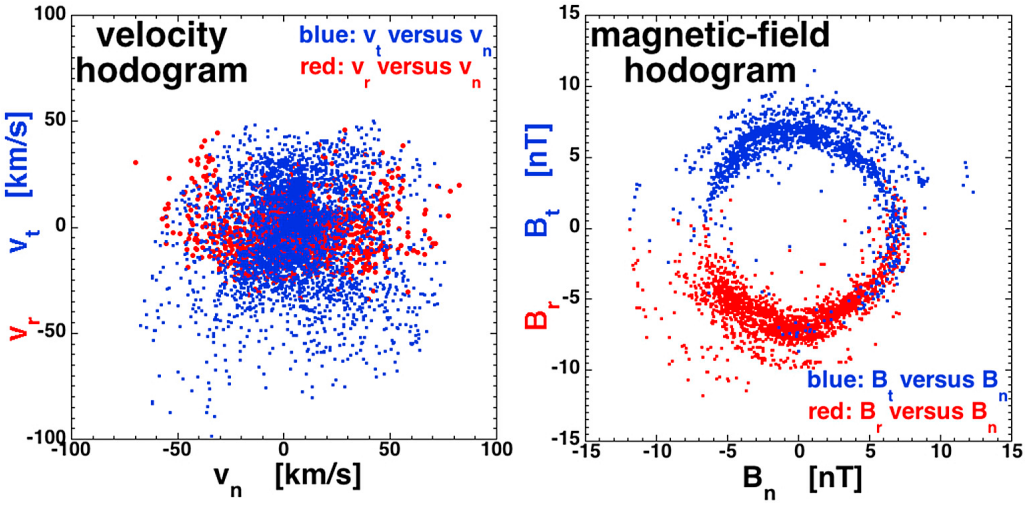

Figure 1. Using 8 days of measurements (February 4–11, 2003) from (left) ACE SWEPAM and from (right) ACE MAG, slices through 3-dimensional hodograms are created. The velocity hodogram (left) is constructed by plotting v_t versus v_n (black points) for -5 km/s $\le (v_r - \langle v_r \rangle) \le +5$ km/s and plotting $(v_r - \langle v_r \rangle)$ versus v_n (red points) for -5 km/s $\le v_t \le +5$ km/s and the magnetic field hodogram (right) is constructed by plotting B_t versus B_n (black points) for -2 nT $\le B_r \le +2$ nT and plotting B_r versus B_n (red points) for -2 nT $\le B_t \le +2$ nT.

processes, wherein there is an unbalanced exchange of energy between the velocity fluctuations and the field fluctuations, both $\delta\underline{v}$ and $\delta\underline{B}$ must the characterized at all frequencies [*Hamba*, 1992; *Mininni et al.*, 2005]. (3) For basic tests of MHD-turbulence theories, the total-energy spectrum must be obtained, which requires both $\delta\underline{v}$ and $\delta\underline{B}$ to be utilized. Additionally, near boundaries in the solar wind (such as plasma interfaces or fossil current sheets) boundary conditions on $\underline{v}$ and $\delta\underline{v}$ may differ from boundary conditions on $\underline{B}$ and $\delta\underline{B}$.

[6] The analysis of this paper breaks the 1998–2008 ACE data set into 20,094 non-overlapping data subintervals that are each 4.55 h long. The velocity and magnetic field in each subinterval are separately analyzed by Fourier techniques and the ensembles of output parameters are statistically analyzed. Working with ensembles of short time intervals allows the reaction of the turbulence to variations in the solar wind properties to be studied; however power spectral densities calculated from finite time intervals have "variance error" and the effects of the variance error must be carefully considered. Through the use of controlled numerical experiments Appendix A describes the interpretation of ensembles of spectra with variance error. To check the validity of the ensemble results, comparisons will be made with the analysis of time long intervals.

[7] The solar wind at 1 AU is typically categorized as slow wind versus fast wind versus ejecta [e.g., *Ruzmaikin et al.*, 1997; *Manoharan et al.*, 2000; *Li*, 2007; *Yordanova et al.*, 2009; *Tessein et al.*, 2009]. Here a categorization of the solar wind as to the region of origin on the Sun will be used: coronal-hole-origin plasma versus non-coronal-hole-origin (streamer-belt) plasma versus ejecta. This categorization is made by inferring the coronal temperature from measurements of heavy-ion charge-state ratios in the wind [cf. *Geiss et al.*, 1995; *Zurbuchen et al.*, 2002; *Zhao et al.*, 2009; *von Steiger et al.*, 2010].

[8] This manuscript is organized as follows. In section 2 the data sets employed and data-analysis methods used are described. section 3 contains a study of strong current sheets (directional discontinuities) in the solar wind; data subintervals without strong current sheets are the cleanest for the study of non-discontinuity fluctuations, however selecting strong-current-sheet-free intervals skews the data selection strongly to coronal mass ejections and non-coronal-hole-origin plasma. In section 4 the spectral indices of the velocity, magnetic field, and total energy are examined in relation to the properties of the solar wind and the type of wind; spectral indices for inward and outward Elsasser variables are also examined. In section 5 the fluctuation amplitudes of the velocity, magnetic field, total energy, and inward and outward Elsasser variables are examined in relation to the properties of the solar wind and the type of wind; additionally the Alfvén ratio and outward-inward imbalance of the fluctuations are examined. Section 6 contains discussions about (1) the variability of the spectral indices of the solar wind, (2) the systematic difference between the velocity and magnetic field spectral indices, (3) comparing the measured total-energy spectral index to expectations from turbulence theories, and (4) future work that is needed. The results of this study are summarized in section 7. In Appendix A numerical experiments are performed to learn how to interpret the ensembles of spectral-index measurements from the ACE spectra with variance errors. Appendix B contains a discussion of the merits of data-tapering windows for Fourier-transform analysis of the ACE measurements.

2. Data Methodology

[9] Merged 64-s-resolution magnetic field and plasma measurements from the ACE spacecraft upstream from the Earth are used to analyze the MHD fluctuations of the solar

Table 1. Using the *Zhao et al.* [2009] Scheme to Categorize the Wind From the ACE SWICS Measurements of the O^{7+}/O^{6+} Charge-State Ratio[a]

	Coronal-Hole-Origin Plasma	Non-Coronal-Hole-Origin Plasma	CME Plasma
All data subintervals	48.8%	43.1%	8.1%
$N_d = 0$ subintervals	10.4%	63.1%	26.5%
Sustained shallow slopes	85.8%	8.3%	5.9%
Sustained steep slopes	21.2%	65.5%	13.3%

[a]The occurrence rate of the three types of plasma are displayed.

wind. The magnetic field measurements are from the MAG instrument [*Smith et al.*, 1998] and the plasma measurements are from the SWEPAM instrument [*McComas et al.*, 1998]. The focus of the analysis is on fluctuations of the plasma flow velocity $\underline{v}$, the magnetic field vector $\underline{B}$, the magnetic field $\underline{b} = \underline{B}/(4\pi m_i n)^{1/2}$ measured in Alfvén units where n is the 64-s resolution plasma number density, and the two Elsasser variables $\underline{z}^+ = \underline{v} + \underline{b}$ and $\underline{z}^- = \underline{v} - \underline{b}$. Data from the SWICS mass-spectrometer [*Gloeckler et al.*, 1998] onboard ACE will also be used to determine coronal-hole-origin solar wind from non-coronal-hole-origin solar wind (see below).

[10] The February 1998 – July 2008 ACE data set is broken into 20,094 non-overlapping 4.55-h-long subintervals and each subinterval is analyzed separately. A 4.55-h subinterval consists of 256 measurements separated by 64 s, which is the time resolution of the SWEPAM plasma instrument on ACE. Since 256 is a power of 2, using data records that are 256 points long makes for efficient and accurate (no leakage) Fourier transforms. The subinterval length of 4.55 h is comparable to the correlation time of the solar wind magnetic field fluctuations, which is 0.7–4 h [*Matthaeus and Goldstein*, 1982; *Tu and Marsch*, 1995b; *Matthaeus et al.*, 1999; *Feynman et al.*, 1996; *Wicks et al.*, 2010], and shorter than the correlation time for the solar wind velocity fluctuations [*Matthaeus and Goldstein*, 1982; *Wicks et al.*, 2010]. The 4.55 h is somewhat shorter than the 5–40 h autocorrelation times for the properties of the solar wind plasma [cf. *Borovsky et al.*, 1998, Figure 6; *Borovsky and Funsten*, 2003a, Figure 12] and also shorter than the 27-h autocorrelation time of the coronal-hole versus non-coronal-hole typing of the wind (cf. section 5.4) so that the individual Fourier transforms do not tend to contain mixtures of fluctuations from different plasmas. As will be seen in section 5 the 4.55 h is somewhat shorter than the 10–40 h correlation time for the amplitude of the solar wind fluctuations, so the individual Fourier transforms tend not to mix measurements from different realizations of the solar wind fluctuations [cf. *Borovsky et al.*, 1997, section 2.2].

[11] Data dropouts in the ACE magnetic field and plasma measurements are replaced by linear interpolation across the data gap. A record is kept of which subintervals have magnetic field-data replacements and which subintervals have plasma-data replacements. If 20 or more data points in a 256-point subinterval need to be replaced by interpolation, that subinterval is not analyzed. Eliminating subintervals with 20 or more missing data points leaves 15,472 subintervals analyzed for the velocity fluctuations and 20,076 data intervals analyzed for magnetic field fluctuations.

[12] Each data subinterval is detrended prior to analysis. The detrending of the time-dependent data f(t) is done by subtracting a line from f(t) where the line goes through the endpoints $f(t_{min})$ and $f(t_{max})$ of the subinterval; the line is $f(t_{min}) + (t - t_{min})(f(t_{max}) - f(t_{min}))$. The detrending eliminates the jump in the data when the ends of the subinterval are joined by the assumption of periodicity in the Fourier analysis. (Cf. *Fougere* [1985] where the technique is called "end matching.") In Appendix B the analysis of the ACE data using linear detrending is compared with analysis using tapering windows: both methods yield very similar results but the tapering windows weaken the signal to noise in the Fourier spectra and increase the statistical error of ensemble averages.

[13] Each data subinterval is analyzed separately with an automated algorithm and the resulting parameters for the ensemble of subintervals are then statistically analyzed. Also, ensemble-averaged spectra are created and analyzed.

[14] To obtain power spectral densities (PSDs) of the detrended turbulent fluctuations, standard fast-Fourier-transform (FFT) methods (periodograms) are used [*Cooley and Tukey*, 1965; *Otnes and Enochson*, 1972]. The data in each subinterval is detrended by subtracting a line; no windowing or band-pass filtering is used prior to analysis (see the analysis of Appendix B on this issue). Spectral indices for each data subinterval are obtained by taking the slopes of lines fit to the PSDs via least squares linear regression in $\log_{10}$(PSD)-versus-$\log_{10}$(f) space. The least squares fitting methods are analyzed in Appendix A.

[15] In this report, most of the analysis will be focused on the frequency range 4.3×10^{-4}–1.9×10^{-3} Hz: this range is in the lower-frequency portion of the inertial subrange of the solar wind. The lower limit 4.3×10^{-4} Hz (39 min) of this frequency range is chosen to be shorter than the reported correlation times of the solar wind fluctuations, which are 0.7–4 h [*Matthaeus and Goldstein*, 1982; *Tu and Marsch*, 1995b; *Matthaeus et al.*, 1999; *Feynman et al.*, 1996]. The upper limit 1.9×10^{-3} Hz (8.5 min) of this frequency range is chosen to stay a factor of 4 away from the Nyquist frequency of the data, which for 64-s data resolution is 7.8×10^{-3} Hz. Note that in the fast wind at 1 AU the roll-over in the magnetic field spectrum between the Kolmogorov-like power law and the 1/f-like power law can be in the vicinity of 10^{-3} Hz [cf. *Roberts*, 2010, Figure 4], which is within the spectral window analyzed here. In section 4 some turbulence spectra will also be analyzed over the range 1.8×10^{-4}–3.9×10^{-3} Hz, which will encroach further on both the correlation time and on the Nyquist frequency.

[16] For each subinterval, the plasma type is categorized as coronal-hole origin, non-coronal-hole origin, ejecta, or unspecified. Using the formulas given by *Zhao et al.* [2009, Table 2], the O^{7+}/O^{6+} charge-state ratio measured by the SWICS instrument onboard ACE along with the solar wind velocity measured by SWEPAM are used to make the categorization. One-hour-averaged measurements are used to determine a "type" of wind every hour: if no high-quality O^{7+}/O^{6+} measurement is available, no type is assigned to the hour. For each 4.55-h data subinterval analyzed, the 5 h of typing are inspected. If all five hours are typed and if all 5 h are of the same type, then the 4.55-h subinterval is typed. If all 5 h are not all of the same type, then no type is assigned to that 4.55-h subinterval. 9469 intervals (out of a possible 20,076) satisfy the criteria and receive a type. There are 4617 subintervals assigned as "coronal-hole-origin wind"

(48.7%), 4089 assigned as "non-coronal-hole-origin wind" (43.2%), and 763 assigned as "CME" (8.1%). These fractions are entered into the top row of Table 1.

3. Current Sheets in the Solar Wind

[17] In addition to the turbulent fluctuations, sudden strong jumps in the magnetic field direction and/or magnetic field strength are found in the solar wind. It is not known whether these current sheets are part of the turbulence [e.g., *Greco et al.*, 2010] or something additional [e.g., *Borovsky and Denton*, 2011] (cf. section 6.4). The strong current sheets take the forms of rotational discontinuities or tangential discontinuities [*Burlaga*, 1968; *Turner and Siscoe*, 1971]. Older analyses using the minimum-variance-analysis technique estimated that rotational discontinuities were more common than tangential discontinuities [*Mariani et al.*, 1973, 1983; *Neugebauer et al.*, 1984; *Neugebauer and Alexander*, 1991; *Tsurutani and Ho*, 1999], although the minimum-variance-analysis technique is problematic [*Hausman et al.*, 2004]; more-recent analyses find that the solar wind discontinuities are predominantly tangential discontinuities [*Horbury et al.*, 2001; *Knetter et al.*, 2003, 2004; *Riazantseva et al.* 2005a, 2005b; *Burlaga*, 1971]. Strong current sheets are often accompanied by changes in the solar wind plasma properties [*Burlaga*, 1969; *Riazantseva et al.*, 2005a; *Borovsky*, 2008, 2010b, 2012a], indicating that the current sheets can be boundaries between different parcels of plasma. The current sheets are usually accompanied by strong flow shear [*Borovsky*, 2008, 2012b]. The measured thicknesses of strong (large-rotation-angle) current sheets in the solar wind at 1 AU vary from 10^3–10^5 km [*Siscoe et al.*, 1968; *Vasquez et al.*, 2007], which are in the MHD range of scale size factors of 10–100 times larger than the ion-inertial length in the solar wind.

[18] High-time-resolution measurements indicate that there are two populations of discontinuities [*Vasquez et al.*, 2007; *Neugebauer and Giacalone*, 2010]: a population of weak discontinuities and a population of strong discontinuities. The population of strong discontinuities is of interest here owing to the contribution that they make to the Fourier spectrum in the inertial subrange of frequencies [*Siscoe et al.*, 1968; *Sari and Ness*, 1969; *Borovsky*, 2010a; *Miao et al.*, 2011]. In a Fourier transform of the time series, the magnetic field and velocity jumps of the discontinuities produce strong signals with frequencies corresponding to the waiting times between jumps. (The waiting time between jumps contributes strongly to the persistence in the autocorrelation function and the Fourier transform of the autocorrelation function is the PSD.) The time interval between the passages of subsequent strong solar wind discontinuities varies from seconds to hours [e.g., *Siscoe et al.*, 1968; *Burlaga*, 1969; *Borovsky*, 2008].

[19] Current sheets are strong contributors to the intermittency of the solar wind magnetic field and velocity time series [cf. *Veltri*, 1999; *Bruno et al.*, 2001; *Mangeney et al.*, 2001; *Pallocchia et al.*, 2002]. *Li et al.* [2011] have argued that the presence of current sheets transforms magnetic field spectra from the Kraichnan $k^{-3/2}$ range to the Kolmogorov $k^{-5/3}$ range. *Borovsky and Denton* [2010] found that the strong current sheets make a significant contribution to the Alfvénicity of the solar wind.

[20] For these reasons, information will be gathered about the presence or absence of strong current sheets in the data subintervals analyzed in this study. Strong current sheets in the solar wind are found by looking for rapid, large changes in the direction of the magnetic field. To mark strong current sheets in the solar wind in the ACE data set, the direction of the magnetic field vector is noted every 64 s and if the angular change $\Delta\theta$ of the vector is greater than 45° in 128 s a current sheet is tallied. (This criterion is similar to those used by *Burlaga et al.* [1977] and by *Tsurutani and Smith* [1979] to gather their collections of solar wind discontinuities.) A mathematical assessment of this method of identifying current sheets can be found in *Li* [2007, 2008] (see also *Li et al.* [2008] and *Miao et al.* [2011]). To avoid counting multiple discontinuities separately, if directional discontinuities are less than 3 min apart they are counted as one discontinuity (as in *Tsurutani and Smith* [1979]).

[21] A parameter of particular interest is N_d, the number of strong ($\Delta\theta > 45°$) current sheets in a 4.55-h subinterval of solar wind data. Times when $N_d = 0$ are of particular interest since they offer an opportunity to analyze solar wind fluctuations that are not dominated by the strong spectral signal of the discontinuities. However, times when N_d has a low value are statistically associated with slow wind with an overemphasis on ejecta. As noted in Table 1, for all of the 4.55-h data subintervals that are typed with the O^{7+}/O^{6+} charge-state ratio 43.2% are non-coronal-hole origin, 48.7% are coronal-hole origin, and 8.1% are CME whereas for the $N_d = 0$ data subintervals 63.1% are non-coronal-hole origin, 10.4% are coronal-hole origin, and 26.5% are CME. The CME to non-coronal-hole ratio for all intervals (row 1) is 1/5.3 whereas the CME to non-coronal-hole ratio for the $N_d = 0$ intervals (row 2) is 1/2.4, an emphasis on ejecta.

[22] In Table 2 the Pearson's linear correlation coefficient R_{corr} (the covariance divided by the standard deviations [cf. *Bevington and Robinson*, 1992, equation (11.17)]) between various solar wind parameters are calculated and collected for the 1998–2008 ACE data set. The plasma properties are averages over the 4.55 h of each subinterval. As can be seen v_{sw} and T_p are strongly positively correlated with each other and those three parameters are anticorrelated with n. The quantities n and B are positively correlated with each other. The positive correlations between v_{sw} and T_p are well known [e.g., *Lopez*, 1987; *Richardson and Cane*, 1995; *Elliott et al.*, 2005; *Borovsky and Steinberg*, 2006a]; the anticorrelation between n and v_{sw} (or T_p) has been discussed [e.g., *Burlaga and Ogilvie*, 1970; *Zank et al.*, 1990]; and the positive correlation between n and B has been explained [*Malara et al.*, 1997]. As seen in Table 2, the logarithms of the proton specific entropy $\log(S_p)$ and the alpha-particle specific entropy $\log(S_\alpha)$ (where $S = T/n^{2/3}$ [cf. *Schindler and Birn*, 1978]) correlate positively with v_{sw} and T_p and negatively with n and B. The carbon and oxygen charge-state ratios C^{6+}/C^{5+} and O^{7+}/O^{6+} and the iron-to-oxygen density ratio Fe/O are all negatively correlated with v_{sw}, T_p, S_p and S_α and positively with B. The anticorrelation of S_p with the O^{7+}/O^{6+} ratio has been examined previously [*Pagel et al.*, 2004].

[23] Table 2 contains the linear correlation coefficients R_{corr} between the number of strong current sheets per data subinterval N_d and various properties of the solar wind plasma. As can be seen, N_d increases as the wind velocity v_{sw} and proton temperature T_p increase. The positive correlation

Table 2. Linear Correlation Coefficients R_{corr} (in Percent) Between Various Solar Wind Parameters

	v_{sw}	n	T_p	B	$\log(S_p)$	$\log(S_\alpha)$	$\log(\beta_p)$	v_A	N_d	$\log(C^6/C^5)$	$\log(O^7/O^6)$	Fe/O
v_{sw}	+100	−36	+71	+5	+72	+76	+16	+35	+48	−50	−59	−36
n	−36	+100	−15	+48	−55	−45	+6	−18	−8	+25	+19	+20
T_p	+71	−15	+100	+21	+80	+71	+37	+33	−50	−55	−46	−38
B	+5	+48	+21	+100	−10	+1	−48	+61	−16	+22	+13	+23
$\log(S_p)$	+72	−55	+80	−10	+100	+85	+34	+34	+45	−63	−48	−44
$\log(S_\alpha)$	+76	−45	+71	+1	+85	+100	+16	+43	+33	−53	−44	−29
$\log(\beta_p)$	+16	+6	+37	−48	+34	+16	+100	−63	+53	−50	−32	−51
v_A	+35	−18	+33	+61	+34	+43	−63	+100	−13	+8	−3	+17
N_d	+48	−8	+50	−16	+45	+33	+53	−13	+100	−52	−43	−39
$\log(C^6/C^5)$	−50	+25	−55	+22	−63	−53	−50	+8	−52	+100	+77	+51
$\log(O^7/O^6)$	−59	+19	−46	+13	−48	−44	−32	−3	−43	+77	+100	+33
Fe/O	−36	+20	−38	+23	−44	−29	−51	+17	−39	+51	+33	+100

of N_d with v_{sw} has been noted previously [e.g., *Borovsky*, 2008; *Borovsky and Denton*, 2010]. N_d is also positively correlated with S_p and β_p: these correlations are consistent with low numbers of strong current sheets occurring in ejecta plasmas. N_d is strongly negatively correlated with the charge-state ratios C^{6+}/C^{5+} and O^{7+}/O^{6+}: these correlations are consistent with low numbers of strong current sheets occurring in non-coronal-hole plasmas. These systematic variations of the number of strong current sheets in the solar wind with the parameters of the solar wind will complicate any analysis of solar wind turbulence as functions of the type of wind or as functions of the parameters of the solar wind.

4. Spectral Indices

[24] For each of the 256-point data subintervals, fast Fourier transforms are applied to the parameters v_r, v_t, v_n, B_r, B_t, B_n, b_r, b_t, and b_n. The power-spectral density (periodogram) P of each subinterval is obtained from the fast-Fourier transform FFT via $P(v) = 2\Delta t/N\{[FFT(v_r)]^2 + [FFT(v_t)]^2 + [FFT(v_n)]^2\}$, $P(B) = 2\Delta t/N\{[FFT(B_r)]^2 + [FFT(B_t)]^2 + [FFT(B_n)]^2\}$, and $P(b) = 2\Delta t/N\{[FFT(b_r)]^2 + [FFT(b_t)]^2 + [FFT(b_n)]^2\}$ [cf. *Otnes and Enochson*, 1972, equation (5.6)], where $\Delta t = 64$ s is the data time resolution and $N = 256$ is the number of data points in a Fourier transform. For the power spectral densities P(f), least squares linear-regression fits in $\log_{10}(P)$ versus $\log_{10}(f)$ are made in the frequency range 4.3×10^{-4} Hz $\le f \le 1.9 \times 10^{-3}$ Hz and the spectral slopes $d\log_{10}(P)/d\log_{10}(f)$ of the fits are recorded.

4.1. General Statistics and Solar-Cycle Dependence of the Spectral Indices

[25] In Figure 2 the spectral index of the magnetic field B power spectral density (blue points) and of the velocity v power spectral density (red points) are plotted as a function of time for 10.5 years. 54-day running averages of the v and B spectral indices are shown along with a 54-day running average of the total-energy E spectral indices; this 54-day average is twice the 27-day solar rotation. Notice that the spectral index of the velocity is consistently lower in magnitude (shallower) than the spectral index of the magnetic field, and notice that the spectral index for the total energy is

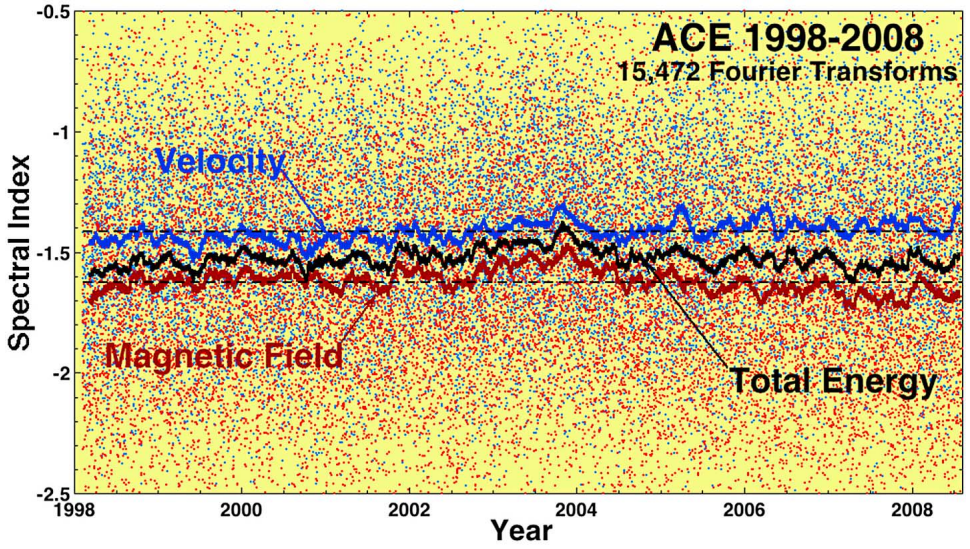

Figure 2. For the years 1998–2008 the spectral indices of the velocity (blue points) and magnetic field (red points) are plotted as functions of time. Each pair of points is from one 4.55-h subinterval of ACE measurements. 13.5-day running averages of the spectral indices of the velocity (dark blue), the magnetic field (dark red), and the total energy (black) are also plotted.

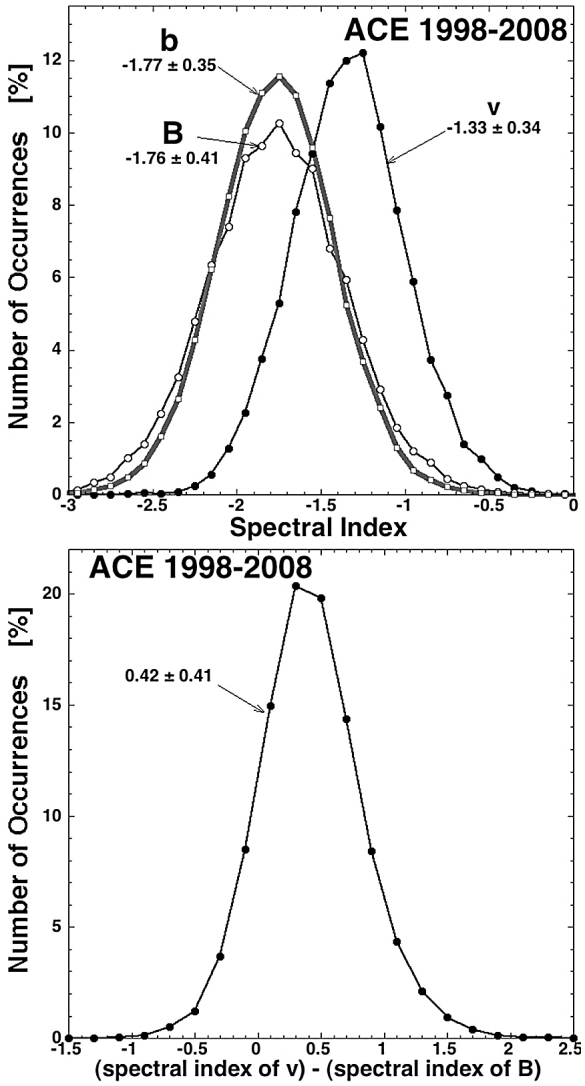

Figure 3. (top) For the 1998–2008 ACE measurements, the spectral indices of the magnetic field PSDs and the velocity PSDs are binned (black curves) as are the spectral indices of the PSDs of the magnetic field b in Alfvén units (gray curve). (bottom) For the 1998–2008 ACE measurements, the differences of the spectral indices of the velocity v and magnetic field b for every 4.55-h subinterval are binned.

between the two. For the v and B spectral indices, the mean values of −1.41 and −1.62 are denoted with horizontal black dashed lines. A slight solar-cycle dependence of the magnetic field spectral index can be seen in Figure 2 where the index is shallower than average in the year 2003 and steeper than average in the years 2007 and 2008. The year 2003 had robust high-speed streams at ACE [*Tripathi et al.*, 2007] and the years 2007 and 2008 had weaker (lower velocity) high-speed streams at ACE [*Denton and Borovsky*, 2011].

[26] The spectral indices of the magnetic field B power spectral density and the velocity v power spectral density are binned for the 1998–2008 ACE measurements and their occurrence distributions are plotted in Figure 3 (top). Also shown is the occurrence distribution of the spectral index of the power spectral density of $\underline{b} = \underline{B}/(4\pi n m_i)^{1/2}$. The shapes of the occurrence distributions are similar, but the velocity spectral index is systematically shallower than the magnetic field spectral index. The ensemble of the magnetic field B spectral indices yields −1.62 ± 0.49 (mean ± standard deviation), the ensemble of the magnetic field b spectral indices yields −1.62 ± 0.39, and the ensemble of the velocity v spectral indices yields −1.41 ± 0.39. These spectral-index values are entered into Table 3. There is a strong positive correlation between the spectral index of b and the spectral index of v ($R_{corr} = +0.45$); when the index of v is steeper than average the index of b tends to be steeper than average, etc.

[27] It has been pointed out to the author (A. Roberts, personal communication, 2012) that the spectral index of the magnetic field may be too shallow owing to the spectral range chosen for the fits, wherein the spectral breakpoint encroaches in the fitting range for fast wind. A magnetic field spectral index close to −1.66 might be expected.

[28] To underpin the statistical analysis of ensembles of spectra, mathematical experiments are performed in Appendix A to mimic and statistically analyze the ACE spectra with inherent variance errors. It is concluded in Appendix A that (1) the mean value of the ensemble of spectral indices is the most-accurate value of the spectral index underlying the "variance error" in the periodograms, (2) the value of the mean spectral index is known much more accurately than the standard deviation of the ensemble of spectral indices, and (3) any attempt to improve the statistical measurement of the spectral index by selecting only fits to the spectra that have high correlation coefficients would be misguided and will yield the wrong answer.

[29] In Figure 3 (bottom) the difference in spectral slopes between v and b in each 4.55-h subinterval is binned. The median value of the difference in spectral indices is 0.21. Velocity spectra flatter than magnetic field spectra in the solar wind at 1 AU have been found by *Podesta et al.* [2007] and *Salem et al.* [2009] using measurements from the WIND spacecraft and by *Tessein et al.* [2009] and *Borovsky and Denton* [2010] using measurements from ACE. A difference in spectral slopes between v and b could be deduced from the frequency-dependent Alfvén ratio of the solar wind turbulence plotted [e.g., *Tu et al.*, 1989b, Figure 11; *Marsch and Tu*, 1990, Figure 7]. Velocity spectra that are shallower than the magnetic field spectra have been reported for the fluctuations of the solar wind in the inner heliosphere from Helios measurements [cf. *Grappin et al.*, 1991, Figure 6b]

Table 3. Summary of the Spectral Indices of the Trace-v Velocity PSDs, the Trace-B Magnetic Field PSDs, the Trace-b Magnetic Field PSDs, and the E Total-Energy PSDs Obtained Through Three Different Methods

	Ensemble of Spectral Fits	Fit to Ensemble-Averaged Spectrum	Fit to Single Large Spectrum
v slope	−1.41 ± 0.39	−1.40	
B slope	−1.62 ± 0.49	−1.60	−1.61
b slope	−1.62 ± 0.39	−1.59	
E slope	−1.52 ± 0.39	−1.52	

[a]The indices are power law fits over the frequency range 4.3×10^{-4} Hz < f < 1.9×10^{-3} Hz.

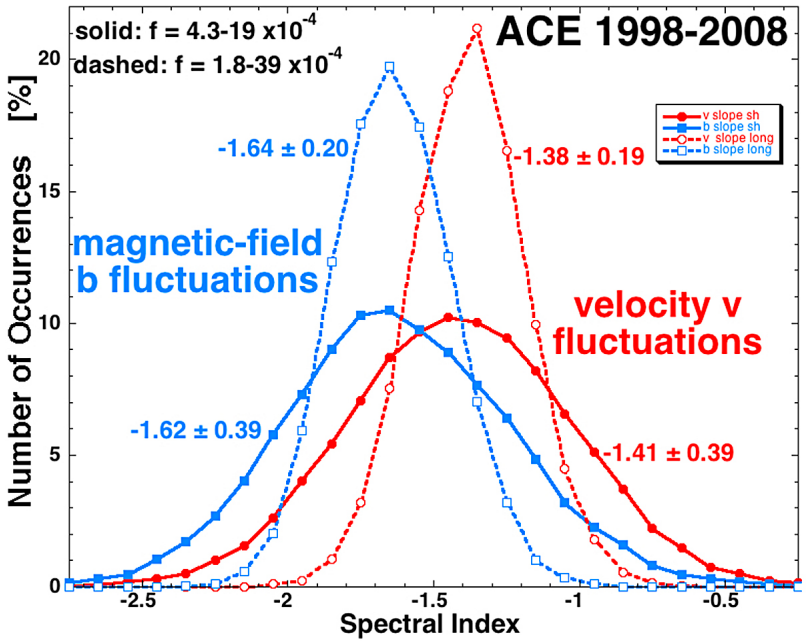

Figure 4. For the 1998–2008 ACE measurements, the spectral indices of the velocity v and the magnetic field b determined by fitting the PSDs in the standard frequency range f = 4.3 × 10^{-4}–1.9 × 10^{-3} Hz are binned (solid curves) and the spectral indices of the velocity and the magnetic field determined by fitting the PSDs in the larger frequency range f = 1.8 × 10^{-4}–3.9 × 10^{-3} Hz are binned (dashed curves). The means and standard deviations of the spectral indices for each distribution are indicated on the figure.

and *Roberts* [2010] has found different rates of radial evolution for the velocity spectra and magnetic field spectra using Helios and ULYSSES measurements. Velocity spectra that are consistently shallower than magnetic field spectra have also been observed by the ISEE-2 spacecraft for the MHD turbulence in the Earth's plasma sheet [*Borovsky et al.*, 1997; *Borovsky and Funsten*, 2003b]. Velocity spectra that are shallower than the magnetic field spectra can also be found in some computer simulations of MHD turbulence [e.g., *Biskamp and Muller*, 2000, Figure 10; *Müller and Grappin*, 2005, Figure 1; *Boldyrev et al.*, 2011, Figures 1 and 2].

[30] As a check on the values of the spectral indices and the systematic difference between them, fits to the spectra over a broader range of frequency are made. The solid curves in Figure 4 are the binned spectral indices of v and B obtained by fitting the PSDs over the standard range f = 4.3 × 10^{-4}–1.9 × 10^{-3} Hz: the dashed curves in Figure 4 are the binned spectral indices of v and B obtained by fitting the PSDs over the broader range f = 2.1 × 10^{-4}–3.8 × 10^{-3} Hz. Note that the high-frequency limit 3.8 × 10^{-3} Hz of this broader frequency range is only a factor of 2 away from the Nyquist frequency of the 64-s-resolution ACE merged data. One should worry about noise with frequencies near and above the sampling frequency being aliased and adding power to portions of the Fourier transform with frequencies below the Nyquist frequency. For our particular case, the following three facts act in favor of reducing the amount of aliased power near the Nyquist frequency. (1) The amplitude of the Fourier components of the fluctuations in the solar wind are decreasing with increasing frequency, so higher-frequency fluctuations that could be aliased to lower frequencies are anticipated to be of smaller amplitudes. (2) The 64-s ACE magnetometer data set is created by temporally averaging higher-time-resolution magnetic field measurements, hence modes with frequencies higher than 1/64 Hz are very strongly suppressed in the data set. (3) The 64-s SWEPAM velocity measurements used to make the ACE data set are each obtained from a proton distribution function which typically requires approximately 26 s of energy-spin sweeping to capture, followed by 38 s wherein no proton data is collected; hence there is partial averaging which will partially suppress modes with frequencies higher than the Nyquist frequency. For point (3), the amount of suppression depends on whether the beam of solar wind protons is (1) aligned with the ACE-spacecraft spin axis or (2) off axis; there is more averaging and more suppression when the solar wind is axially aligned. As can be seen in Figure 4, the mean values of the distributions of slopes are approximately the same for the narrow (solid) and broad (dashed) ranges of frequencies, but the spread is reduced for the longer-frequency-interval fits. The wider-range spectral fits re-confirm that the velocity spectra are shallower than the magnetic field spectra and that there is a more-statistically significant difference between the spectral indices of v and B. Note that the width of the magnetic field distribution for the larger frequency range (dashed blue curve) in Figure 4 is comparable to the width of the distribution obtained by *Smith et al.* [2006]: the width in Figure 4 is ±0.20 with a fit that is 1.25 orders of magnitude in frequency range and the width in Figure 2 of *Smith et al.* [2006] is ±0.14 with a fit that is 1.1 orders of magnitude in frequency.

[31] An important quantity is the spectral index of the total energy in the fluctuations: $\delta E = m_i n \delta v^2/2 + \delta B^2/8\pi$ [cf. *Tu*

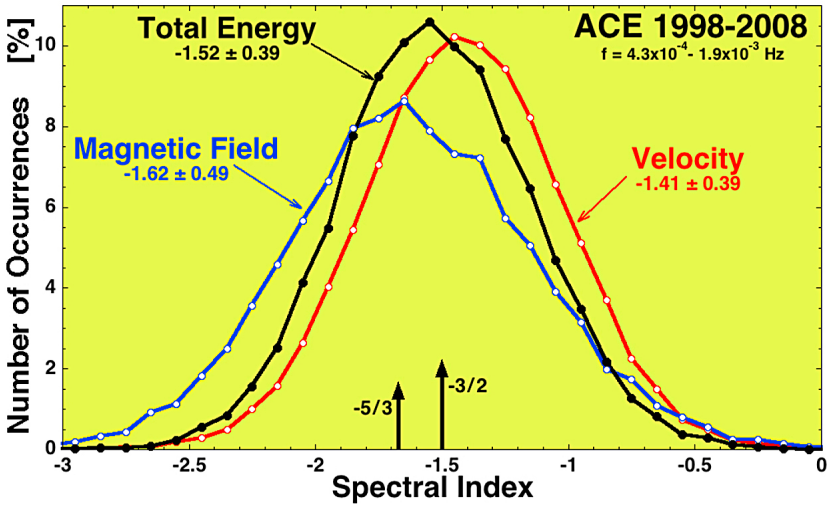

Figure 5. For each 4.55-h subinterval in 1998–2008 the spectral indices of the velocity PSD (red), the magnetic field PSD (blue), and the total energy PSD (black) are calculated and binned. Arrows at the bottom of the plot indicate the position of the Kolmogorov $k^{-5/3}$ spectral index and the Kraichnan $k^{-3/2}$ spectral index.

and Marsch, 1995a, equations (2.15) and (2.18)]. In Figure 5 the distribution of spectral indices for the total energy of each 4.55-h subinterval is binned (black curve) [see also *Tessein et al.*, 2009, Figure 3]. The distribution of measured spectral indices is described (mean ± standard deviation) by -1.52 ± 0.39. For comparison the distributions of velocity v spectral indices (blue) and magnetic field B spectral indices (red) are also displayed. The values are entered into Table 3.

[32] The reader is reminded that the analysis of Appendix A concludes that the statistical mean value of the ensemble of spectral indices is the value to take.

[33] A check on the accuracy of the average of the ensemble of spectral-index measurements is to compare the ensemble of spectral indices with the spectral index of an ensemble-averaged spectrum [cf. *Welch*, 1967]. In Figure 6 ensemble-averaged spectra for v, B, b, and E are plotted. The v, b, and E spectra are each the average of 15,472 PSDs and the B spectrum is the average of 20,076 spectra, all from sequential non-overlapping data intervals. Each of the four ensemble-averaged spectra in Figure 6 is fit with a log-log linear regression in the frequency range 4.3×10^{-4} Hz $\le f \le$ 1.9×10^{-3} Hz and the spectral indices are noted in the figure. These values are collected into Table 3. As can be seen in the table, the spectral indices of the four ensemble-averaged spectra for v, B, b, and E are very close to the mean values of the ensemble of spectral indices from the thousands of individual spectra.

[34] Another check on the accuracy of the index is to compare the ensemble-averaged spectrum (and its index) with a single Fourier transform of the entire time series data set. Since the ACE velocity data set contains large regions of data dropout, making the single large Fourier transform is only practical for the magnetic field B. Picking the largest power-of-2 number of data points in the data set (2^{22}), the trace-B power spectral density for ACE measurements from 1998 to 2006 is calculated and plotted in Figure 7 as the black curve [see also *Borovsky*, 2010a]. Note that this single

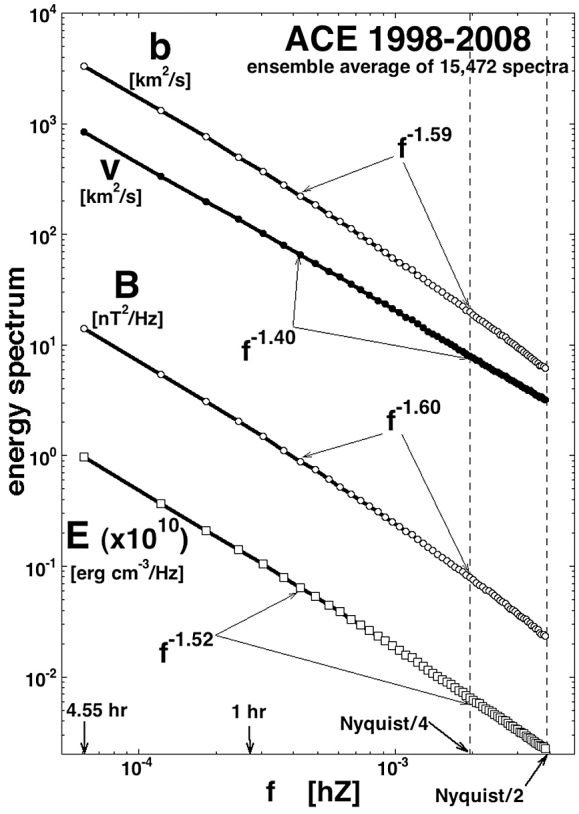

Figure 6. For the entire 1998–2008 ACE data set, the spectrum from each 4.55-h data subinterval is calculated and the spectra are summed together to produce ensemble-average spectra. For v, B, b, and E those ensemble-averaged spectra are plotted.

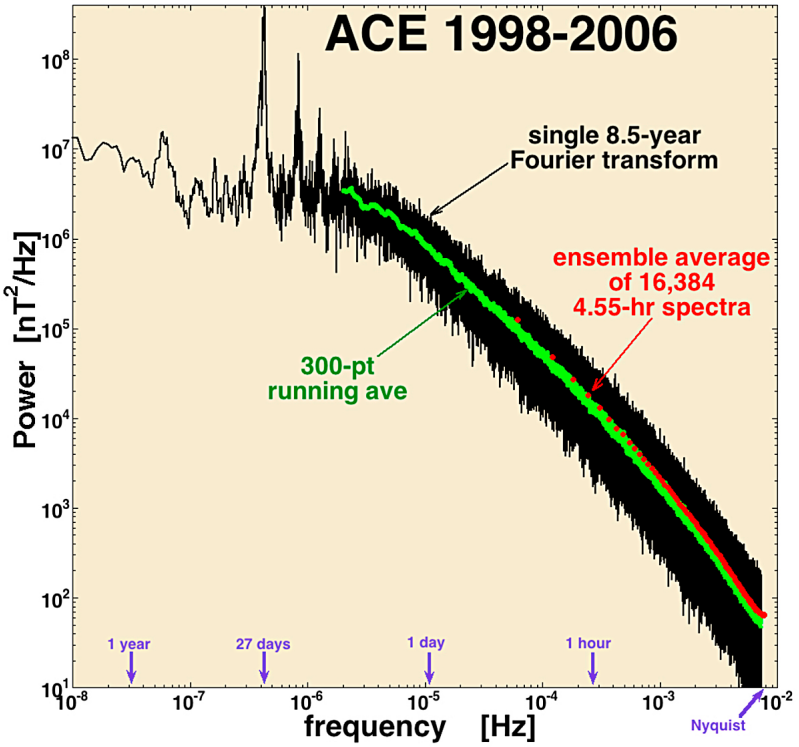

Figure 7. Using the same magnetic field measurements in the ACE 1998–2006 data set, a single Fourier transform of 2^{22} data points is plotted (black) along with the ensemble-averaged spectrum (red) from 16,384 Fourier transforms of 256 points each (1998–2006). The trace-B spectral indices are −1.60 for ensemble spectrum and −1.61 for single large spectrum.

Fourier transform extends to very low frequencies. For frequencies $f > 2 \times 10^{-6}$ Hz a 300-point running average of the spectrum is plotted as the green points. For the comparison, an ensemble spectrum is created by summing the 16,383 trace-B power spectral densities for the 4.55-h subintervals from the same 1998–2006 time interval: this ensemble-averaged spectrum is plotted as the red points in Figure 7. As can be seen, the shape of the ensemble of spectra (red) is very similar to the shape of the single spectrum (green). In the frequency range 4.3×10^{-4} Hz $\leq f \leq 1.9 \times 10^{-3}$ Hz the single trace-B spectrum (black points) is fit by a log-log linear regression with a spectral index −1.61 and the ensemble-averaged spectrum is fit by a spectral index −1.60. (These values are entered into Table 3.) The two spectral indices are very close, providing a check on the accuracy of the mean of the ensemble of spectral indices.

[35] Note in Figure 7 that the red and green curves show noticeable downward deviations from power laws at frequencies above 1/4 times the Nyquist frequency (above 2.0×10^{-3} Hz). This downward deviation is owed to the attenuation of Fourier components by the 64-s averaging of the magnetic field measurements to produce the 64-s time resolution data. At the Nyquist frequency Fourier components are attenuated by a factor of 0.635; in the power spectral density (the square of the Fourier transform) the amplitude attenuation is 0.403, which is approximately the factor by which the red and green curves deviate from a power law in Figure 7.

[36] The spectral indices of the Elsasser-variable PSDs are examined in Figure 8. For each 4.55-h subinterval, the PSD of the each Elsasser variable $\underline{z}^+ = \underline{v} + \underline{b}$ and $\underline{z}^- = \underline{v} - \underline{b}$ is determined via the direct FFT method (with linear detrending). In constructing the Elsasser variables the 64-s-resolution values of $\underline{v}$, $\underline{B}$, and n are used and, following the spirit of

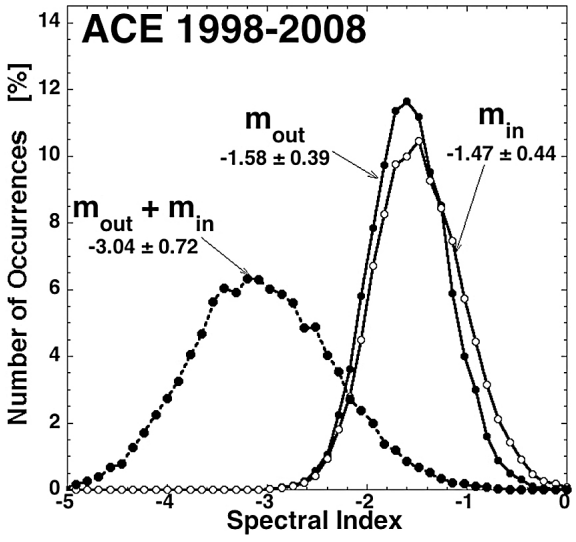

Figure 8. The spectral index m_{out} of the Elsasser variable z_{out} and the spectral index m_{in} of the Elsasser variable z_{in} are calculated for every 4.55-h subinterval in 1998–2008 and binned. Also binned is the sum $m_{out} + m_{in}$ of the spectral indices for every subinterval.

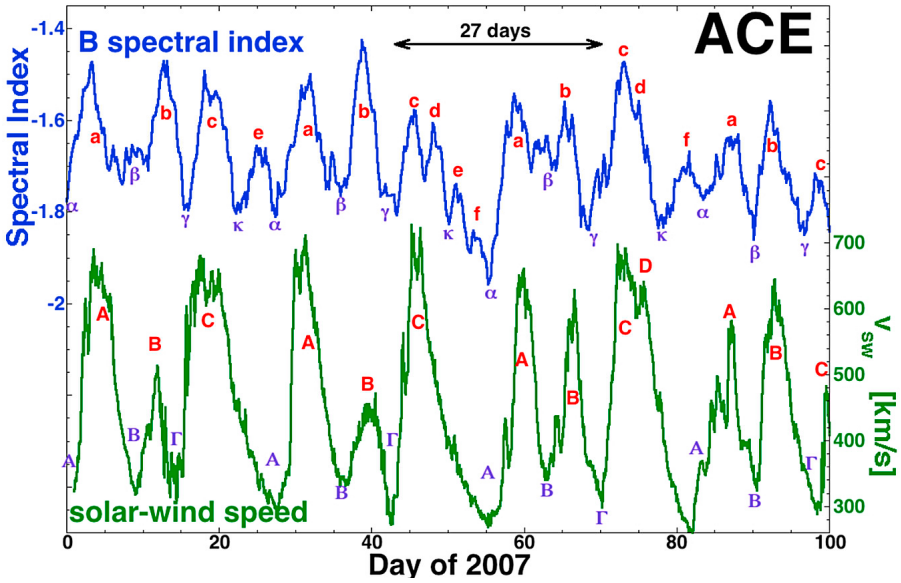

Figure 9. For 100 days in 2007 a 1-day running average of the spectral index of the magnetic field fluctuations δB (blue; left axis) is plotted along with the speed of the solar wind (green; right axis). 27-day repeating peaks (roman letters) and troughs (Greek letters) in both curves are identified and labeled. For noise-reduction purposes, the spectral indices in this figure are fit over the frequency range 1.8×10^{-4}–3.9×10^{-3} Hz.

section 2.2.2 of *Tu and Marsch* [1995a], $\underline{B}$ is replaced by $-\underline{B}$ if the average magnetic field for a 4.55-h subinterval is outward along the nominal Parker-spiral direction so that z^+ denotes outward propagation and z^- denotes inward propagation. With this prescription, we will refer to the two Elsasser variables as z_{out} and z_{in} to avoid confusion. All ions are assumed to be protons in the construction of $\underline{b}$ from measured values of $\underline{B}$ and n. From the PSDs of z_{out} and z_{in} the two spectral indices m_{out} and m_{in}, are obtained by linear-regression fit in $\log_{10}$(PSD)-versus-$\log_{10}$(f) space over the standard frequency range. In Figure 8 the spectral indices m_{out} and m_{in} are binned for the 1998–2008 ACE data set. The sum $m_{out} + m_{in}$ for each subinterval is also binned [cf. *Grappin et al.*, 1983]. Consistent with previous reports for the inertial subrange of solar wind turbulence at 1 AU [e.g., *Tu and Marsch*, 1990], the spectral index m_{in} of z_{in} is slightly shallower (mean value -1.47) then the spectral index m_{out} of z_{out} (mean value -1.58).

4.2. Dependence of Spectral Indices on Solar Wind Parameters

[37] In Figure 9 a 1-day running average of the spectral index of the magnetic field B is plotted in blue (left axis) for the first 100 days of 2007 when clearly identifiable 27-day-repeating high-speed streams were occurring. Plotted in green (right axis) is the solar wind velocity. Systematic variations in the spectral index of the solar wind magnetic field fluctuations are clearly seen. For the blue spectral-index curve, isolated peaks in the spectral index are marked in the figure with red lower-case roman letters and isolated troughs are labeled with purple lower-case Greek letters. The peaks labeled "a" are each separated by 27-days: hence they can all be identified with the same solar longitude on the rotating Sun. Likewise for the sets of "b," "c," "d," "e," and "f" peaks and "α," "β," "γ," "δ," and "ε" troughs. For the green curve in Figure 9 the isolated peaks are labeled with red upper-case roman letters and the isolated troughs are labeled with purple upper-case Greek letters. The set of "A" velocity peaks matches the set of "a" spectral-index peaks. And the set of "A" velocity troughs matches the set of "α" spectral-index troughs. Likewise for the "B" ("b") and "C" ("c") peaks and for the "B" ("β") and "Γ" ("γ") troughs. In Figure 9 the flow-velocity pattern is indicative of various types of solar wind plasma passing the spacecraft: i.e., slow wind, compressed slow wind, compressed fast wind, coronal-hole fast wind, rarefacted coronal-hole wind, etc. The spectral index of the fluctuations changes with the type of wind. The spectral index of the turbulence tends to repeat the value it had 27 days earlier: this is associated with the same type of plasma returning every 27 days, be it the well-known repetition of high-speed streams [*Mursula and Zieger*, 1996] or the lesser-appreciated repetition of slow wind [cf. *Borovsky and Steinberg*, 2006b, Figure 20]. Note that the sets of "d," "e," and "f" peaks and "ε" troughs in the blue spectral-index curve do not have counterpart peaks or troughs in the green solar wind-velocity curve. Investigation shows that these other peaks and troughs tend to be associated with peaks and troughs in the proton specific entropy of the solar wind plasma, indicating again that a change in the type of solar wind plasma can lead to a change in the spectral index of the solar wind fluctuations.

[38] In Figure 10 (top) the spectral indices of v and B are plotted as functions of the solar wind proton specific entropy S_p. The velocity spectral indices for each 4.55-h subinterval are in red and the magnetic field spectral indices are in blue. 400-point running averages of the spectral indices of v, B, and E are plotted in black and labeled. As can be seen, there is systematic variation of the v, B, and E spectral indices with S_p: the total energy spectral index is steeper for low-specific entropy plasma (about -1.6) and shallower for

high-specific entropy plasma (about −1.4). In Figure 10 (middle) the spectral indices are plotted as functions of the carbon charge-state ratio C^{6+}/C^{5+} of the solar wind. The running averages show systematic trends with the spectral indices shallower for lower ratios of C^{6+}/C^{5+}. In Figure 10 (bottom) the spectral indices are plotted as functions of N_d, the number of strong current sheets in a subinterval. A random number between 0.0 and 1.0 has been added to N_d in the plot to spread the data points off the integer values. As seen by the running averages, the total-energy spectral index is shallower (about −1.4) for large N_d and steeper (about −1.55) for small N_d. Note in all three panels of Figure 10 that the magnetic field spectral index varies more than the velocity spectral index does: this was also reported by *Borovsky and Denton* [2010] in the transition between slow wind and fast wind across CIRs and by *Podesta and Borovsky* [2010]. Note that some of the variation in the B spectral index could be owed to the movement of the spectral breakpoint into the range of frequencies fitted (A. Roberts, private communication, 2012).

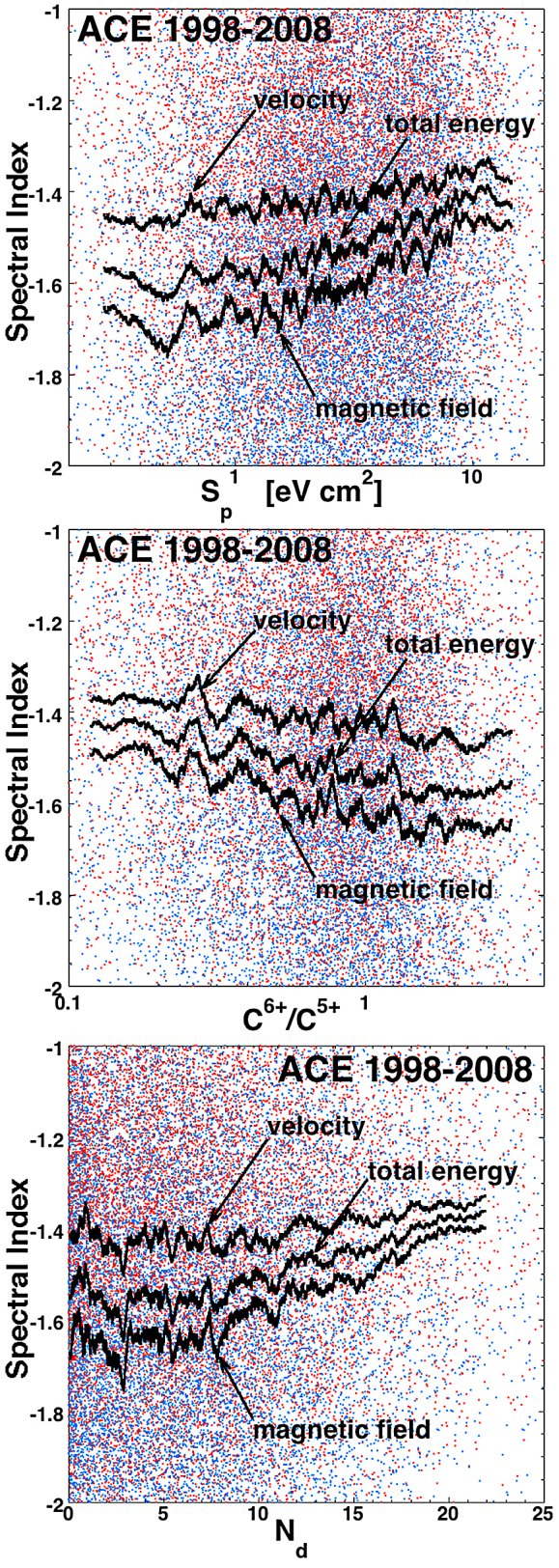

Figure 10. (top) A function of the solar wind proton specific entropy S_p, (middle) a function of the solar wind carbon charge-state ratio C^{6+}/C^{5+}, and (bottom) a function of the number of directional discontinuities (current sheets) per subinterval N_d, the spectral indices of the velocity (red points) and magnetic field (blue points) are plotted for every 4.55-h subinterval in 1998–2008. 400-point running averages of the spectral indices of v, B, and E are plotted in black and labeled.

[39] The difference between the spectral index of v and the spectral index of B is plotted as a function of S_p (Figure 11, top) and as a function of N_d (Figure 11, bottom): only 400-point running averages are shown. The black points pertain to the difference in the spectral slopes between v and B and the green points pertain to the difference in the spectral slopes between v and b. Figure 11 (top) reveals a trend wherein the spectral slopes of v and B (and v and b) tend to become closer as the specific entropy of the plasma increases. Figure 11 (bottom) indicates a trend in which the difference between the spectral slopes of v and B are reduced as the number N_d of strong discontinuities per subinterval increases. High N_d values are associated with high-speed wind and highly Alfvénic wind [cf. *Borovsky and Denton*, 2010, Figure 12]. Again, this behavior could in part be caused by movement of the magnetic field spectral breakpoint.

[40] In Table 4 the value of Pearson's linear-correlation coefficient R_{corr} between the spectral indices of v, B, b, and E and the properties of the solar wind plasma and the amplitude of the fluctuations in the solar wind. Also included are the difference between the spectral indices of v and b and the spectral indices of the Elsasser variables z_{out} and z_{in}. The individual correlation coefficients vary, but general trends are that the spectral indices are positively correlated with the solar wind speed v_{sw}, the proton temperature T_p, the proton and alpha-particle specific entropies S_p and S_α, and with N_d. The spectral indices tend to be anticorrelated with the solar wind number density n, magnetic field strength B, the charge-state ratios C^{6+}/C^{5+} and O^{7+}/O^{6+}, and the Fe/O density ratio. In Table 4 the two plasma parameters that have the strongest correlations with the values of the spectral indices are $\log(S_p)$ and $\log(C^{6+}/C^{5+})$, both of which are indicators of the type of plasma. Correlation coefficients between the spectral slopes and the fluctuation amplitudes are also

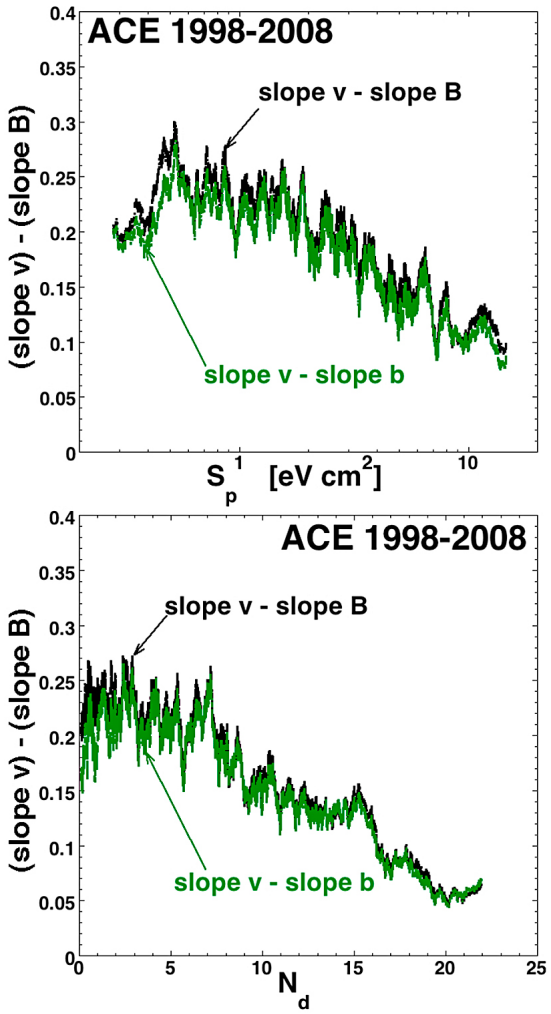

Figure 11. (top) A function of the solar wind proton specific entropy S_p and (bottom) a function of the number of directional discontinuities (current sheets) per subinterval N_d, 400-point running averages of the differences between the velocity and magnetic field spectral indices are plotted for the 4.55-h subintervals in 1998–2008.

included in Table 4: in general the spectral indices are positively correlated with the amplitudes of the fluctuations. The fluctuation amplitudes will be discussed further in section 5.

4.3. Spectral Indices and the Type of Solar Wind

[41] In the first three columns of Table 5 the median values of the spectral indices of v, B, b, E, z_{out}, and z_{in} of the solar wind are collected as functions of the three types of wind, using the *Zhao et al.* [2009] method to categorize the wind type. The coronal-hole-origin wind and non-coronal-hole-origin (streamer-belt) wind show the well-known fast-wind and slow-wind tendencies [cf. *Tu and Marsch*, 1995a; *Bruno et al.*, 2007; *Tessein et al.*, 2009; *Borovsky and Denton*, 2010] with the spectral indices all being statistically shallower for coronal-hole wind. (*Yordanova et al.* [2009] examined 10 intervals of magnetic field measurements on Ulysses between 1.4 and 5 AU from the Sun wherein the O^{7+}/O^{6+} charge-state ratio was used to differentiate "fast streams" from "slow streams": spectral indices similar to those in row 2 of Table 5 were observed.) For CME wind, the spectral indices in Table 5 are steep, sometimes steeper than those of non-coronal-hole wind. Note for CME wind (with perhaps both magnetic foot points on the Sun) the similarity in the spectral indices of z_{out} and z_{in} in Table 5.

[42] In the third and fourth columns of Table 5 the median values of the spectral indices are collected for slow wind ($v < 450$ km/s) and for fast wind ($v > 550$ km/s). As can be seen by comparing with columns 1 and 2, the slow wind and non-coronal-hole-origin plasma have similar statistics and the fast wind and coronal-hole-origin plasma have similar statistics.

[43] We argue here that the slow-wind fast-wind difference in the spectral indices at 1 AU is not caused so much by the age difference of the wind [cf. *Horbury and Schmidt*, 1999], but rather by the coronal-hole versus non-coronal-hole origin of the plasma. To test this, we separate wind of similar speed into coronal-hole versus non-coronal-hole collections. Fast wind tends to be of coronal-hole origin, slow wind can be of coronal-hole origin [e.g., *Arge and Pizzo*, 2000; *Wang and Sheeley*, 2003; *Wang*, 2011] or streamer-belt origin [e.g., *Habbal et al.*, 1997; *Ofman*, 2004; *Suess et al.*, 2009]. Data subintervals with mean solar wind speeds between 375 km/s and 425 km/s are collected and the median values of the spectral indices are displayed in columns 6 and 7 of Table 5 separately for non-coronal-hole-origin plasma and for coronal-hole-origin plasma. For these two collections the spectral indices are steeper for slow non-coronal-hole wind than for slow coronal-hole wind. The spectral indices of slow coronal-hole-origin wind (column 7) resemble more the indices of coronal-hole wind (column 2) than they do of slow wind (column 4), indicating that type of wind is more fundamental than speed (=age) of wind.

Table 4. Linear Correlation Coefficients R_{corr} (in Percent) Between the Spectral Indices of the Solar Wind Turbulence and Several Properties of the Solar Wind and the Turbulence Amplitude

	v Slope	B Slope	b Slope	E Slope	(v Slope)–(b Slope)	z_{out} Slope	z_{in} Slope
v_{sw}	+9	+25	+23	+24	−16	+27	+32
n	−20	−16	−18	−22	+2	−22	−33
T_p	+3	+24	+26	+20	−18	+22	+24
B	−18	+3	+5	−4	−20	−4	−11
$\log(S_p)$	+11	+26	+24	+25	−15	+27	+38
$\log(S_\alpha)$	+8	+22	+21	+22	−15	+25	+31
β_i	+4	−3	−10	−5	+14	−3	−8
β^*	+5	−15	−20	−14	+24	−13	+22
v_A	−4	+15	+22	+12	−26	+14	+14
C_s^*	+3	+25	+21	+20	−18	+22	+25
N_d	+4	+22	+16	+17	−13	+20	+31
$\log(C^6/C^5)$	−16	−23	−20	−25	+8	−24	−38
$\log(O^7/O^6)$	−15	−19	−18	−22	+6	−21	−25
Fe/O	−11	−4	−11	−15	−3	−17	−18
δv	+7	+38	+36	+35	−32	+37	+58
δB	−9	+21	+16	+11	−25	+14	+18
δb	+1	+32	+31	+26	−31	+29	+42
δE	−9	+18	+15	+12	−19	+13	+15
$\delta v/v_A$	+9	+32	+26	+30	−19	+33	+56
$\delta B/B$	+4	+24	+16	+18	−13	+22	+36
$\delta\varepsilon 8\pi/B^2$	+8	+29	+24	+26	−18	+29	+46
$\log(r_A)$	+15	+23	+24	+34	−13	+32	+54
$\log(\delta z_{out}/\delta z_{in})$	+8	+32	+31	+31	−25	+18	+64

[a]The asterisk is a reminder that $T_e = 12.9$ eV [cf. *Skoug et al.*, 2000] is used to calculate β and C_s.

Table 5. Using the *Zhao et al.* [2009] Scheme to Categorize the Wind From the ACE SWICS Measurements of the O^{7+}/O^{6+} Charge-State Ratio, Median Values of Several Turbulence Parameters Are Shown for the Various Types of Solar Wind

	Non-Coronal-Hole-Origin Plasma	Coronal-Hole-Origin Plasma	CME	Slow Wind v < 450	Fast Wind v > 550	Non-Coronal-Hole-Origin Plasma 375 < v < 425	Coronal-Hole-Origin Plasma 375 < v < 425
slope v	−1.40	−1.36	−1.45	−1.40	−1.34	−1.42	−1.37
slope B	−1.70	−1.56	−1.68	−1.70	−1.54	−1.71	−1.63
slope b	−1.67	−1.55	−1.64	−1.66	−1.52	−1.68	−1.60
slope E	−1.57	−1.46	−1.58	−1.55	−1.44	−1.58	−1.52
slope v - slope B	0.25	0.18	0.19	0.26	0.18	0.26	0.21
slope z_{out}	−1.65	−1.53	−1.65	−1.64	−1.50	−1.65	−1.60
slope z_{in}	−1.57	−1.28	−1.63	−1.53	−1.25	−1.58	−1.35
$\delta v/v_A$	0.11	0.19	0.15	0.12	0.22	0.11	0.15
$\delta B/B$	0.16	0.24	0.21	0.17	0.26	0.16	0.21
$\delta E8\pi/B^2$	0.038	0.097	0.021	0.043	0.12	0.039	0.066
ϖ_ρ (km/s)	373	506	509	378	611	395	408
$\sigma\eta\iota\phi\tau\varepsilon\delta$ $\delta v/v_A$	0.14	0.19	0.085	1.5	0.19	0.14	0.18
$\sigma\eta\iota\phi\tau\varepsilon\delta$ $\delta B/B$	0.20	0.24	0.11	2.1	0.23	0.20	0.24
$\sigma\eta\iota\phi\tau\varepsilon\delta$ $\delta E8\pi/B^2$	0.061	0.095	0.020	0.066	0.087	0.057	0.091
r_A	0.47	0.65	0.45	0.52	0.70	0.49	0.57
$\delta z_{out}/\delta z_{in}$	1.5	2.7	1.1	1.6	2.8	1.6	2.3
N_d	3	9	1	4	11	3	6

[a]The three "shifted" amplitudes are shifted to a median solar wind speed of 500 km/s using a $k^{-1.6}$ spectrum.

4.4. Autocorrelation Functions of the Spectral Indices

[44] The temporal autocorrelation functions of the spectral indices of the solar wind fluctuations are explored in Figure 12. The autocorrelation function $A(\Delta t)$ of a function f (t) is constructed by first subtracting the average value of the function $f_o = \langle f(t) \rangle$ to produce a new function $F(t) = f(t) - f_o$; the autocorrelation function $A(\Delta t)$ of f(t) is then $A(\Delta t) = \int F(t)F(t - \Delta t)dt / \int F(t)F(t)dt$. Here f(t) is the spectral index of the fluctuations in the solar wind measured every 4.55 h; thus the time shift Δt is in increments of 4.55 h and $\int dt$ is over the entire 11-year 1998–2008 ACE data set. Note that the autocorrelation function is normalized to be unity at $\Delta t = 0$. The autocorrelation functions in Figure 12 are corrected for "shot noise" [cf. *Borovsky et al.*, 1997] which can be caused by measurement inaccuracy or by correlations in the data set that are shorter than the 4.55-h resolution. This correction is done by fitting an exponential function to the autocorrelation function in the range $\Delta t = 4.55$ h to $\Delta t = 13.65$ h (= 3 × 4.55 h), replacing the autocorrelation function between $\Delta t = 0$ and $\Delta t = 4.55$ h with an extrapolation of the exponential-fit function and then multiplying the entire autocorrelation function by a constant so that the corrected autocorrelation function is unity at $\Delta t = 0$. In Figure 12 (top) the autocorrelation functions of the spectral indices of the trace-v spectrum (red curve), the trace-B spectrum (blue curve), and the total-energy spectrum (black curve) are plotted for time shifts of up to 40 days. Note the decay from unity as the time shift Δt increases from 0 and note also the peaks at 27 days, the solar rotation period. Note that the half width of the $\Delta t = 27$-day peak is about equal to the half width of the peak at $\Delta t = 0$.

[45] In the second panel of Figure 12 the autocorrelation functions of the spectral indices of v (red), B (blue), and E (black) are plotted for 70 h along with the autocorrelation functions of the spectral indices of the two Elsasser variables z_{out} (purple dashed) and z_{in} (green dashed). All five spectral indices have similar decay rates from unity. The temporal rate of decrease from unity of the autocorrelation function is a measure of the temporal persistence of the function. In Table 6 the autocorrelation times (persistence times) of the five spectral indices are listed, where the autocorrelation times are defined to be the time at which the autocorrelation function decreases to 1/e = 0.367 from unity. Autocorrelation times of 10–30 h are obtained.

[46] In Figure 12 (bottom) the autocorrelation function of several solar wind plasma properties are plotted (colors) for comparison with the autocorrelation functions of the spectral indices of the second panel (all replotted in gray). Note the differences between the autocorrelation function of the solar wind velocity (orange) and those of the spectral indices (gray): because of these differences the temporal variation of the solar wind velocity does not well-describe the temporal variation of the spectral indices. The two plasma properties that had the strongest correlations with the spectral indices were $\log(S_p)$ and $\log(C^{6+}/C^{5+})$ (see Table 4); in Figure 12 (bottom) it is seen that these two quantities (red and blue curves) have similar temporal variations to the spectral indices.

5. Fluctuation Amplitudes

[47] The amplitude of the magnetic field and velocity fluctuations in each 4.55-h-long data subinterval is determined as follows. First the time series data is Fourier transformed (after detrending with a line). Then all Fourier coefficients with frequencies $f < 1 \times 10^{-3}$ Hz (periods > 16.6 min) are zeroed out and an inverse Fourier transform is performed. The RMS fluctuation levels of the Fourier-filtered variables in each 4.55-h data subinterval are then calculated. These RMS amplitudes are taken as measures of the fluctuation amplitude.

5.1. General Statistics and Solar-Cycle Dependence of the Fluctuation Amplitudes

[48] In Figure 13 the amplitudes of the velocity fluctuations $\delta v = ((\delta v_r)^2 + (\delta v_t)^2 + (\delta v_n)^2)^{1/2}$ (red) and of the magnetic field fluctuations $\delta B = ((\delta B_r)^2 + (\delta B_t)^2 + (\delta B_n)^2)^{1/2}$ (blue) are plotted for the years 1998–2008, one pair of points for every 4.55-h subinterval. A 27-day running averages are

also shown in the figure. As can be seen, δv and δB have similar temporal behavior. For the 1998–2008 ACE data set, δv and δB have a linear correlation coefficient $R_{corr} = +0.66$. The mean values of δv and δB are noted in Figure 13 by dashed lines. Factor-of-2 systematic changes in the amplitudes through the solar cycle are seen with similar trends in δv and δB. The year 2003 shows larger-than-average amplitudes; 2003 contained a large fraction of fast wind and the raw amplitudes δv and δB are higher in fast wind [cf. *Borovsky and Denton*, 2010, Figure 11].

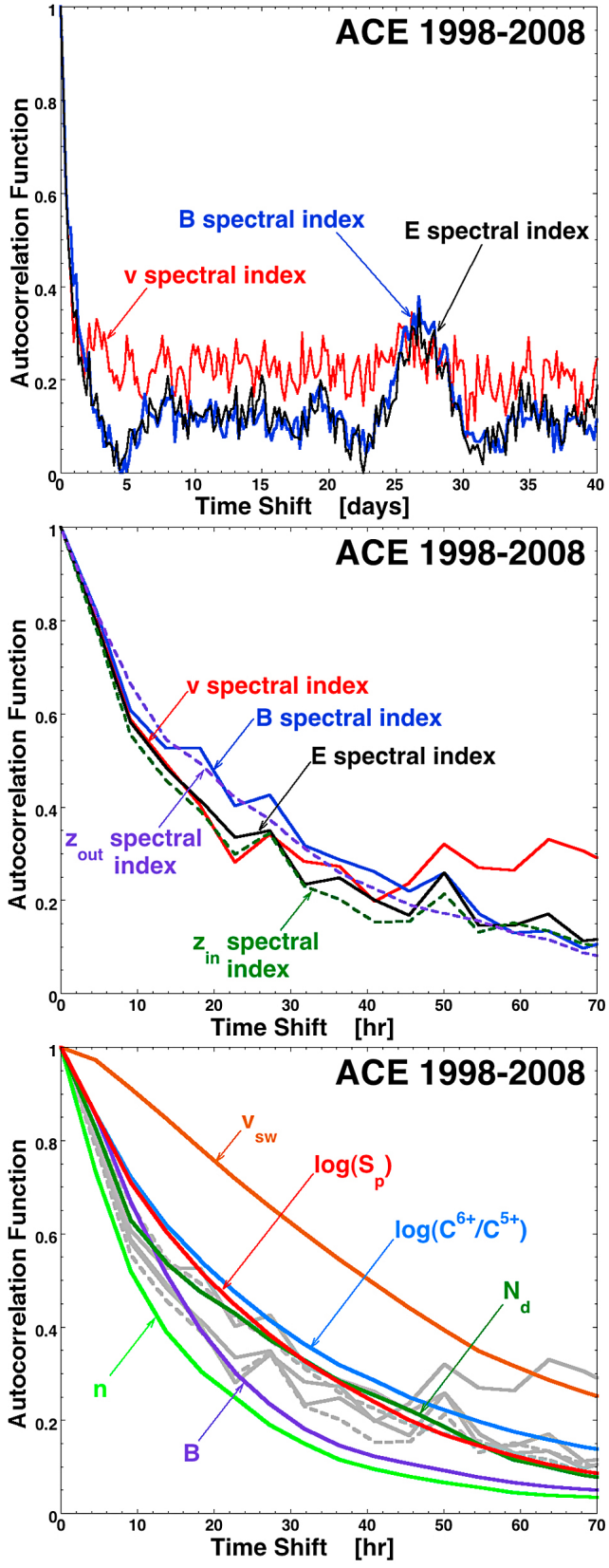

Figure 12. The autocorrelation functions for the trace-v, trace-B, and E spectral indices are plotted (top) for 40 days and (bottom) for 70 h. Also plotted in the second panel are the autocorrelation functions for the spectral indices of z_{out} and z_{in}. (bottom) The autocorrelation function of the spectral indices (gray curves) are compared with the autocorrelation functions of various solar wind parameters. All autocorrelation functions are corrected for shot noise and renormalized.

Table 6. Autocorrelation Times for the Amplitude of the Turbulence in the Solar Wind and for the Solar Wind Velocity and the Number of Strong Discontinuities (Current Sheets) per 4.55-h Data Subinterval

Symbol	τ_{auto}	Quantity
slope v	20 h	spectral index of trace-v
slope B	30 h	spectral index of trace-B
slope b	23 h	spectral index of trace-b
slope E	21 h	spectral index of total energy
slope z_{out}	19 h	spectral index of Elsasser outward
slope z_{in}	28 h	spectral index of Elsasser inward
δv	37 h	amplitude of velocity fluctuations
δB	16 h	amplitude of magnetic field fluctuations
δb	35 h	amplitude of magnetic field fluctuations
δE	11 h	amplitude of total-energy fluctuations
$\delta v/v_A$	33 h	normalized velocity amplitude
$\delta B/B$	27 h	normalized magnetic field amplitude
$\delta E 8\pi/B^2$	26 h	normalized total-energy amplitude
$\log(r_A)$	20 h	logarithm of the Alfvén ratio
$\log(\delta z_{out}/\delta z_{in})$	27 h	logarithm of the outward/inward Elsasser ratio
v_{sw}	53 h	solar wind velocity
n	15 h	solar wind number density
B	20 h	solar wind magnetic field strength
T_p	23 h	solar wind proton temperature
$\log(S_p)$	29 h	logarithm of the proton specific entropy
$\log(S_\alpha)$	36 h	logarithm of the alpha-particle specific entropy
N_d	28 h	number of strong discontinuities per subinterval
$\log(C^6/C^5)$	31 h	logarithm of the carbon charge-state ratio
$\log(O^7/O^6)$	29 h	logarithm of the oxygen charge-state ratio
type	27 h	coronal-hole vs non-coronal-hole typing of wind

[a]The autocorrelation times are obtained from the 1/e method using autocorrelation functions that are corrected for shot noise.

[49] Measuring the magnetic field-fluctuation amplitude in Alfvén units, $\delta b = \delta(B/4\pi nm_i)$, the magnetic field and velocity amplitudes are more similar. In Figure 14 the amplitude of the magnetic field fluctuations is measured three different ways (δB, δB/B, and δb) [see also *Borovsky*, 2006; *Borovsky and Steinberg*, 2006a] for each 4.55-h subinterval of 1998–2008 and these three amplitudes are plotted as functions of the velocity amplitude in each subinterval. The linear correlation coefficients R_{corr} are indicated in the figure. As can be seen, δb has the highest correlation coefficient with δv: $R_{corr} = +0.95$ [see also *Borovsky and Steinberg*, 2006a; *Borovsky*, 2006]. This high correlation coefficient holds also when only $N_d = 0$ subintervals are used. Taking a least squares linear-regression fit of δb as a function of δv and another linear-regression fit of δv as a function of δb and logarithmically averaging the slopes from

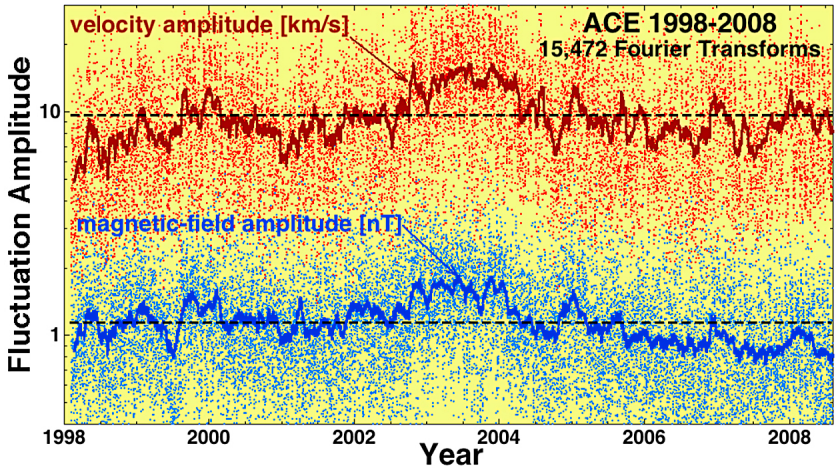

Figure 13. For the years 1998–2008 the amplitude of velocity fluctuations δv (red points) and the amplitude of the magnetic field fluctuations δB (blue points) are plotted as a function of time. One pair of points is obtained from every 4.55-h subinterval in the frequency band $f \geq 1 \times 10^{-3}$ Hz. A 27-day running average of both amplitudes is plotted.

the two formulas and linearly averaging the intercepts gives the excellent fit $\delta b = 1.10\ \delta v + 1.40$ km/s for the relation between the amplitude of the flow and field fluctuations in the solar wind.

[50] In Figure 15 (top) the amplitudes δv and δb of the fluctuations in each 4.55-h subinterval are binned for the 1998–2008 ACE data set. The median values of the distributions are 8.1 km/sec for δv and 11.1 km/sec for δb. The distributions of δv and δb are approximately lognormal (i.e., the distributions of log(δv) and log(δb) are approximately Gaussian). In Figure 15 (bottom) the amplitudes δz_{out} and δz_{in} of the two Elsasser variables are binned. As can be seen, the outward Elsasser fluctuations dominate over the inward fluctuations with the median values of δz_{out} and δz_{in} being 17.7 km/s and 9.4 km/s, respectively.

[51] In Figure 16 (top) the Alfvén ratio $r_A = (\delta v/\delta b)^2$ of the fluctuations is binned for the subintervals of 1998–2008; the solid black curve is for all subintervals and the dashed green curve is for the $N_d = 0$ subintervals (no strong current sheets). As can be seen, r_A is typically less than unity; i.e., δv is typically smaller than δb [cf. *Tu and Marsch*, 1995a, section 2.4.5]. The median value of r_A is 0.58 for $f \geq 1 \times 10^{-3}$ Hz for all subintervals and 0.57 for $N_d = 0$ subintervals.

[52] In Figure 16 (bottom) the amplitude ratio $\delta z_{out}/\delta z_{in}$ is binned for the data subintervals of 1998–2008; the solid curve is for all subintervals and the dashed curves are for various N_d-value subsets of the subintervals. The ratio $\delta z_{out}/\delta z_{in}$ is a measure of the outward-inward imbalance of the solar wind fluctuations and is related to the cross helicity [*Roberts et al.*, 1987; *Podesta and Borovsky*, 2010]. The solid black curve for all data shows the typical dominance of outward signal in the solar wind fluctuations [cf. *Tu and Marsch*, 1995a, section 2.4.3]. The green curve shows that in $N_d = 0$ subintervals the imbalance is only slight (median = 1.27). Examining the green ($N_d = 0$), blue ($3 \leq N_d \leq 5$), and red ($N_d > 5$) dashed curves, the greater the number of strong current sheets in a subinterval the stronger the outward imbalance. Historically it has been known that solar wind current sheets are highly Alfvénic [*Denskat and Burlaga*, 1977; *Vasquez et al.*, 2007] with v-versus-B vector correlations that look like outward propagation [*Neugebauer et al.*, 1984, 1986; *Neugebauer*, 1985]. In the plasma between the strong current sheets, the degree of imbalance may be modest [cf. *Borovsky and Denton*, 2010, Figure 12].

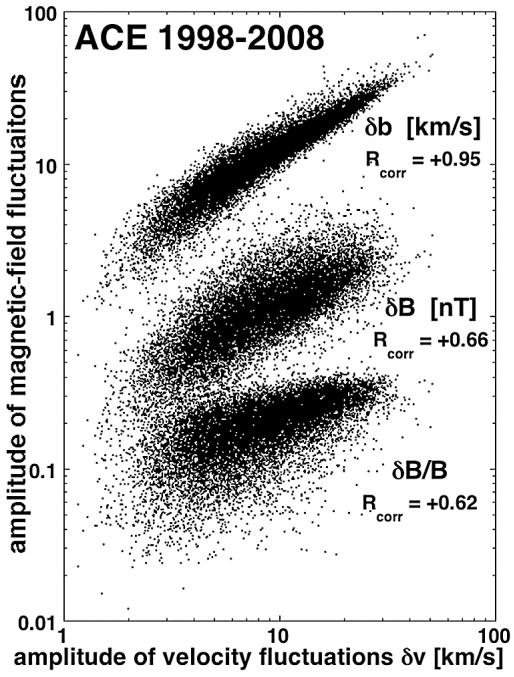

Figure 14. For every 4.55-h subinterval in 1998–2008 the amplitude of the magnetic field fluctuations is measured three different ways (δB, δB/B, and δb) and each is plotted as functions of the velocity amplitude. All amplitudes are measured in the frequency band $f \geq 1 \times 10^{-3}$ Hz. The linear correlation coefficients R_{corr} between the magnetic field amplitudes and the velocity amplitude are indicated on the plot.

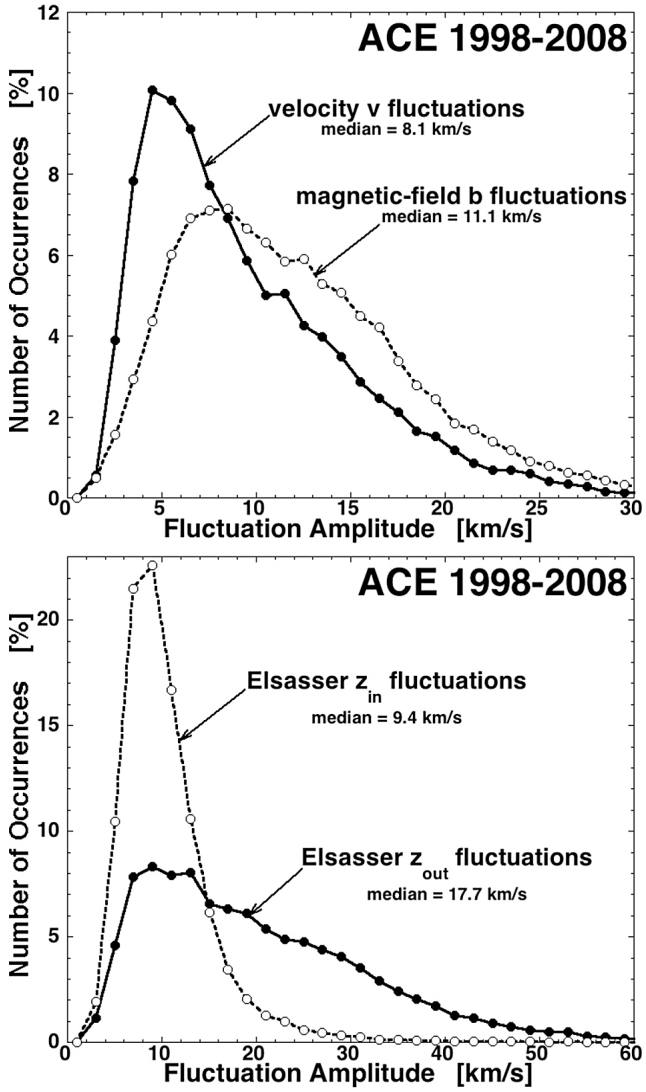

Figure 15. (top) The amplitudes δv and δb of the fluctuations in each 4.55-h subinterval are binned for the 1998–2008. (bottom) The Elsasser-variable amplitudes δz_{out} and δz_{in} of the fluctuations in each 4.55-h subinterval are binned for the 1998–2008. All amplitudes are measured in the frequency band $f \geq 1 \times 10^{-3}$ Hz.

5.2. Dependence of the Fluctuation Amplitudes on Solar Wind Parameters

[53] In Figure 17 the Alfvén ratio $r_A = (\delta v/\delta b)^2$ is plotted as a function of the outward-inward Elsasser ratio $\delta z_{out}/\delta z_{in}$ in that subinterval: the black points are individual values for each 4.55-h subinterval and the red points are a 400-point logarithmic running average of the black points. A strong relation between the r_A and $\delta z_{out}/\delta z_{in}$ is seen (cf. *Tu et al.* [1989a] at 0.3 AU). When $\delta z_{out}/\delta z_{in} = 1$ (when there is balance) there is a minimum to r_A (a minimum of $\delta v/\delta b$) and when $\delta z_{out}/\delta z_{in}$ decreases or increases away from unity (i.e., when there is increasing imbalance) the Alfvén ratio increases toward unity. Hence, when there is balance the magnetic field fluctuations dominate in amplitude over the velocity fluctuations and when there is strong imbalance fluctuations are Alfvénic. The linear correlation coefficient between $\log(r_A)$ and $\log(\delta z_{out}/\delta z_{in})$ is $R_{corr} = +0.43$ for the 1998–2008 ACE data set. A measure of the net imbalance (regardless of inward or outward dominance) is $|\log(\delta z_{out}/\delta z_{in})|$: the linear correlation coefficient between $\log(r_A)$ and $|\log(\delta z_{out}/\delta z_{in})|$ is $R_{corr} = +0.57$.

[54] In Table 7 the linear correlation coefficients between $\log(r_A)$, $\log(\delta z_{out}/\delta z_{in})$ and $|\log(\delta z_{out}/\delta z_{in})|$ and various solar wind parameters are collected for the 1998–2008 ACE data set. As can be seen, variations in the degree of imbalance $|\log(\delta z_{out}/\delta z_{in})|$ are more correlated with variations in solar wind parameters than are variations in $\log(r_A)$. The correlations of $\log(\delta z_{out}/\delta z_{in})$ and $|\log(\delta z_{out}/\delta z_{in})|$ are positive with v_{sw}, T_p, and N_d and quantities related (C_s, S_p, and S_α) and

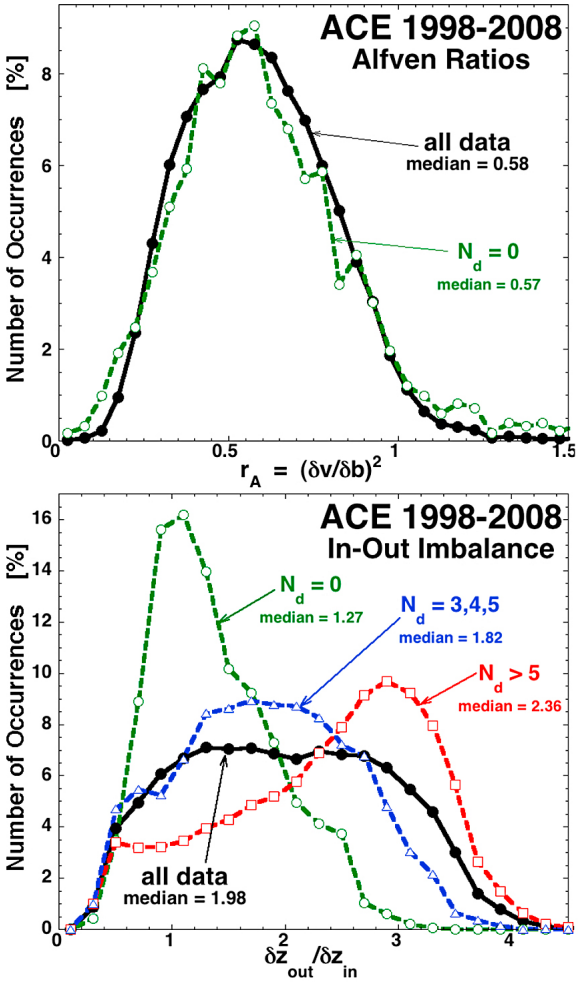

Figure 16. (top) The amplitude ratio $\delta v/\delta b$ is binned for the subintervals of 1998–2008; the black solid curve is for all subintervals and the green dashed curve is for the directional-discontinuity-free ($N_d = 0$) subintervals. (bottom) The outward-inward Elsasser ratio $\delta z_{out}/\delta z_{in}$ is binned for the subintervals of 1998–2008; the black solid curve is for all subintervals, the green curve is for the directional-discontinuity-free ($N_d = 0$) subintervals, the blue curve is for subintervals containing 3, 4, or 5 discontinuities, and the red curve is for subintervals containing 5 or more discontinuities. All amplitudes are measured in the frequency band $f \geq 1 \times 10^{-3}$ Hz.

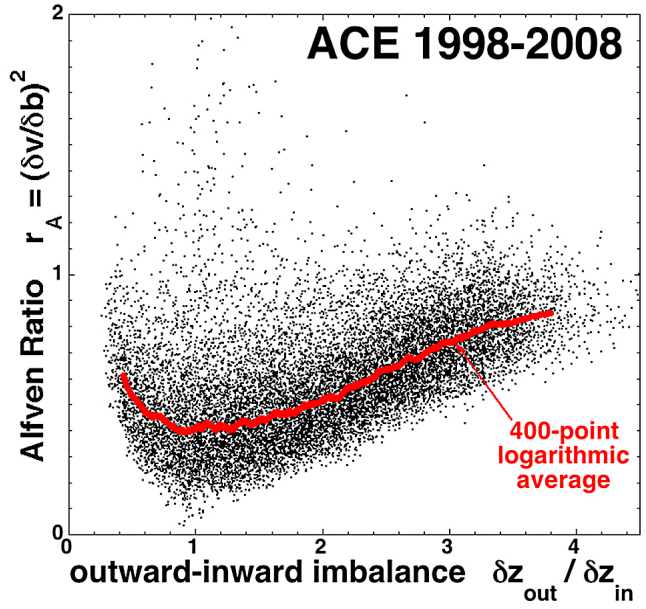

Figure 17. For all of the 4.55-h subintervals of the ACE 1998–2008 data set the Alfvén ratio is plotted as a function of the outward-inward Elsasser ratio (black). A 400-point running logarithmic average of the black points is plotted in red.

the correlations are negative with n, B, C^{6+}/C^{5+}, O^{7+}/O^{6+}, and Fe/O. As was the case for the spectral indices in section 4.2 and Table 4, the strongest of the correlations are with log (C^{6+}/C^{5+}) and log(S_p), which are indicators of plasma type.

[55] In Figure 18 (top) the outward-inward Elsasser ratio $\delta z_{out}/\delta z_{in}$ of each 4.55-h-long data subinterval is plotted (black points) as a function of the proton specific entropy of the solar wind S_p averaged over that 4.55-h subinterval. The linear correlation coefficient between log$(\delta z_{out}/\delta z_{in})$ and log (S_p) is $R_{corr} = +0.46$. To discern the trend in the black points, a 400-point running average of log$(\delta z_{out}/\delta z_{in})$ is plotted in red. As can be seen, there is a clear trend of $\delta z_{out}/\delta z_{in}$ increasing with increasing S_p: solar wind plasma with higher specific entropy is more imbalanced (with outward dominance). In Figure 18 (middle) $\delta z_{out}/\delta z_{in}$ is plotted as a function of the C^{6+}/C^{5+} charge-state ratio. As can be seen from the red 400-point running average, the imbalance (with outward dominance) increases as the charge-state ratio C^{6+}/C^{5+} decreases. In Figure 18 (bottom) the outward-inward Elsasser ratio $\delta z_{out}/\delta z_{in}$ of each 4.55-h-long subinterval is plotted (black points) as a function of the number of strong current sheets N_d in that subinterval. Random numbers between 0.0 and +1.0 have been added to the integer number of strong current sheets per subinterval to spread the points in the plot to make their distribution visible. A 400-point running average is plotted in red to show the trend underlying the black points. As can be seen from the red curve, the imbalance (with outward dominance) increases as the number of strong current sheets per subinterval increases. This agrees with the finding of *Borovsky and Denton* [2010] that the Alfvénicity of strong discontinuities is higher than the Alfvénicity of the plasma between the discontinuities. Note in Figure 18 (bottom), for $N_d \approx 0$ the fluctuations are nearly balanced.

[56] In Figure 19 (top) the amplitudes δv and δb of the fluctuations in each 4.55-h-long data subinterval are plotted as functions of the average solar wind velocity v_{sw} during each 4.55-h subinterval. As can be seen, the amplitude of the fluctuations is strongly correlated with the solar wind velocity: for δv the correlation coefficient with v_{sw} is $R_{corr} = +0.68$, for δb it is $R_{corr} = +0.68$, and for δB (not plotted) it is $R_{corr} = +0.35$. As can be seen from the dark-red and black running averages, the mean value of the fluctuation amplitude increases by a factor of 5 or more as the wind velocity increases by a factor of 2.75. (Cf. section 5.3 for a discussion of this.)

[57] In Figure 19 (bottom) the amplitudes δv (red) and δb (blue) of the fluctuations in each 4.55-h-long data subinterval are plotted as functions of the number of strong current sheets N_d in each subinterval. Random numbers between 0.0 and +1.0 are added to N_d in the plot to spread the points. The fluctuation amplitudes are strongly correlated with N_d; the linear correlation coefficients with N_d are $R_{corr} = +0.58$ for δv, $R_{corr} = +0.58$ for δb, and $R_{corr} = +0.53$ for δB (not plotted). 200-point running averages of the amplitudes are also plotted: the amplitude has an almost-linear dependence on N_d.

[58] In Table 8 the linear correlation coefficients between various measures of the fluctuation amplitudes and various properties of the solar wind are displayed. The various measures used are the amplitudes of the fluctuations (δv, δB, δb, and $\delta E = 0.5 n m_i \delta v^2 + \delta B^2/8\pi$), the amplitudes of the Elsasser-variable fluctuations (δz_{out} and δz_{in}), and the normalized amplitudes of the fluctuations ($\delta v/v_A$, $\delta B/B$, and $\delta E 8\pi/B^2$). As can be seen in the table, there are mixed patterns to the correlations. The basic fluctuation amplitudes δv and δb are strongly positively correlated with v_{sw}, T_p, log(S_p), log(S_α), and N_d and anticorrelated with n, log(S_p), log(S_α), and Fe/O. The correlations of δv and δb are particularly strong with the proton temperature T_p and with related quantities (C_s and log(S_p)). All fluctuation amplitudes are strongly positively correlated with N_d, particularly the normalized amplitudes with correlations exceeding 90%. Besides N_d, the plasma property that has the strongest correlation with the normalized amplitudes is log(C^{6+}/C^{5+}).

Table 7. Linear Correlation Coefficients R_{corr} (in Percent) Between the Logarithms of the Alfvén Ratio r_A and Outward-Inward Elsasser Ratio $\delta z_{out}/\delta z_{in}$ and Several Properties of the Solar Wind and the Turbulence Amplitude

	log(r_A)	log($\delta z_{out}/\delta z_{in}$)	|log($\delta z_{out}/\delta z_{in}$)|
v_{sw}	+22	+34	+43
n	−19	−26	−32
T_p	+15	+37	+40
B	−18	−6	−10
log(S_p)	+23	+46	+53
log(S_α)	+29	+35	+41
β_p	−7	+3	+3
β^*	−9	−22	−24
v_A	−4	+11	+10
C_s^*	+16	+38	+42
N_d	+9	+40	+49
log(C^{+6}/C^{+5})	−33	−48	−52
log(O^{+7}/O^{+6})	−24	−33	−34
Fe/O	−18	−28	−33

[a]The asterisk is a reminder that $T_e = 12.9$ eV is used to calculate β and C_s.

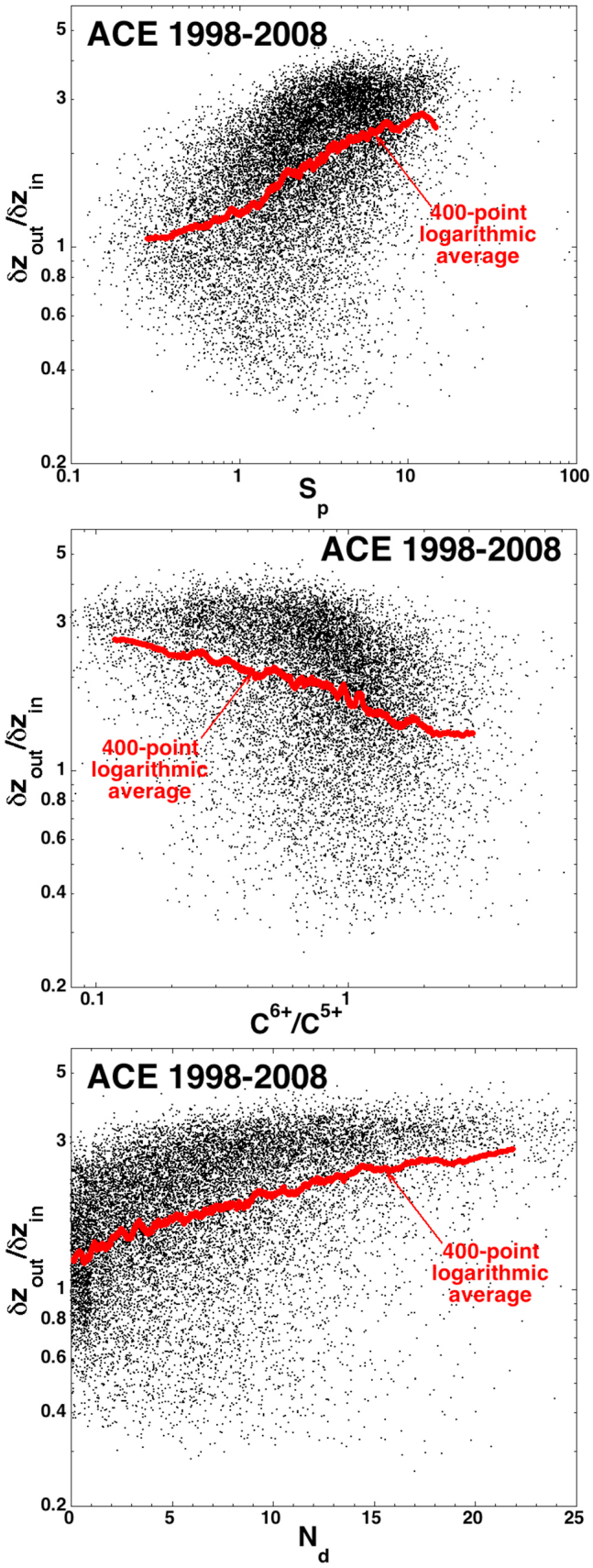

5.3. Dependence of the Fluctuation Amplitudes on the Type of Wind

[59] In Table 5 the median values of the normalized amplitudes $\delta v/v_A$, $\delta B/B$, and $\delta E8\pi/B^2$ are shown for the three types of plasma, using the *Zhao et al.* [2009] method to categorize the wind. The normalized amplitudes are also shown for slow and fast wind and for wind in the restricted speed range 375–425 km/s for the coronal-hole-origin and non-coronal-hole-origin classifications. Before examining these amplitude values, the reader should realize that the fluctuation amplitude measured in frequency space depends on the amplitude of fluctuations in the wind, on the speed of the wind sweeping spatial fluctuations past the spacecraft, and on the steepness of the spectrum. In two parcels of wind with the same amplitude of fluctuations, a larger fluctuation amplitude will be measured in the faster parcel owing to the Doppler shift of the frequency measurement into lower-wave number portions of the spectrum. Hence, systematic variations in the amplitudes of the MHD fluctuations between different types of wind are complicated by systematic differences in the speeds of the different types of wind. To take out some of this Doppler shift, the amplitudes $\delta v/v_A$, $\delta B/B$, and $\delta E8\pi/B^2$ are each shifted to a solar wind velocity of 500 km/s using the median value of v_r with the factor $F = (v_r/500)^{-1.6}$, which approximates the fluctuation spectrum as $k^{-1.6}$ in the Doppler shifting. To perform the shift, the median amplitude $\delta E8\pi/B^2$ is multiplied by F and the median amplitudes $\delta v/v_A$ and $\delta B/B$ are multiplied by $F^{1/2}$. The comparison of the different types of wind are then made with the "shifted" median amplitudes in Table 5. As can be seen in the first three columns, the shifted amplitudes are statistically larger by 10s of per cent in wind of coronal-hole origin than they are in non-coronal-hole-origin wind, and the normalized amplitudes in CME wind is substantially lower than both. The amplitudes $\delta v/v_A$, $\delta B/B$, and $\delta E8\pi/B^2$ are statistically similar for non-coronal-hole-origin plasma (column 1) and slow wind (column 4) and for coronal-hole-origin plasma (column 2) and fast wind (column 5).

[60] Breaking slow solar wind (375–425 km/s) into wind of coronal-hole origin versus non-coronal-hole origin in columns 6 and 7 of Table 5, it is seen that the shifted amplitudes for coronal-hole slow wind (column 7) are more-similar statistically to the shifted amplitudes for coronal-hole wind in general (column 2) than they are to the amplitudes for non-coronal-hole slow wind (column 6). This emphasizes that the difference between slow wind and fast wind is

Figure 18. (top) The outward-inward Elsasser ratio of each 4.55-h-long subinterval is plotted (black points) as a function of the proton specific entropy of the solar wind S_p averaged over the 4.55-h subinterval. The amplitudes going into the Elsasser ratio are measured in the frequency range $f \geq 1 \times 10^{-3}$ Hz. A 400-point logarithmic running average of the black points is plotted in red. (middle) The outward-inward Elsasser ratio (black points) and a 400-point logarithmic running average (red points) are plotted as functions of the alpha-particle specific entropy of the solar wind S_α. (bottom) The outward-inward Elsasser ratio (black points) and a 400-point logarithmic running average (red points) are plotted as functions of the number of directional discontinuities (current sheets) per subinterval N_d.

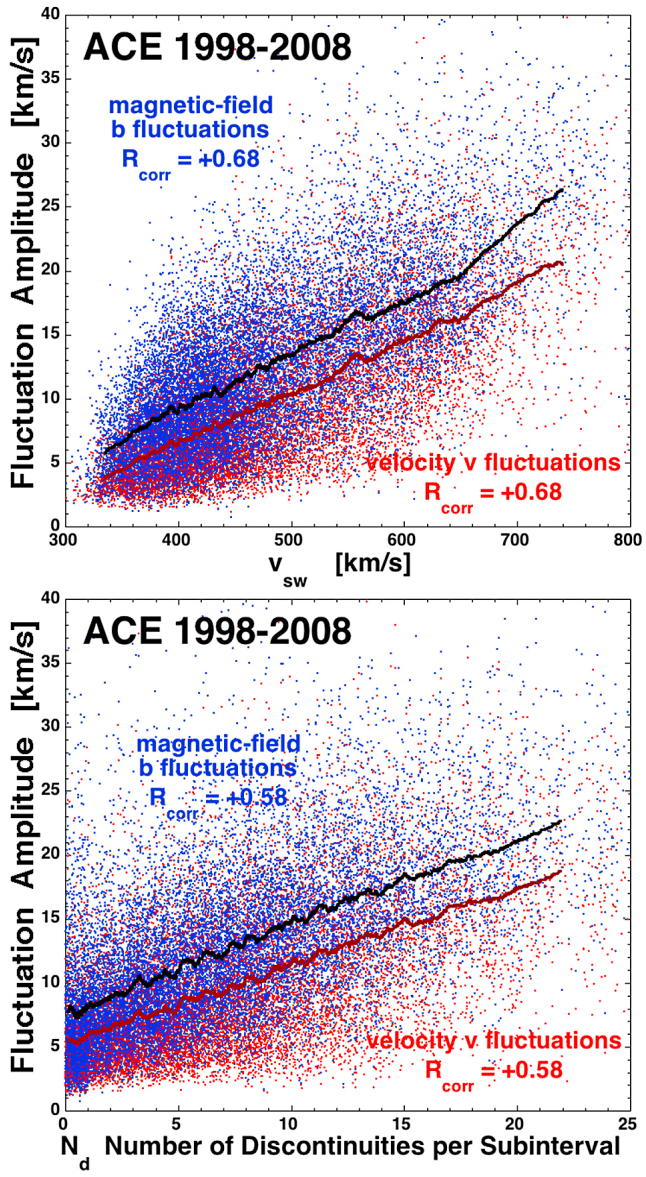

Figure 19. (top) The amplitudes δv (red points) and δb (blue points) of the fluctuations in each 4.55-h-long data subinterval of 1998–2008 are plotted as functions of the solar wind velocity v_{sw}. The amplitudes are measured in the frequency band $f \geq 1 \times 10^{-3}$ Hz. 400-point running averages of δv (pink) and δb (black) are plotted. (bottom) The same quantities are plotted as functions of the number of directional discontinuities (current sheets) per subinterval. Random numbers between −0.5 and +0.5 are added to N_d in the plot to spread the points of the integer values of N_d.

not so much the speed or age of the wind, but rather the difference between coronal-hole-origin plasma (which tends to be fast) versus non-coronal-hole-origin plasma (which tends to be slow).

[61] In Table 5 the median values of the Alfvén ratio r_A and the outward-inward imbalance of the fluctuations $\delta z_{out}/\delta z_{in}$ are displayed for the three types of plasma. Note that these ratios of amplitudes do not suffer from the velocity-dependent Doppler shift described above since the numerator and denominator have the same Doppler variation. The coronal-hole versus non-coronal-hole-origin plasmas show the well-known fast-versus-slow trends [e.g., *Belcher and Davis*, 1971; *Belcher and Solodyna*, 1975; *Horbury and Schmidt*, 1999; *Gulamali and Cargill*, 2001; *Borovsky and Denton*, 2010] wherein the coronal-hole wind has a higher Alfvén ratio and strong outward imbalance than does the non-coronal-hole wind. Note in column 3 that the r_A for CME wind is the lowest and that the degree of imbalance is very low (only 10% above unity).

[62] Breaking slow solar wind (375–425 km/s) into plasma of coronal-hole versus non-coronal-hole origin in columns 6 and 7 of Table 5, it is seen that the r_A and $\delta z_{out}/\delta z_{in}$ for coronal-hole-origin slow wind (column 7) are more-similar statistically to the coronal-hole plasma in general (column 2) than they are to non-coronal-hole slow wind (column 6). Again, this emphasizes that the plasma type is more important than wind speed or wind age.

[63] Note also in the last row of Table 5 that the median number of strong current sheets N_d in the slow wind of coronal-hole origin (column 7) is 6 whereas it is 3 in the slow wind of non-coronal-hole origin (column 6). Accounting for the median wind speed differences in columns 7 and 2, the value $N_d = 6$ of column 7 becomes $6 \times (506/408) = 7.4$ which is comparable to the value $N_d = 9$ in column 2 for coronal-hole-origin wind in general. Again, the coronal-hole versus non-coronal-hole characteristics are more fundamental than the speed-of-wind differences.

5.4. Autocorrelation Functions of the Fluctuation Amplitudes

[64] The temporal autocorrelation functions of the fluctuation amplitudes are explored in Figure 20 along with the autocorrelation functions of various solar wind parameters. Note that these are the autocorrelation functions of the amplitudes of the fluctuations, not the autocorrelation functions of the fluctuating variables. The autocorrelation functions in Figure 20 are corrected for "shot noise" (cf. section 4.3); these corrections range from no correction to 10s of per cent. In Figure 20 (top) the autocorrelation functions of the normalized amplitudes $\delta v/v_A$ (red) and $\delta B/B$

Table 8. Linear Correlation Coefficients R_{corr} (in Percent) Between the Amplitude of the Turbulence in the Solar Wind and Various Properties of the Solar Wind

	δv	δb	δB	δE	δz_{out}	δz_{in}	$\delta v/v_A$	$\delta B/B$	$\delta E 8\pi/B^2$
v_{sw}	+68	+68	+35	+30	+67	+44	+54	+47	+55
n	−24	−19	+36	+33	−23	+2	−16	−9	−14
T_p	+71	+75	+62	+54	+72	+48	+52	+53	+53
B	+23	+35	+60	+57	+26	+50	−17	−20	−16
log(S_p)	+68	+68	+30	+23	+68	+36	+52	+50	+51
log(S_α)	+63	+62	+26	+22	+62	+40	+43	+35	+39
β_p	−3	−3	+7	+3	−2	−10	+38	+54	+45
β*	−36	−38	−24	−19	−36	−31	+5	+15	+8
v_A	+46	+59	+27	+25	+49	+61	−8	−18	−8
C_s^*	+72	+75	+62	+54	+73	+47	+53	+54	+54
N_d	+58	+58	+53	+40	+59	+23	+84	+93	+92
log(r_A)	+44	+14	+3	+9	+32	−19	+49	+11	+28
log($\delta z_{out}/\delta z_{in}$)	+58	+46	+31	+24	+68	−25	+58	+46	+51
log(C^6/C^5)	−51	−43	−29	−23	−51	−1	−61	−58	−58
log(O^7/O^6)	−42	−38	−19	−16	−43	−8	−49	−45	−49
Fe/O	−29	−26	−17	−10	−29	−13	−41	−45	−40

[a]The asterisk is a reminder that $T_e = 12.9$ eV is used to calculate β and C_s.

(blue) are plotted for time shifts of up to 40 days. Note the decay from unity as the time shift Δt increases from 0. Note also the peaks in the autocorrelation functions at 27 days, the solar rotation period. Also plotted in the first panel are the autocorrelation functions of $\log_{10}(S_p)$ (dashed purple) and $\log_{10}(C^{6+}/C^{5+})$ (dashed green). The specific entropy and charge-state ratio are markers of the type of plasma emitted from the Sun; the peaks of the autocorrelation functions of $\log_{10}(S_p)$ and $\log_{10}(C^{6+}/C^{5+})$ at 27 days indicates the tendency for the solar wind plasma type to recur after one 27-day rotation of the Sun [see also *Borovsky and Denton*, 2010, Figure 3]. For the turbulence amplitudes, 27-day peaks are discernible in the autocorrelation functions out to 189 days (7 solar rotations). In the second panel of Figure 20 the autocorrelation functions of $\delta v/v_A$, $\delta B/B$, and $\delta E8\pi/B^2$ are plotted (solid curves) along with the autocorrelation functions of several solar wind parameters (dashed curves). The rate of drop from unity of the autocorrelation functions of the three amplitudes are very similar to the rates of drop from unity of $\log_{10}(S_p)$, $\log_{10}(C^{6+}/C^{5+})$, and N_d, mildly similar to the rate of drop of T_p, and different from the rates of drop of n, B, and v_{sw}. The similarity with the temporal behavior of $\log10(S_p)$, $\log_{10}(C^{6+}/C^{5+})$, and N_d is an indication that the amplitudes of the velocity and magnetic field fluctuations in the solar wind may be related to the type of plasma and to the population of strong current sheets.

[65] In Table 6 the autocorrelation times (persistence times) of the various parameters in Figure 20 (middle) are listed. The autocorrelation times for $\delta v/v_A$, $\delta B/B$, and $\delta E8\pi/B^2$, $\log_{10}(S_p)$, $\log_{10}(C^{6+}/C^{5+})$, and N_d are all similar. Again, this is an indication that the amplitudes of the velocity and magnetic field fluctuations in the solar wind may be related to the type of plasma and to the population of strong current sheets.

[66] In Figure 20 (bottom) the autocorrelation functions of $\log_{10}(r_A)$ and $\log_{10}(\delta z_{out}/\delta z_{in})$ are plotted (solid curves), along with several solar wind quantities (dashed curves). The autocorrelation times appear in Table 6. Note that the autocorrelation function of the outward-inward imbalance is very similar to the autocorrelation function of the number of strong current sheets per subinterval N_d. As in Figure 16 (bottom), this suggests a connection between strong discontinuities in the solar wind and the outward dominance of the solar wind fluctuations [cf. *Borovsky and Denton*, 2010].

6. Discussion

[67] This section contains brief discussions about (1) the variability of the spectral indices of the solar wind, (2) the systematic difference between the velocity spectral index

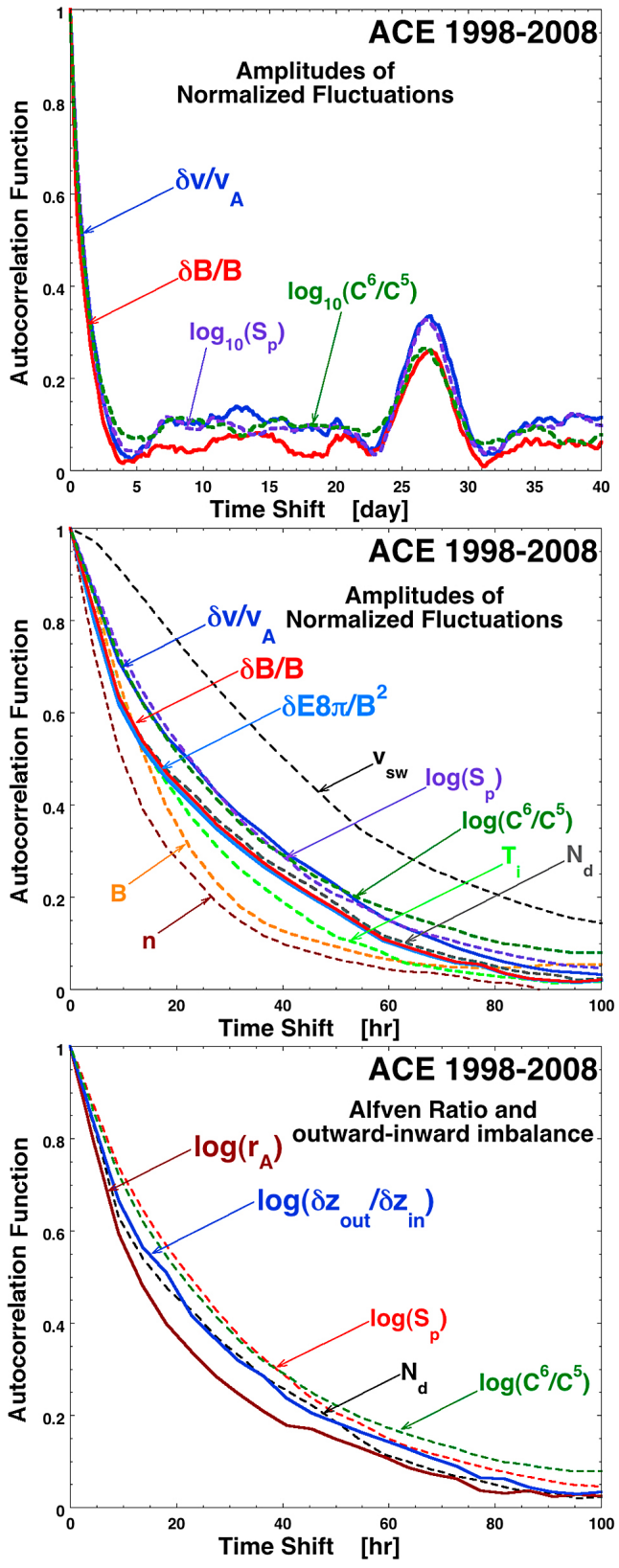

Figure 20. From ACE 1998–2008 measurements, the temporal autocorrelation functions of the normalized fluctuation amplitudes δv, δB, and δb of the solar wind are plotted. The amplitudes are measured in the frequency band $f \geq 1 \times 10^{-3}$ Hz. (top) The autocorrelation functions are plotted for 40 days. (middle) The autocorrelation functions of the fluctuation amplitudes are plotted for 100 h along with the autocorrelation functions of the solar wind speed v_{sw}, the solar wind magnetic field strength B, and the number of directional discontinuities (current sheets) per 4.55-h subinterval N_d. (bottom) The autocorrelation functions for the logarithms of the Alfvén ratio and the outward-inward Elsasser ratio are plotted. All autocorrelation functions are corrected for shot noise and renormalized.

Table 9. A Comparison of the Properties of Regions of the Solar Wind at 1 AU That Exhibit Sustained Shallow Slopes of Trace-B With Regions That Exhibit Sustained Steep Slopes (Median Values Are Shown)

Symbol	Regions of Sustained Shallow Slopes	Regions of Sustained Steep Slopes	Ratio Shallow to Steep	Quantity
slope v	−1.24	−1.48	1:1.2	spectral index of trace-v
slope B	−1.33	−1.95	1:1.5	spectral index of trace-B
slope b	−1.34	−1.91	1:1.5	spectral index of trace-b
slope E	−1.28	−1.75	1:1.4	spectral index of total energy
slope v - slope b	0.076	0.47		difference between v and b spectral indices
slope z_{out}	−1.37	−1.78	1:1.3	spectral index of Elsasser out
slope z_{in}	−1.04	−1.74	1:1.7	spectral index of Elsasser in
δv	18.4 km/s	5.3 km/s	3.5:1	amplitude of velocity fluctuations
δB	1.83 nT	0.75 nT	2.4:1	amplitude of magnetic field fluctuations
δb	21.4 km/s	7.5 km/s	2.9:1	amplitude of magnetic field fluctuations
δE	2.3×10^{-11} erg cm^{-3}	3.6×10^{-12} erg cm^{-3}	6.5:1	amplitude of total-energy fluctuations
δz_{out}	39	10	3.8:1	amplitude of Elsasser-outward fluctuations
δz_{in}	13	8.4	1.5:1	amplitude of Elsasser-inward fluctuations
$\delta v/v_A$	0.24	0.11	2.1:1	normalized velocity amplitude
$\delta B/B$	0.26	0.15	1.9:1	normalized magnetic field amplitude
$\delta E 8\pi/B^2$	0.13	0.036	3.5:1	normalized total-energy amplitude
r_A	0.77	0.48	1.6:1	Alfvén ratio
$\delta z_{out}/\delta z_{in}$	3.2	1.16	2.7:1	outward/inward Elsasser ratio
v_{sw}	582 km/s	387 km/s	1.5:1	solar wind velocity
n	3.4 cm^{-3}	5.9 cm^{-3}	1:1.8	solar wind number density
B	6.6 nT	5.5 nT	1.2:1	solar wind magnetic field strength
T_p	15.0 eV	5.4 eV	3.1:1	solar wind proton temperature
S_p	6.6 eV cm^2	1.4 eV cm^2	4.6:1	proton specific entropy
S_α	500 eV cm^2	80 eV cm^2	6.2:1	alpha-particle specific entropy
β_p	0.49	0.44	1.1:1	proton beta
v_A	80 km/s	48 km/s	1.7:1	Alfvén speed
N_d	11	3	3.7:1	number of strong discontinuities per subinterval
C^{+6}/C^{+5}	0.45	1.1	1:2.3	charge-state ratio of carbon
O^{+7}/O^{+6}	0.072	0.25	1:3.4	charge-state ratio of oxygen
Fe/O	0.062	0.11	1:1.7	iron to oxygen density ratio

and the magnetic field spectral index, (3) comparing the measured total-energy spectral index to expectations from turbulence theories, and (4) future work that is needed.

6.1. The Variability of the Spectral Indices of the Solar Wind

[68] Throughout this study the reader has seen temporal variations in the spectral indices of the velocity, magnetic field, and total energy fluctuations of the solar wind. There are two aspects to the variations of the spectral indices in the present study: (1) shot-to-shot measurement variations owed to mathematical variance errors introduced into the PSDs formed from finite data records and the fitting over finite frequency ranges to determine spectral slopes and (2) systematic variations that are day-to-day or longer. The magnitude of the shot-to-shot variations is discernible in Figure 4 where the frequency range of fitting is varied. The nature of those shot-to-shot variations is analyzed in Appendix A. The timescales of the systematic variations are indicated in the autocorrelation-function examination of Figures 12 and 20 and the properties of the systematic variations can be discerned in the averaging used in Figures 9–11 and 17–19.

[69] The systematic variation at 1 AU shows a 27-day tendency to repeat the properties (spectral indices, amplitudes, outward-inward imbalance, etc.) of the fluctuations. This can be discerned in Figures 9, 12, and 20. There is a well-known tendency to observe similar types of plasma at 1 AU separated by the 27-day rotation period of the Sun as seen from Earth. This is an indication that the properties of the fluctuations in the solar wind are to some degree controlled by (or characterizable by) the properties of the plasma.

[70] Two extremes of the systematic spectral-index variations can be analyzed: (1) "steepest-slope intervals" and (2) "shallowest-slope intervals." In Table 9 the median values of the properties of the solar wind plasma and fluctuations in the ACE data set are compared for these two types of intervals. The data used for the shallowest-slope intervals comes from all intervals in the 1998–2008 time series wherein the 1-day running average of the trace-B spectral index is shallower than −1.38; the data used for the steepest-slope intervals comes from intervals in the time series when the 1-day running average of the trace-B spectral index is steeper than −1.91.

[71] Contrasting the steepest-slope regions of the solar wind with the shallowest-slope regions, Table 9 indicates that the steepest-slope regions have steeper spectral indices of v, B, b, and E; have a large difference between the spectral index of v and that of b; have substantially lower-amplitude fluctuations δv, δb, δB, δE, δz_{out}, and δz_{in}; have substantially lower amplitude normalized fluctuations $\delta v/v_A$, $\delta B/B$, and $\delta E 8\pi/B^2$; have slightly smaller Alfvén ratios, and have substantially lower outward-inward Elsasser ratios, close to balanced. The plasma properties of the steepest-slope regions of the solar wind are characterized by higher densities, substantially cooler temperatures, and substantially lower proton specific entropies. The steepest-slope regions of the solar wind are also characterized by higher

O^{7+}/O^{6+} and C^{6+}/C^{5+} ratios, meaning higher coronal temperatures. The solar wind speed for the steepest-slope plasmas are much lower and the number of density of strong current sheets is substantially lower, but not zero.

[72] The statistical difference in the solar wind speed for the shallowest-slope versus steepest-slope regions is consistent with a difference between fast solar wind and slow solar wind. The statistical difference in the O^{7+}/O^{6+} charge-state ratio is consistent with a difference between coronal-hole-origin plasma and slow non-coronal-hole-origin plasma [cf. *Zhao et al.*, 2009]. Using the *Zhao et al.* [2009] classification scheme from the O^{7+}/O^{6+} measurements, it is found that the shallowest-slope regions are categorized as 86% coronal-hole origin, 8% non-coronal-hole origin, and 6% ejecta and that the steepest-slope regions are categorized as 21% coronal-hole origin, 66% non-coronal-hole origin, and 13% ejecta. These values are entered into Table 1 for a comparison with the occurrence frequency of categories for all data subintervals. The shallowest-slope regions (row 3) certainly emphasize coronal-hole-origin plasma. The steepest-slope regions (row 4) emphasize non-coronal-hole-origin plasma and ejecta, with approximately the same ratio of occurrence (5.1 to 1) as in the all-data collection (5.3 to 1, see row 1).

[73] Researchers should be cautioned about the interpretation of spectra obtained from long (a day or more) intervals of solar wind measurements: these spectra can contain mixed contributions from plasmas having differing fluctuation properties.

6.2. The Difference Between the Velocity and Magnetic Field Spectral Indices

[74] Throughout this study a systematic difference between the spectral indices of the trace-v and trace-b (or trace-B) spectra has been seen. The magnetic field spectrum tends to be steeper than the velocity spectrum. This difference has been seen in prior solar wind studies [*Podesta et al.*, 2007; *Tessein et al.*, 2009; *Salem et al.*, 2009; *Borovsky and Denton*, 2010; *Podesta and Borovsky*, 2010; *Boldyrev et al.*, 2011], with some of those studies having noted the size of the spectral difference being correlated with solar wind speed. In the present study that solar wind speed correlation is also seen, however the spectral-index difference shows stronger correlations with other plasma properties and with several fluctuation-amplitude measures (see Table 4).

[75] Seven possible reasons for this difference between the v and b spectral indices were considered by *Borovsky and Denton* [2010], all explanations dealing with complications to the homogeneous, stationary, isotropic, incompressible picture used to derive Kolmogorov spectra for MHD turbulence.

[76] In addition to these seven reasons, *Boldyrev et al.* [2011] suggest that the difference in the v and B spectral indices may be owed to the accumulation of magnetic helicity at large scales in MHD turbulence. In the MHD simulations of *Boldyrev et al.* [2011] the amount of difference between the v and b spectral indices varied with the degree of imbalance of the turbulence.

[77] In *Borovsky and Denton* [2010] the role of the mixture of discontinuity (current-sheet) signal to other signals in the solar wind time series was not considered as clues to the variable spectral difference between v and b, however they observed that more-Alfvénic solar wind statistically has a smaller difference between the spectral indices of v and b (cf. Figures 13 and 14). Individual solar wind tangential discontinuities are known to be Alfvénic [*Neugebauer*, 1985; *Neugebauer et al.*, 1986; *Neugebauer and Alexander*, 1991]: *Borovsky and Denton* [2010] found that the population of discontinuities (current sheets) in the solar wind are much more Alfvénic (with strong outward dominance) than are the fluctuations in the solar wind plasma between the strong discontinuities. In Figures 10 and 11 it was seen that when the solar wind plasma has a high density of strong current sheets the difference in spectral index between v and b becomes small and where the plasma has a low density of strong discontinuities the difference becomes large. Pertinent to this, *Li et al.* [2011] found evidence in Ulysses measurements that the presence of strong current sheets in solar wind Fourier transforms Kraichnan $-3/2$ magnetic field spectra into Kolmogorov $-5/3$ spectra; however, the effect of current sheets on the difference between the v and b spectra were not studied.

6.3. Observed Total-Energy Spectral Indices and Turbulence Theories

[78] In section 4 and Appendix A it is concluded that the average spectral index of the total energy $E = m_i n v^2/2 + B^2/8\pi$ of the solar wind is -1.52 and that the distribution of measured total-energy spectral indices for the ACE 1998–2008 data set is consistent with the Kraichnan $-3/2$ spectrum rather than the Kolmogorov $-5/3$ spectrum.

[79] A naive interpretation would be that the ACE measurements support a picture in which Kraichnan-type isotropic MHD turbulence with the Alfvén effect acting to weaken eddy-eddy interactions [*Iroshnikov*, 1964; *Kraichnan*, 1965] over a simple Kolmogorov-type isotropic MHD turbulence [*Fyfe et al.*, 1977; *Hatori*, 1984]. Or that the ACE measurements support a picture of Boldyrev-type anisotropic turbulence with scale-dependent v-B alignments [*Boldyrev*, 2006; *Podesta and Bhattacharjee*, 2010; *Podesta*, 2010] over simpler critical-balance turbulence [*Goldreich and Sridhar*, 1997].

[80] Note however that the spectral index of the total energy E varies with solar wind plasma properties, complicating any assessment of turbulence models with global solar wind data. The total-energy spectral index at 1 AU tends to be shallower than -1.5 for coronal-hole wind with high proton specific entropy, a large density of strong current sheets, an Alfvén ratio approaching unity, and an outward dominance of fluctuations (see Table 5). And, the total-energy spectral index at 1 AU tends to be steeper than -1.5 for slow non-coronal-hole-origin plasma with low proton specific entropy, low numbers of strong current sheets, an Alfvén ratio much less than unity, and an outward-inward balance to the fluctuations (see also Table 5).

[81] Note also that the signal from strong current sheets in the solar wind has not been separated out of the solar wind-fluctuation spectra analyzed here (or anywhere else). Solar wind strong directional discontinuities on average carry half or more of the spectral energy of the solar wind magnetic field fluctuations [*Siscoe et al.*, 1968; *Borovsky*, 2010a] and likely a similar fraction for the velocity fluctuations. Arguments can be made that these strong current sheets are

plasma boundaries in the solar wind and not an aspect of MHD turbulence in the wind. This is particularly the case for non-coronal-hole solar wind [*Borovsky*, 2012a, 2012b]. If it is the case that the strong current sheets are not part of the turbulence, then the signal from turbulent fluctuations in the solar wind is masked in the power spectrum of the strong discontinuities and the observed spectral index may or may not be indicative of the properties of turbulence in the solar wind.

6.4. Future Work Needed

[82] Discerning turbulence from other structures in the solar wind has been an issue for decades [cf. *Siscoe et al.*, 1968; *Sari and Ness*, 1969; *Bavassano and Bruno*, 1991; *Tu and Marsch*, 1991, 1994, 1995a; *Bruno and Carbone*, 2005; *Bruno et al.*, 2007; *Borovsky*, 2008, 2010a; *Li et al.*, 2011; *Owens et al.*, 2011], particularly since it has been argued that some types of solar wind structures are fossils from the Sun [e.g., *Mariani et al.*, 1983; *Thieme et al.*, 1988, 1989, 1990; *Feldman et al.*, 1993; *Woo and Habbal*, 1998; *Reisenfeld et al.*, 1999; *Yamauchi et al.*, 2002, 2003; *Borovsky*, 2008]. Before turbulence in the solar wind can be accurately studied, a true picture of the physical nature of the fluctuations in the solar wind must be obtained. The nature of the fluctuations must be understood before solar wind evolution, energetic-particle transport, and solar wind driving of the Earth's magnetosphere can be correctly calculated. A methodology to discern true MHD turbulence from the ubiquitous tangential discontinuities, pressure-balance structures, magnetic holes, ejecta, and other fossils from the Sun must be developed and the contribution of each type of fluctuation to the Fourier spectra and structure functions of the solar wind needs to be understood. In particular, a determination of the nature and origin of strong current sheets is needed.

7. Summary

[83] In this report velocity fluctuations and magnetic field fluctuations in the solar wind at 1 AU were examined using measurements from the ACE spacecraft in the years 1998–2008. The method of analysis was to break the 10-year data set into 20,076 subintervals that were each 4.55 h long and to analyze each subinterval separately using Fourier-transform techniques. The results of the individual analyses were then statistically analyzed as an ensemble of realizations of the turbulence of the solar wind. The information obtained is summarized below.

7.1. Current Sheets in the Solar Wind Plasma

[84] 1. There is an average of 6 strong ($\Delta\theta > 45°$) discontinuities (current sheets) per 4.55-h data subinterval in the 1998–2008 ACE data set.

[85] 2. Strong-current-sheet free intervals ($N_d = 0$) are relatively rare: only 13.4% of the subintervals have $N_d = 0$.

[86] 3. Strong-discontinuity-free subintervals are associated with coronal-mass-ejection plasma and non-coronal-hole-origin (streamer-belt) plasma.

[87] 4. Intervals with very large numbers of strong discontinuities are associated with coronal-hole-origin wind.

7.2. Spectral Indices

[88] 1. The spectral index of the velocity fluctuations is consistently shallower than the spectral index of the magnetic field fluctuations, with the total-energy spectral index in between.

[89] 2. For the 1998–2008 solar wind ensemble, the distributions of spectral indices are -1.62 ± 0.49 for the magnetic field, -1.41 ± 0.39 for the velocity, and -1.52 ± 0.39 for the total energy.

[90] 3. These values of the spectral indices are supported by fits to ensemble-averaged spectra and by fits to single large spectra.

[91] 4. Numerical experiments indicate that the mean value of the spectral-index ensemble should be used as the correct spectral index.

[92] 5. The spectral indices of the solar wind fluctuations vary with the type of solar wind plasma at the measuring satellite. The magnetic field spectral index varies more with plasma type than does the velocity spectral index. Some of the slope variation of the magnetic spectra could be owed to movement of the spectral breakpoint into the range of frequencies analyzed.

[93] 6. The total-energy spectral index (-1.52) is shallower than the Kolmogorov $k^{-5/3}$ slope and it is consistent with the Kraichnan $k^{-3/2}$ slope. But note that the total-energy spectral index varies systematically with the type of plasma.

[94] 7. The spectral index of the z_{out} Elsasser variable tends to be steeper than the spectral index of z_{in}. In the absence of strong current sheets the two spectral indices tend to be equal.

[95] 8. The total-energy spectral index varies with the plasma proton specific entropy S_p, with the carbon and oxygen charge-state ratios C^{6+}/C^{5+} and O^{7+}/O^{6+}, and with the number of strong discontinuities (current sheets) per data subinterval N_d. High-specific-entropy and high-N_d plasmas have shallower than -1.5 total-energy spectra and low-specific-entropy and low-N_d plasmas have steeper than -1.5 total-energy spectra.

[96] 9. The difference between the spectral slopes of v and of B is reduced in high-specific-entropy and high-N_d plasmas.

[97] 10. Systematic differences are seen in the spectral indices between coronal-hole-origin plasma, non-coronal-hole-origin plasma, and CME plasma. The spectral indices are in general steeper in non-coronal-hole plasmas than they are in coronal-hole plasmas.

[98] 11. The systematic differences in the spectral indices between fast and slow wind is owed to the differences between coronal-hole and non-coronal-hole plasma. The spectral indices of slow wind of coronal-hole origin resemble more the indices of coronal-hole wind in general rather than of slow wind in general.

[99] 12. Weak solar-cycle trends are seen in the spectral indices of the solar wind fluctuations.

[100] 13. The autocorrelation times for the spectral indices of the solar wind fluctuations are 20–30 h, similar to the autocorrelation times for the properties of the solar wind plasma; i.e., the spectral indices vary from day to day as the plasma changes.

7.3. Fluctuation Amplitudes

[101] 1. The amplitudes δv and δb of the velocity and magnetic field fluctuations both vary with time in the solar wind. They vary together with a linear correlation coefficient $R_{corr} = +0.95$.

[102] 2. The amplitudes δv and δb are approximately log-normally distributed in the 1998–2008 ACE measurements.

[103] 3. There is a distinct solar-cycle trend to the fluctuation amplitudes with the amplitudes largest in 2003, a year in the declining phase with strong high-speed-stream occurrence.

[104] 4. The amplitude δz_{out} of the Elsasser variable z_{out} usually dominates the amplitude δz_{in} of the variable z_{in}, yielding an outward-inward Elsasser ratio $\delta z_{out}/\delta z_{in}$ that is outward dominant.

[105] 5. For subintervals without strong current sheets ($N_d = 0$), the outward-inward Elsasser ratio $\delta z_{out}/\delta z_{in}$ tends to be near unity, meaning the fluctuations are nearly balanced, and the spectral indices of the z_{out} and z_{in} Elsasser variables tend to be equal. For subintervals containing strong current sheets ($N_d > 0$), the outward-inward Elsasser ratio $\delta z_{out}/\delta z_{in}$ is greater than unity, meaning the fluctuations are outward imbalanced.

[106] 6. The outward imbalance increases with the density of strong current sheets N_d in the plasma and increases with the proton specific entropy of the plasma.

[107] 7. The Alfvén ratio $r_A = (\delta v/\delta b)^2$ of the fluctuations is almost always less than unity.

[108] 8. The fluctuation amplitudes increase linearly with the number of strong current sheets N_d per subinterval.

[109] 9. The normalized amplitudes $\delta B/B$, $\delta v/v_A$, and $\delta E 8\pi/B^2$ all increase with increasing solar wind speed, with increasing proton temperature, and with number of strong current sheets and the normalized fluctuation amplitudes increase with decreasing number density, decreasing magnetic field strength, and decreasing C^{6+}/C^{5+} and O^{7+}/O^{6+} charge-state ratios.

[110] 10. Systematic differences are seen in the Alfvén ratio and outward-inward imbalance between coronal-hole-origin plasma, non-coronal-hole-origin plasma, and CME plasma. The imbalance is larger for coronal-hole plasmas.

[111] 11. The systematic differences in the Alfvén ratio and outward-inward imbalance between fast and slow wind is owed to the differences between coronal-hole and non-coronal-hole plasma. The Alfvén ratios and degrees of imbalance of slow wind of coronal-hole origin resemble those of coronal-hole wind in general rather than those of slow wind in general.

[112] 12. The autocorrelation times of the amplitudes of the solar wind fluctuations are in the range 11–37 h, similar to the autocorrelation times for the properties of the solar wind plasma.

[113] 13. The autocorrelation times of the amplitudes $\delta B/B$, $\delta v/v_A$, and $\delta E 8\pi/B^2$ of the fluctuations are approximately equal to the autocorrelation times of the solar wind proton specific entropy, the number density of strong current sheets, and the carbon and oxygen charge-state ratios.

[114] 14. The autocorrelation times for the Alfvén ratio and outward-inward Elsasser ratio of the fluctuations are also approximately equal to the autocorrelation times of the proton specific entropy, the density of strong current sheets, and the carbon and oxygen charge-state ratios.

7.4. Data Analysis Methods

[115] 1. An analysis of numerical experiments simulating the ACE power spectra with variance error finds that for a large number of measurements of the spectral index, the mean of the distribution of measurements is the significant quantity and it is determined to an accuracy that is much less than the standard deviation of the measurements. The mean value is supported by comparison with fits to ensemble-averaged spectra and fits to single spectra created from long time series.

[116] 2. In an ensemble of measurements, the best estimate of the spectral index is *not* obtained by keeping only those spectral-index fits with the highest R_{corr} values.

[117] 3. For an ensemble of spectra, direct FFT methods using linear detrend of the data provide less statistical noise than FFT methods using tapered windows.

Appendix A: Interpreting the Ensemble of Spectral Indices Obtained From Spectra With Variance Error

[118] Constructing a PSD from a finite record of data introduces "statistical error" or "variance error" into the PSD, which affects the spectral fit of the PSD. In Appendix A we will work to interpret the spectral fitting of FFT-generated PSDs (periodograms) so that we can better interpret the statistics of the ensemble of spectral indices obtained by fits to the 20,076 ACE PSDs. To this end, two sets of computational experiments are utilized. Via these experiments with synthetic PSDs that have known values underlying controlled amounts of variance we will learn about the properties of spectral-index measurements. The ultimate purpose is to learn how to determine the underlying PSD despite the variance errors.

[119] For each 4.55-h data subinterval in the 1998–2008 ACE data set, PSDs were calculated using FFTs and the FFT-generated PSDs were linear-regression fit in log-log space over the frequency range $f = 4.3 \times 10^{-4}$ Hz to $f = 1.9 \times 10^{-3}$ Hz (see section 4), where the slope of the linear-regression fit is the spectral index.

[120] Owing to the fact that the individual PSDs are formed from finite time intervals of data, the Fourier transforms are convolutions of the true spectrum with the time window [*George*, 1978; *Otnes and Enochson*, 1972, section 7.1]. This convolution introduces a highly oscillating "spectral variance" into each PSD. The individual values of the FFT-generated PSD are equal to the product of the true PSD times a random function with amplitude proportional to the local value of the true PSD [cf. *Jenkins and Watts*, 1968, section 6.4.1; *Bloomfield*, 1976, sections 8.4 and 8.5; *Marple*, 1987, Appendix 4.A; *Kaimal et al.*, 1989]. The constant of proportionality is of order unity. In the logarithm of the FFT-generated PSD, this product looks like the true PSD (which is frequency dependent) plus a random number (with an amplitude that is frequency independent). For the solar wind, this noisy form of the PSD can be seen by examining unsmoothed power spectral densities (Figure 7)

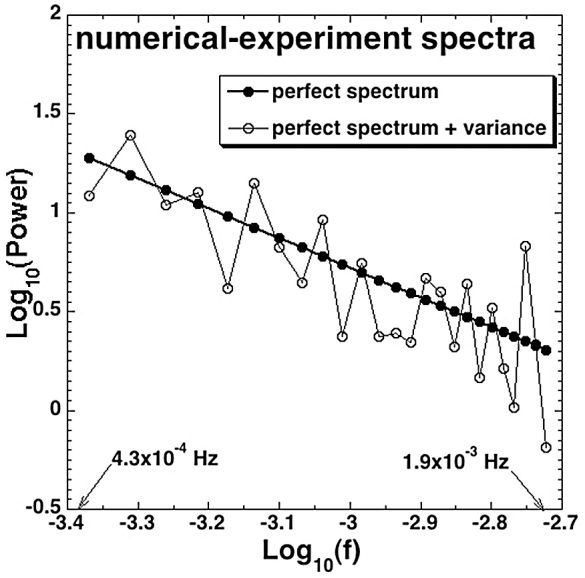

Figure A1. For the numerical experiments, an artificial PSD is shown. The artificial PSD (hollow points) is constructed from a perfect PSD $Cf^{-3/2}$ (solid points) by adding random numbers to simulate variance error.

[e.g., see *Tu and Marsch*, 1995a, Figure 2.2; *Bruno and Carbone*, 2005, Figure A3].

[121] Note that the amplitude of the variance error in a PSD is independent of the number of data points going into the Fourier transform, i.e., it is independent of the length of the time window [cf. *George*, 1978; *Fougere*, 1985; *Marple*, 1987, Appendix 4.A]. The amplitude of the variance error is dependent however on the shape of the time window [cf. *Jenkins and Watts*, 1968, Table 6.6; *Harris*, 1978]. Commonly this PSD variance is averaged away by summing independent PSDs [*Welch*, 1967; *Williams*, 1981, section E.2.2] or averaged away with spectral smoothing in frequency space [*Kay and Marple*, 1981, section 4.E; *Brillinger*, 1981, section 5.4], as was done in Figures 6 and 7 respectively. In the bulk of the present study the spectral noise is not removed.

[122] In the numerical experiments of this appendix, artificial PSDs are created that resemble the PSDs from ACE (but without variance) and variance is added in controlled fashions to see the effects of variance error on the spectral-index fits to the PSDs and to gain information about how to interpret the ensemble of spectral-index fits. We will pay attention to two quantities in the ACE data analysis and in the experiments: (1) the slope of the linear fit in log-log space and (2) the linear correlation coefficient R_{corr} of the fit.

[123] An artificial PSD is shown in Figure A1. The solid points are for the perfect PSD $Cf^{-3/2}$ without variance, where $C = 1.66 \times 10^{-4}$ is a constant. Note in Figure A1 that the points are spaced in frequency exactly like the ACE PSDs. A linear fit (in log-log space) to the black points will yield a slope -1.5 and a correlation coefficient $R_{corr} = -1.0$. The magnitude of the correlation coefficient being unity means that 100% of the variance of $\log_{10}$(PSD) is described by a variation of $\log_{10}$(f). The solid curve with the hollow points in Figure A1 is an artificial PSD created by adding random numbers (noise) to the logarithm of the perfect PSD represented by the solid points. Analysis of the variance error of periodograms assumes that it is random and has a zero mean [cf. *Otnes and Enochson*, 1972, section 5.3]. The random numbers are drawn from a zero-mean boxcar distribution of random numbers between $-A/2$ and $+A/2$, where A is a constant (the amplitude of the random-number set). To match the properties of the spectral variance in FFT-generated PSDs, the random-number amplitude is independent of the frequency f. Since random variance was added to the perfect PSD, the correlation coefficient R_{corr} will have a magnitude less than unity, i.e., all of the variation of $\log_{10}$(PSD) is not described by a variation of $\log_{10}$(f).

[124] When variance is added to a perfect PSD, two things happen. (1) The slope of the noise (added variance) adds to the slope of the perfect PSD; the slope (spectral index) of the noise-added spectrum can be greater or less than the slope of the perfect spectrum depending on whether the slope of the noise is positive or negative. (2) The linear correlation coefficient of the fit is lowered when the variance is added; the larger the amplitude of the variance, the more the coefficient is lowered. Note that for a given amplitude of noise added to the perfect spectrum, if the slope of the noise is of the same sign (negative) as the slope of the perfect spectrum then the resulting correlation coefficient will be larger in magnitude than it would be if the slope of the noise was of opposite sign to the slope of the perfect spectrum.

[125] For the next few paragraphs, Figure A2 is described. Plotted in red and blue, respectively, are parameters of the spectral fits to the ensemble of ACE velocity and magnetic field PSDs. Every 4.55-h-long data subinterval yields a velocity PSD and a magnetic field PSD, and these are independently fit with least squares linear-regression lines in $\log_{10}$(PSD) versus $\log_{10}$(f) space from $f = 4.3 \times 10^{-4}$ Hz to 1.9×10^{-3} Hz. Each PSD yields a spectral index (slope of the fitting line) and a linear correlation coefficient R_{corr}. The spectral index is plotted in Figure A2 as a function of R_{corr}. Each population of PSDs forms a diagonal band in the plot. Numerical experiments with artificial spectra are performed to interpret the bands.

[126] The green points plotted in Figure A2 are from one numerical experiment. Here 10,000 identical perfect spectra (with $-3/2$ spectral index) were created and to each spectrum random noise was added. Each time the amplitude of the noise was the same, but the numbers were newly randomized. Lines were fit to each of the 10,000 noisy spectra: the spectral indices and R_{corr} values of the 10,000 fits are plotted (green points) in Figure A2. As can be seen, sometimes the slope of the noisy spectra are steeper than the -1.5 perfect slope and sometimes they are sallower. When they are steeper R_{corr} is higher (closer to -1) than when they are shallower. The numerical-experiment points (green) representing an ensemble of constant-amplitude-noise cases forms a diagonal band which overlies the diagonal bands of the ACE velocity PSDs (red) and the ACE magnetic field PSDs (blue).

[127] A second set of numerical experiments is performed, represented by the yellow curves in Figure A2. Here, five perfect PSDs (with $-3/2$ spectral index) are created and five sets of random numbers are created, one set for each perfect PSD. The random number sets are repeatedly multiplied by a

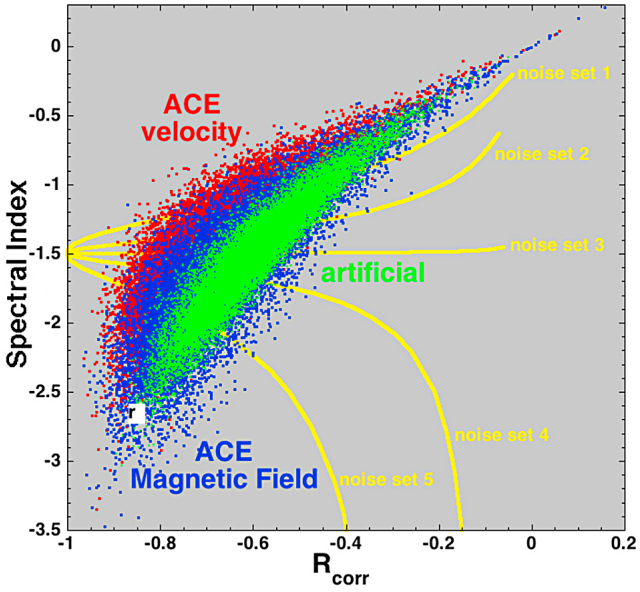

Figure A2. For two sets of numerical experiments with artificial PSDs, the spectral indices of the PSDs obtained from fits of $\log_{10}$ (PSD) versus $\log_{10}$ (f) are plotted as functions of the correlation coefficient between $\log_{10}$ (PSD) and $\log_{10}$ (f). The red and blue points are for the spectral fits to the ensemble of 1998–2008 ACE velocity and magnetic field PSDs. The green points are for spectral fits to an ensemble of 10000 artificial PSDs formed by perfect spectra (with −3/2 spectral index) plus random noise. Each of the 10000 artificial spectra has the same amplitude noise. The five yellow curves are produced by five perfect PSDs (with −3/2 spectral index) plus five sets of random numbers. The random number sets are repeatedly multiplied by a variable amplitude and added to the perfect PSDs, whence they are fit and the slopes and R_{corr} values are plotted to make the five curves.

variable amplitude and added to the perfect PSDs, whence they are fit and the slopes and R_{corr} values are plotted for the five perfect PSDs as the five yellow curves in Figure A2. Let us first focus on the middle yellow curve (noise set #3). In this case the slope of a line fit to the noise alone is very near to zero. When the amplitude of the added noise is infinitesimally small, the resulting fits yield a slope −1.5 and a correlation coefficient $R_{corr} = -1$ (left-hand edge of the figure). As the noise amplitude gets larger, the correlation coefficient is reduced from −1, but since the slope of the noise is near zero, the noise neither adds nor subtracts from the slope of the perfect PSD; hence the slope of the noisy PSD remains at −1.5 regardless of the amplitude of the noise. For noise sets #4 and #5, the slope of a fit to the noise alone is <0. When the amplitudes of the noise sets are infinitesimally small, the slope of the noise-added PSDs are again −1.5 with $R_{corr} = -1$. As the amplitudes of the added noise sets increase, the correlation coefficient is reduced from −1 and the slope of the noise adds to the slope of the perfect PSD so the slopes of the noise-added PSDs are steeper than −1.5. This is shown by the behavior of the yellow curves for noise sets #4 and #5 in Figure A2. As the noise amplitudes are increased further, eventually the noise dominates and the yellow curves asymptote to the R_{corr} value of the noise and to infinite negative slope corresponding to infinitely loud noise. For noise sets #1 and #2, the slope of a line fit to the noise alone is >0 so the added noise will tend to flatten the spectral slope of the PSD. Again, when the amplitudes of these noise sets is infinitesimally small the spectral index of the noise-added PSD is −1.5 with R = −1. As the noise amplitude increases R_{corr} is reduced from −1 and the slopes of the noise counteract the slope of the perfect PSD to make a slope shallower than −1.5. The yellow curves for noise sets #1 and #2 reflect this behavior. As the added noise amplitude is larger and larger, the yellow curves will asymptote to the (positive) R_{corr} values of the noise sets with infinite positive slopes corresponding to infinitely loud noise.

[128] These behaviors in the two types of numerical experiments are demonstrated in Figure A3, where the 5 yellow curves of Figure A2 are redrawn in black. Six ensembles of a perfect −3/2 PSD plus variance are made, with each ensemble having a different amplitude of variance (noise). The noise levels range from very small (0.2) to very large (10). As can be seen, in each case a diagonal band of point results on the spectral-index versus R_{corr} plot, with the black curves tracking the shape of the band.

[129] In Figures A2 and A3, the perfect answer for the spectral index of the PSDs with variance error lies where the yellow curves converge at the left-hand edge of the plot. One might (incorrectly) think that a best estimate of the spectral index might be obtained by examining all of the measured ACE spectral indices and R_{corr} values and keeping only those spectral fits with the highest R_{corr} values, the

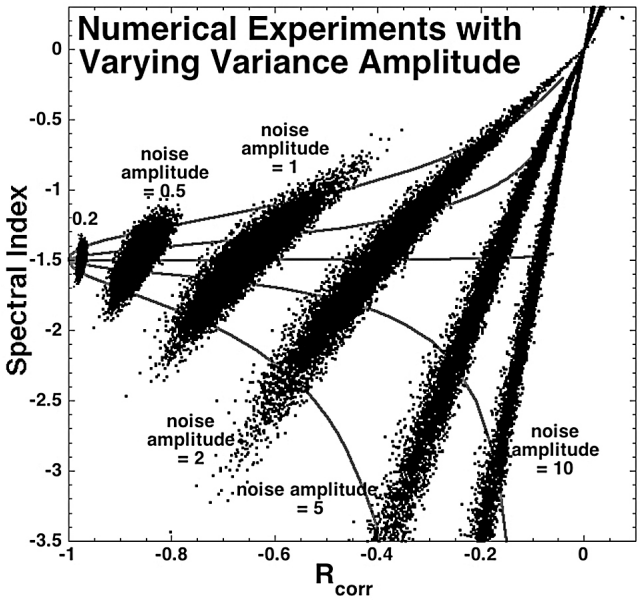

Figure A3. Similar to the ensemble of artificial PSD in Figure A2 (green points) six ensembles of a perfect −3/2 PSD plus noise are made and fit with a spectral index and correlation coefficient R_{corr}, which are plotted. Each ensemble has a different amplitude of noise (as labeled) and each ensemble has 10,000 PSDs. The five yellow curves of Figure A2 are replotted here in black.

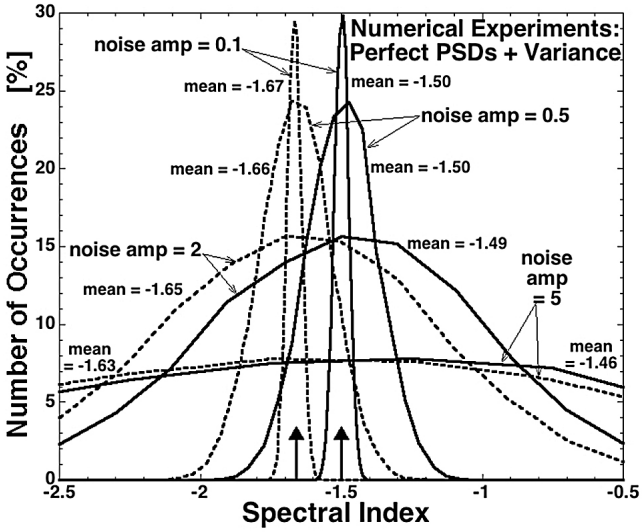

Figure A4. Two perfect PSDs, one with spectral index −3/2 and the other with spectral index −5/3, are created and noise with varying amplitudes is added to the perfect spectra. The spectral indices are determined and binned. Each distribution plotted is for an ensemble of 10,000 PSDs with the same noise amplitude (as labeled). The mean value of each distribution of spectral indices is indicated on the figure. Arrows in the bottom of the plot indicate the position of −5/3 and −3/2 spectral indices.

interpretation being that these spectra have "better fits." From what we know of the first numerical experiment (green points), that would very wrong: the correlation coefficients are higher because the noise adds to the spectral slopes, not because the underling spectral slopes are being found more clearly. If we made the mistake of only taking the "best fit" spectra (those with the highest R_{corr}), we would concentrate on the red and blue points at the bottom-left end of the diagonal bands of Figure A2. We would say "the best-fit spectral indices for the solar-wind turbulence are approximately −3."

[130] So how do we get the best estimate of the correct spectral index from the ensemble of ACE PSDs? The answer lies in Figure A4 and A5. In Figure A4 two perfect PSDs, one with spectral index −3/2 and the other with spectral index −5/3, are created and noise with varying amplitudes is added to the perfect spectra. The spectral indices are fit as usual, and the resulting indices are binned and the occurrence distributions are plotted in Figure A4. Each distribution is for an ensemble of 10,000 cases with the same noise amplitude. As can be seen by examining the various distributions, adding variance error does not skew the mean value of an ensemble of slopes away from the slope of the underlying perfect PSD. In Figure A5 the spectral indices of the energy spectra from ACE are binned and for comparison a distribution of −3/2 perfect spectra with variance error (red) and distribution of −5/3 perfect spectra with variance error (green) are also displayed. As can be seen, the all-data ACE distribution is very consistent with a −3/2 spectrum plus variance error. (The two distributions have an overlap of 92.3%.) The all-data distribution is less consistent with a −5/3 spectrum plus variance error (these two distributions have an overlap of 71.6%).

[131] Note from Figure A4 that the mean is preserved even while the spread of a distribution of measurements increases. Since we will identify the mean value as our measurement of the spectral index of the solar wind turbulence, the question to ask is: How accurate a representation to the true spectral index is the mean value obtained from N measurements? The answer will be that the mean value is much closer to the correct answer than one standard deviation of the measurements (i.e., the mean is determined to an accuracy much less

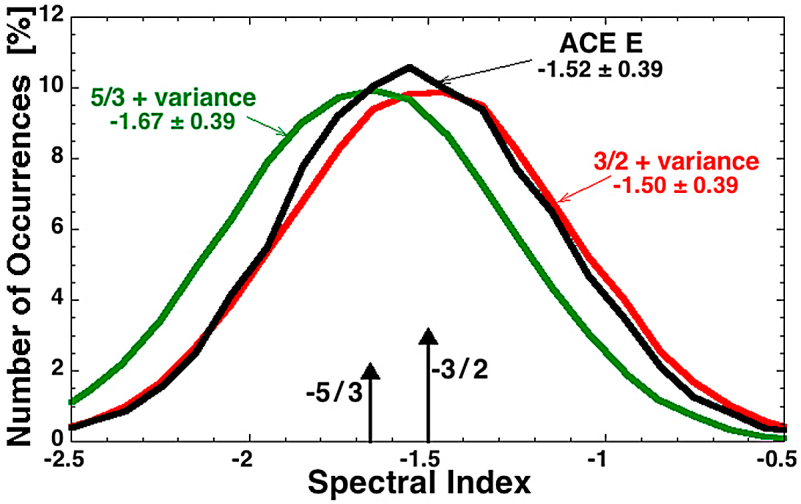

Figure A5. The spectral indices of the total energy PSDs from 1998 to 2008 ACE measurements are binned for all subintervals (dashed black curve) and for the directional-discontinuity-free ($N_d = 0$) subintervals (solid black curve). The spectral indices from an ensemble of 10,000 artificial PSDs formed by a −3/2 perfect spectra plus noise are binned (red curve) and the spectral indices from an ensemble of 10,000 artificial PSDs formed by a −5/3 perfect spectra plus noise are binned (green curve).

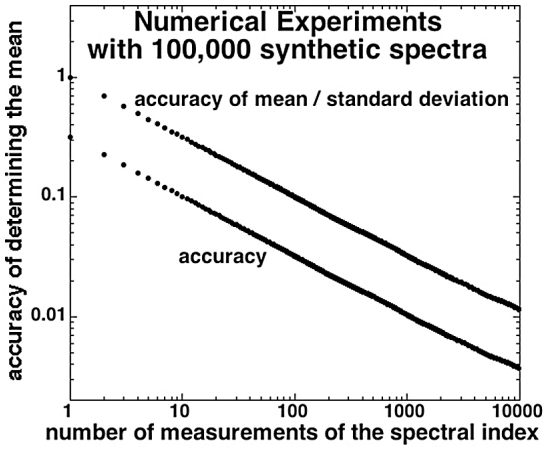

Figure A6. 100,000 artificial PSDs (perfect spectra plus noise) are created and each is fit to obtain a spectral index S. The 100,000 spectral indices are collected into groups of size N. For each group of N, the mean value of the spectral index S_m is calculated. These mean values S_m are then statistically analyzed and standard deviation of S_m is determined. This standard deviation is the accuracy that a given S_m value represents the underlying perfect spectral index; it is plotted as a function of the group size N (bottom points in the figure). It is replotted (top points) normalized to the standard deviation in measured values.

than the spread of the distribution). This is shown in Figure A6. To construct this figure a series of numerical experiments are performed, again involving perfect PSDs plus variance error. The perfect PSD has a slope of $-3/2$ and the noise amplitude is chosen as in the numerical-experiment distributions of Figure A5 that match the spread of the ACE measurements. A set of 100,000 synthetic PSDs (each one a perfect PSD plus noise) is created and each PSD is fit as usual to obtain 100,000 realizations of the spectral index S. The 100,000 spectral indices are collected into a large number of groups, each grouping having N spectral indices. For each group of N spectral indices, the mean value of the spectral index S_m is calculated. These mean values of the spectral index S_m are then statistically analyzed and the spread in the S_m values is determined (this spread is equal to the standard deviation of the S_m values). This spread is a measure of the accuracy that a given S_m value represents the underlying perfect spectral index. The accuracy is plotted as a function of the group size N in Figure A6 as the bottom set of points. This plotted accuracy pertains to PSDs with variance errors that are approximately equal to the variance errors in the ACE PSDs. The top set of points in Figure A6 is this accuracy normalized to the spread in measured values. As stated earlier, the accuracy by which the mean value represents the spectral index underlying the noise is considerably better than one standard deviation of the measured values of the spectral index. For example, with N = 1840 (the number of quality velocity PSDs for $N_d = 0$ from the 1998–2008 ACE data set) the mean value of the spectral indices is determined to an accuracy of ± 0.01, which is about 3% of the standard deviations of the spectral-index measurements.

[132] The analysis of this appendix has shown that the ensemble of total-energy spectral-index measurements from ACE is consistent with a $-3/2$ spectrum underlying random variance error. The conclusion attained from the analysis of this appendix is that the distribution of ACE spectral-index measurements supports a spectral index of $-3/2$ for the total-energy spectrum of the solar wind at 1 AU. Note however that there are systematic variations in the total-energy spectral index with the type of solar wind plasma.

Appendix B: Fast-Fourier-Transform Windowing

[133] When using fast Fourier transforms (FFTs) to analyze the ACE velocity and magnetic field measurements in this report, each data subinterval was detrended with a line prior to Fourier transforming. The purpose of this linear detrend is to eliminate the jump in the measurement value at the end of each 256-point data subinterval when the beginning and end of the data subinterval are matched together (with the implicit assumption that the 256-point data subinterval is periodic in order to apply Fourier-transform analysis). This sudden jump in the measurement value can introduce noise into the Fourier transform.

[134] Another method (besides linear detrend) to eliminate this periodicity jump would be to apply a data-tapering window to each data subinterval prior to Fourier transforming.

[135] To compare the two methodologies, the Fourier analysis of the 1998–2008 ACE data set is repeated a number of times using (a) no pre-processing of the data subintervals, (b) applying a linear detrend to each data subinterval prior to Fourier transforming, and (c) applying various data-tapering windows to the data subintervals prior to Fourier transforming. Note that when using multiplicative windows (method (c)) it is very important to subtract off the mean value of the function prior to applying the window, otherwise the window will transfer the power in the DC offset (which can be very large for v_r) into low-frequency Fourier components, making the spectrum erroneously steep. Methods (a) and (b) do not subtract off the mean value. Note that method (b) is an additive data modification and that method (c) is a multiplicative data modification. The shapes of the data-tapering windows used appear in Figure B1. The results of the repeated analyses appear in Figure B2 and in Table B1.

[136] The functional forms of the seven data-tapering windows used for the comparison are given in expressions (B1)–(B7) and the windows are plotted in Figure B1. Each data subinterval was 256 points long, with the data points equally spaced in time. The data points are labeled with integer j, with j varying from 1 to 256. The Gaussian window is a Gaussian notch with a half width of 20 points that spans the ends of the 256-point data subinterval:

$$w(j) = 1 - \exp\left(-((j-1)/20)^2\right) - \exp\left(-((257-j)/20)^2\right). \quad \text{(B1)}$$

The Gaussian window has the desirable properties that it has an infinite number of continuous derivatives [cf. *Hertweck and Schluter*, 1957; *Borovsky and Hansen*, 1991] and its Fourier transform is not a power law [cf. *International*

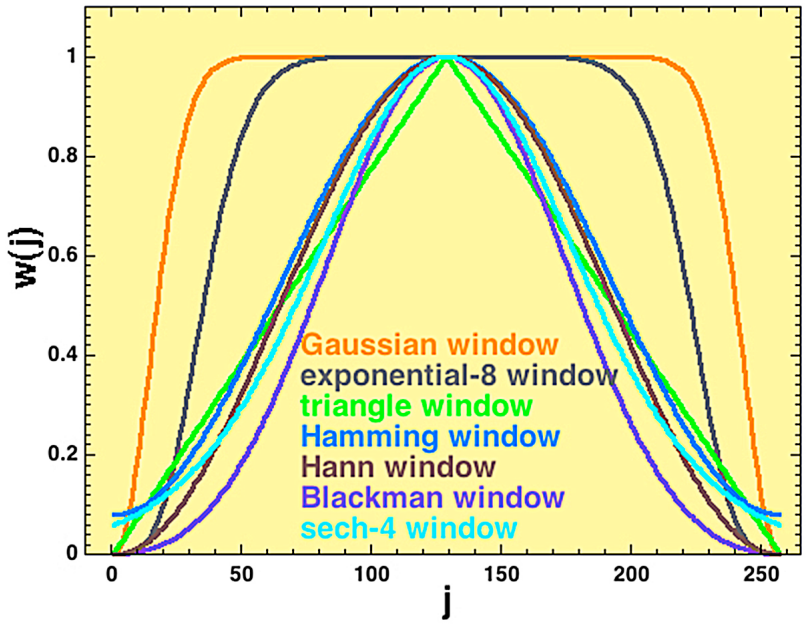

Figure B1. Seven data-tapering windows w that are used for pre-processing 256-point-long data intervals are plotted as a function of the data-point number j.

Telephone and Telegraph Corporation, 1979]. The exponential[8] window is

$$w(j) = \exp\left(-((j-129)/98)^8\right), \tag{B2}$$

which is flat for the central 3/4 of the data subinterval and rolls over smoothly toward zero at the ends. The triangular window (Bartlett window) is

$$\begin{aligned} w(j) &= 2(j-1)/256 \text{ for } 1 \le j \le 128 \\ w(j) &= 2 - 2(j-1)/256 \text{ for } 129 \le j \le 256. \end{aligned} \tag{B3}$$

The Hamming window is written

$$w(j) = 0.54 - 0.46\cos(\pi(j-1)/128) \tag{B4}$$

and the very-similar Hann window is given by

$$w(j) = 0.5 - 0.5\cos(\pi(j-1)/128). \tag{B5}$$

The Blackman window has the form

$$w(j) = 0.42 - 0.5\cos(\pi(j-1)/128) + 0.08\cos(\pi(j-1)/64) \tag{B6}$$

Finally, the sech[4] window is

$$w(j) = \mathrm{sech}^4((j-129)/96). \tag{B7}$$

For each methodology, 15,472 velocity data subintervals that are 256 points long and 20,076 magnetic field data subintervals that are 256 points long are used. For each data subinterval, the Fourier transforms of v_r, v_t, and v_n were used to construct a velocity power spectral density for the subinterval and the Fourier transforms of B_r, B_t, and B_n were used to construct a magnetic field power spectral density for the subinterval. The spectral indices of v and B were determined as usual (see section 2) by least squares linear-regression fitting of the power spectral densities. For each methodology, the 15,472 or 20,076 values of the spectral index of v and of B are then statistically analyzed.

[137] In Figure B2 the occurrence distributions of the spectral indices are plotted. The various colors are the

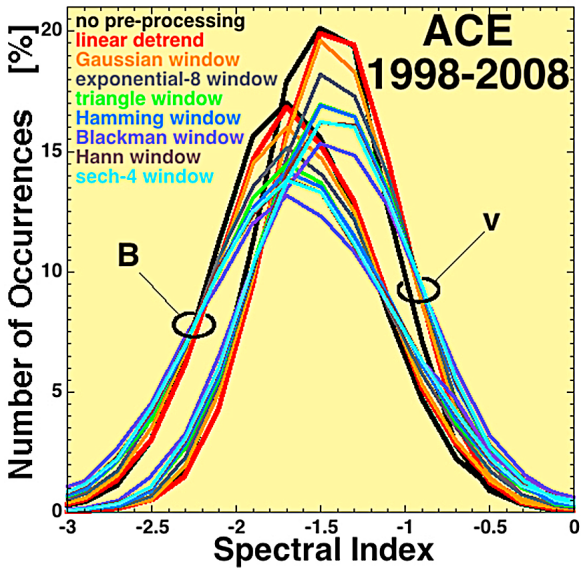

Figure B2. The occurrence distribution of the spectral index of the magnetic field power spectral density (left-hand curves) and of the velocity power spectral density (right-hand curves) are plotted. Each curve corresponds to 10292 values of the spectral index. The colors of the curves correspond to the data-analysis pre-processing method used. The ACE 1998–2008 measurements were used.

Table B1. The Median Values of the Spectral Indices and the Standard Deviations of the Spectral Indices Obtained by Fourier Analyzing the Velocity Fluctuations in 15,472 Subintervals and the Magnetic Field Fluctuations in 20,076 Subintervals of ACE Data Are Listed for Various Data Pre-processing Methods

Method of Data Pre-processing	v Mean ± Standard Deviation	B Mean ± Standard Deviation	v Spectral Index of Ensemble Average	B Spectral Index of Ensemble Average
No data preprocessing	−1.46 ± 0.38	−1.64 ± 0.47	−1.44	−1.64
Linear detrend	−1.41 ± 0.39	−1.62 ± 0.49	−1.40	−1.62
Gaussian window	−1.42 ± 0.41	−1.63 ± 0.51	−1.41	−1.63
Exponential[8] window	−1.42 ± 0.44	−1.63 ± 0.54	−1.41	−1.62
Triangle window	−1.41 ± 0.47	−1.62 ± 0.57	−1.41	−1.62
Hamming window	−1.41 ± 0.47	−1.62 ± 0.57	−1.41	−1.62
Hann window	−1.41 ± 0.49	−1.62 ± 0.59	−1.41	−1.62
Sech[4] window	−1.41 ± 0.49	−1.61 ± 0.59	−1.41	−1.62
Blackman window	−1.41 ± 0.52	−1.61 ± 0.63	−1.41	−1.62

distributions obtained from the various methodologies, with the color coding matching that in Figure B1. The leftmost set of curves in Figure B2 are the distributions of the spectral index of B and the rightmost set of curves are the distributions of the spectral index of v. As can be seen, the distributions with the narrowest spreads are those associated with no pre-processing of the data subintervals (black curves) and with linear detrending of the data (red curves). Applying windows to the data before Fourier transforming results in spectral-index distributions with more spread. This is interpreted as: windowing the data is adding noise (or reducing the signal to noise) to the measurement of the spectral index.

[138] In the first two columns of Table B1 the mean values and standard deviations of the spectral indices for v and B are listed for the various methodologies. As can be seen from the mean values, all of the methods are fairly consistent, except perhaps the "no data preprocessing" method that lead to spectral indices slightly steeper than the others. However, the filters tend to increase the standard deviation of the spectral indices, implying that they are adding noise to the spectral-index measurement. The methods are listed in Table B1 in order of ascending standard deviation. The "no data preprocessing" has the least spread, followed by the linear detrend, then by the Gaussian window with its continuous derivatives, finally by the other windows.

[139] For all the various methodologies the ensemble average of the 15,472 or 20,076 spectra are formed and power law fits to the ensemble-average spectra are made (as in Figure 6). In the last two columns of Table B1 these spectral indices are listed. As can be seen, the methods yield very similar spectral indices, except the "no data preprocessing" method which yields slightly steeper spectra.

[140] In summary, for the FFT analysis of the ACE data, utilizing data-tapering windows prior to Fourier transforming seems to weaken the signal-to-noise for the measurement of the spectral indices. The superior method appears to be using a linear detrend to the data subintervals.

[141] **Acknowledgments.** The author wishes to thank Mick Denton, Peter Gary, Sue Lepri, Bill Matthaeus, John Podesta, Aaron Roberts, Ruth Skoug, Chuck Smith, and John Steinberg for their assistance. This work was supported by the NASA Heliospheric SR&T Program, the NASA Heliospheric Guest-Investigator Program, by the NSF SHINE Program, and by the NASA Research in the Structure of the Solar Wind at 1 AU (RSSW@1AU) Program.

[142] Philippa Browning thanks the reviewers for their assistance in evaluating this paper.

References

Arge, C. N., and V. J. Pizzo (2000), Improvement in the prediction of solar wind conditions using near-real time solar magnetic field updates, *J. Geophys. Res.*, *105*, 10,465, doi:10.1029/1999JA000262.

Bavassano, B., and R. Bruno (1991), Solar wind fluctuations at large scale: A comparison between low and high solar activity conditions, *J. Geophys. Res.*, *96*, 1737, doi:10.1029/90JA01959.

Belcher, J. W., and L. Davis (1971), Large-amplitude Alfvén waves in the interplanetary medium, 2, *J. Geophys. Res.*, *76*, 3534, doi:10.1029/JA076i016p03534.

Belcher, J. W., and C. V. Solodyna (1975), Alfvén waves and directional discontinuities in the interplanetary medium, *J. Geophys. Res.*, *80*, 181, doi:10.1029/JA080i001p00181.

Bevington, P. R., and D. K. Robinson (1992), *Data Reduction and Error Analysis for the Physical Sciences*, 2nd ed., McGraw-Hill, New York.

Biskamp, D., and W.-C. Muller (2000), Scaling properties of three-dimensional magnetohydrodynamic turbulence, *Phys. Plasmas*, *7*, 4889, doi:10.1063/1.1322562.

Bloomfield, P. (1976), *Fourier Analysis of Time Series: An Introduction*, Wiley, New York.

Boldyrev, S. (2006), Spectrum of magnetohydrodynamic turbulence, *Phys. Rev. Lett.*, *96*, 115002, doi:10.1103/PhysRevLett.96.115002.

Boldyrev, S., J. C. Perez, J. E. Borovsky, and J. J. Podesta (2011), Spectral scaling laws in MHD turbulence simulations and in the solar wind, *Astrophys. J.*, *741*, L19, doi:10.1088/2041-8205/741/1/L19.

Borovsky, J. E. (2006), The eddy viscosity and flow properties of the solar wind: CIRs, CME sheaths, and solar-wind/magnetosphere coupling, *Phys. Plasmas*, *13*, 056505, doi:10.1063/1.2200308.

Borovsky, J. E. (2008), The flux tube texture of the solar wind: Strands of the magnetic carpet at 1 AU?, *J. Geophys. Res.*, *113*, A08110, doi:10.1029/2007JA012684.

Borovsky, J. E. (2010a), Contribution of strong discontinuities to the power spectrum of the solar wind, *Phys. Rev. Lett.*, *105*, 111102, doi:10.1103/PhysRevLett.105.111102.

Borovsky, J. E. (2010b), On the variations of the solar wind magnetic field about the Parker spiral direction, *J. Geophys. Res.*, *115*, A09101, doi:10.1029/2009JA015040.

Borovsky, J. E. (2012a), Looking for evidence of mixing in the solar wind from 0.31 to 0.98 AU, *J. Geophys. Res.*, doi:10.1029/2012JA017525, in press.

Borovsky, J. E. (2012b), The effect of sudden wind shear on the Earth's magnetosphere: Statistics of wind-shear events and CCMC simulations of magnetotail disconnections, *J. Geophys. Res.*, doi:10.1029/2012JA017623, in press.

Borovsky, J. E., and M. H. Denton (2010), Solar-wind turbulence and shear: A superposed-epoch analysis of corotating interaction regions at 1 AU, *J. Geophys. Res.*, *115*, A10101, doi:10.1029/2009JA014966.

Borovsky, J. E., and M. H. Denton (2011), No evidence for heating of the solar wind at strong current sheets, *Phys. Rev. Lett.*, *739*, L61.

Borovsky, J. E., and H. O. Funsten (2003a), Role of solar wind turbulence in the coupling of the solar wind to the Earth's magnetosphere, *J. Geophys. Res.*, *108*(A6), 1246, doi:10.1029/2002JA009601.

Borovsky, J. E., and H. O. Funsten (2003b), MHD turbulence in the Earth's plasma sheet: Dynamics, dissipation, and driving, *J. Geophys. Res.*, *108*(A7), 1284, doi:10.1029/2002JA009625.

Borovsky, J. E., and P. H. Hansen (1991), Breaking of the first adiabatic invariants of charged particles in time-dependent magnetic fields: Computer simulations and theory, *Phys. Rev. A*, *43*, 5605, doi:10.1103/PhysRevA.43.5605.

Borovsky, J. E., and J. T. Steinberg (2006a), The freestream turbulence effect in solar-wind/magnetosphere coupling: Analysis through the solar cycle and for various types of solar wind, in *Recurrent Magnetic Storms: Corotating Solar Wind Streams*, *Geophys. Monogr. Ser.*, vol. 167, edited by B. Tsurutani et al., pp. 59–76, AGU, Washington, D. C., doi:10.1029/167GM07.

Borovsky, J. E., and J. T. Steinberg (2006b), The "calm before the storm" in CIR/magnetosphere interactions: Occurrence statistics, solar-wind statistics, and magnetospheric preconditioning, *J. Geophys. Res.*, *111*, A07S10, doi:10.1029/2005JA011397.

Borovsky, J. E., R. C. Elphic, H. O. Funsten, and M. F. Thomsen (1997), The Earth's plasma sheet as a laboratory for flow turbulence in high-β MHD, *J. Plasma Phys.*, *57*, 1, doi:10.1017/S0022377896005259.

Borovsky, J. E., M. F. Thomsen, and R. C. Elphic (1998), The driving of the plasma sheet by the solar wind, *J. Geophys. Res.*, *103*, 17,617, doi:10.1029/97JA02986.

Brillinger, D. R. (1981), *Time Series Data Analysis and Theory*, McGraw-Hill, New York.

Bruno, R., and V. Carbone (2005), The solar wind as a turbulence laboratory, *Living Rev. Solar Phys.*, *2*, lrsp-2005-4.

Bruno, R., V. Carbone, P. Veltri, E. Pietropaolo, and B. Bavassano (2001), Identifying intermittency events in the solar wind, *Planet. Space Sci.*, *49*, 1201, doi:10.1016/S0032-0633(01)00061-7.

Bruno, R., R. D. D'Amicis, B. Bavassano, V. Carbone, and L. Sorriso-Valvo (2007), Magnetically dominated structures as an important component of the solar wind turbulence, *Ann. Geophys.*, *25*, 1913, doi:10.5194/angeo-25-1913-2007.

Burlaga, L. F. (1968), Micro-scale structures in the interplanetary medium, *Sol. Phys.*, *4*, 67, doi:10.1007/BF00146999.

Burlaga, L. F. (1969), Directional discontinuities in the interplanetary magnetic field, *Sol. Phys.*, *7*, 54, doi:10.1007/BF00148406.

Burlaga, L. F. (1971), Nature and origin of directional discontinuities in the solar wind, *J. Geophys. Res.*, *76*, 4360, doi:10.1029/JA076i019p04360.

Burlaga, L. F., and K. W. Ogilvie (1970), Magnetic and thermal pressures in the solar wind, *Sol. Phys.*, *15*, 61, doi:10.1007/BF00149472.

Burlaga, L. F., J. F. Lemaire, and J. M. Turner (1977), Interplanetary current sheets at 1 AU, *J. Geophys. Res.*, *82*, 3191, doi:10.1029/JA082i022p03191.

Cooley, J. W., and J. W. Tukey (1965), An algorithm for the machine calculation of complex Fourier series, *Math. Comput.*, *19*, 297, doi:10.1090/S0025-5718-1965-0178586-1.

Denskat, K. U., and L. F. Burlaga (1977), Multispecies observations of microscale fluctuations in the solar wind, *J. Geophys. Res.*, *82*, 2693, doi:10.1029/JA082i019p02693.

Denton, M. H., and J. E. Borovsky (2011), Magnetosphere response to high-speed solar-wind streams: A comparison of weak and strong driving and the importance of extended periods of fast solar wind, *J. Geophys. Res.*, *117*, A00L05, doi:10.1029/2011JA017124.

Elliott, H. A., D. J. McComas, N. A. Schwadron, J. T. Gosling, R. M. Skoug, G. Gloeckler, and T. H. Zurbuchen (2005), An improved expected temperature formula for identifying ICMEs, *J. Geophys. Res.*, *110*, A04103, doi:10.1029/2004JA010794.

Feldman, W. C., J. T. Gosling, D. J. McComas, and J. L. Phillips (1993), Evidence for ion jets in the high-speed solar wind, *J. Geophys. Res.*, *98*, 5593, doi:10.1029/92JA02260.

Feynman, J., A. A. Ruzmaikin, and E. J. Smith (1996), Radial evolution of the high/low frequency breakpoint in magnetic field spectra, *AIP Conf. Proc.*, *382*, 347, doi:10.1063/1.51409.

Fougere, P. F. (1985), On the accuracy of spectrum analysis of red noise processes using maximum entropy and periodogram methods: Simulation studies and application to geophysical data, *J. Geophys. Res.*, *90*, 4355, doi:10.1029/JA090iA05p04355.

Fyfe, D., D. Montgomery, and G. Joyce (1977), Dissipative, forced turbulence in two-dimensional magnetohydrodynamics, *J. Plasma Phys.*, *17*, 369, doi:10.1017/S0022377800020687.

Geiss, J., G. Gloeckler, and R. von Steiger (1995), Origin of solar wind from composition data, *Space Sci. Rev.*, *72*, 49, doi:10.1007/BF00768753.

George, W. K. (1978), Processing of random signals, in *Proceedings of the Dynamic Flow Conference 1978 on Dynamic Measurements in Unsteady Flows*, p. 757, Sijthoff and Noordhoff, Copenhagen, Denmark.

Gloeckler, G., et al. (1998), Investigation of the composition of solar and interstellar matter using solar wind and pickup ion measurements with SWICS and SWIMS on the ACE spacecraft, *Space Sci. Rev.*, *86*, 497, doi:10.1023/A:1005036131689.

Goldreich, P., and S. Sridhar (1997), Magnetohydrodynamic turbulence revisited, *Astrophys. J.*, *485*, 680, doi:10.1086/304442.

Grappin, R., A. Pouquet, and J. Leorat (1983), Dependence of MHD turbulence spectra on the velocity field-magnetic field correlation, *Astron. Astrophys.*, *126*, 51.

Grappin, R., M. Velli, and A. Mangeney (1991), "Alfvénic" versus "standard" turbulence in the solar wind, *Ann. Geophys.*, *9*, 416.

Greco, A., S. Servidio, W. H. Matthaeus, and P. Dmitruk (2010), Intermittent structures and magnetic discontinuities on small scales in MHD simulations and solar wind, *Planet. Space Sci.*, *58*, 1895, doi:10.1016/j.pss.2010.08.019.

Gulamali, M. Y., and P. J. Cargill (2001), Ulysses observations of magnetohydrodynamic turbulence in corotating interaction regions, *J. Geophys. Res.*, *106*, 15,687, doi:10.1029/2000JA000390.

Habbal, S. R., R. Woo, S. Fineschi, R. O'Neal, J. Kohl, G. Noci, and C. Korendyke (1997), Origins of the slow and the ubiquitous fast solar wind, *Astrophys. J.*, *489*, L103, doi:10.1086/310970.

Hamba, F. (1992), Turbulent dynamo effect and cross helicity in magnetohydrodynamic flows, *Phys. Fluids A*, *4*, 441, doi:10.1063/1.858314.

Harris, F. J. (1978), On the use of windows for harmonic analysis with the discrete Fourier transform, *Proc. IEEE*, *66*, 51, doi:10.1109/PROC.1978.10837.

Hatori, T. (1984), Kolmogorov-style argument for the decaying homogeneous MHD turbulence, *J. Phys. Soc. Jpn.*, *53*, 2539, doi:10.1143/JPSJ.53.2539.

Hausman, B. A., F. C. Michel, J. R. Espley, and P. A. Cloutier (2004), On determining the nature and orientation of magnetic directional discontinuities: Problems with the minimum variance method, *J. Geophys. Res.*, *109*, A11102, doi:10.1029/2004JA010670.

Hertweck, F., and A. Schluter (1957), Die "adiabatische Invarianz" des magnitischen Bahnmomentes gelander Teilchen, *Z. Naturforsch. B*, *12A*, 844.

Horbury, T. S., and J. M. Schmidt (1999), Development and effects of turbulence in connection with CIRs, *Space Sci. Rev.*, *89*, 61, doi:10.1023/A:1005260331464.

Horbury, T. S., D. Burgess, M. Franz, and C. J. Owen (2001), Three spacecraft observations of solar wind discontinuities, *Geophys. Res. Lett.*, *28*, 677, doi:10.1029/2000GL000121.

International Telephone and Telegraph Corporation (1979), *Reference Data for Radio Engineers*, Howard Sams, Indianapolis, Indiana.

Iroshnikov, P. S. (1964), Turbulence of a conducting fluid in a strong magnetic field, *Sov. Astron., Engl. Transl.*, *7*, 566.

Jenkins, G. M., and D. G. Watts (1968), *Spectral Analysis and Its Applications*, Holden-Day, San Francisco.

Johnstone, A. D., and I. C. Krauklis (1998), The effect of Poisson statistics on studies of turbulence in the solar wind, *J. Geophys. Res.*, *103*, 14,575, doi:10.1029/97JA02868.

Kaimal, J. C., S. F. Clifford, and R. J. Lataitis (1989), Effect of finite sampling on atmospheric spectra, *Boundary Layer Meteorol.*, *47*, 337, doi:10.1007/BF00122338.

Kay, S. M., and S. L. Marple (1981), Spectrum analysis–A modern perspective, *Proc. IEEE*, *69*, 1380, doi:10.1109/PROC.1981.12184.

Knetter, T., F. M. Neubauer, T. Horbury, and A. Balogh (2003), Discontinuity observations with Cluster, *Adv. Space Res.*, *32*(4), 543, doi:10.1016/S0273-1177(03)00335-1.

Knetter, T., F. M. Neubauer, T. Horbury, and A. Balogh (2004), Four-point discontinuity observations using Cluster magnetic field data: A statistical survey, *J. Geophys. Res.*, *109*, A06102, doi:10.1029/2003JA010099.

Kraichnan, R. H. (1965), Inertial-range spectrum of hydromagnetic turbulence, *Phys. Fluids*, *8*, 1385, doi:10.1063/1.1761412.

Li, G. (2007), Flux tubes in the fast and slow solar wind, *AIP Conf. Proc.*, *932*, 26, doi:10.1063/1.2778941.

Li, G. (2008), Identifying current-sheet-like structures in the solar wind, *Astrophys. J.*, *672*, L65, doi:10.1086/525847.

Li, G., E. Lee, and G. Parks (2008), Are there current-sheet-like structures in the Earth's magnetotail as in the solar wind–results and implications from high time resolution magnetic field measurements by Cluster, *Ann. Geophys.*, *26*, 1889, doi:10.5194/angeo-26-1889-2008.

Li, G., B. Miao, Q. Hu, and G. Qin (2011), Effect of current sheets on the solar wind magnetic field power spectrum from the Ulysses observations: From Kraichnan to Kolmogorov scaling, *Phys. Rev. Lett.*, *106*, 125001, doi:10.1103/PhysRevLett.106.125001.

Lopez, R. E. (1987), Solar cycle invariance in solar wind proton temperature relationships, *J. Geophys. Res.*, *92*, 11,189, doi:10.1029/JA092iA10p11189.

Malara, F., P. Veltri, and L. Primavera (1997), Nature of the density–magnetic-field-intensity correlation observed in the solar wind, *Phys. Rev. E*, *56*, 3508, doi:10.1103/PhysRevE.56.3508.

Mangeney, A., C. Salem, P. L. Veltri, and B. Cecconi (2001), Intermittency in the solar wind turbulence and the Haar wavelet transform, *Eur. Space Agency Spec. Publ.*, *ESA SP-492*, 53.

Manoharan, P. K., M. Kojima, N. Gopalswamy, T. Kondo, and Z. Smith (2000), Radial evolution and turbulence characteristics of a coronal mass ejection, *Astrophys. J.*, *530*, 1061, doi:10.1086/308378.

Mariani, F., B. Bavassano, U. Villante, and N. F. Ness (1973), Variations of the occurrence rate of discontinuities in the interplanetary magnetic field, *J. Geophys. Res.*, *78*, 8011, doi:10.1029/JA078i034p08011.

Mariani, F. B., B. Bavassano, and U. Villante (1983), A statistical study of MHD discontinuities in the inner solar system: Helios 1 and 2, *Sol. Phys.*, *83*, 349, doi:10.1007/BF00148285

Marple, S. L. (1987), *Digital Spectral Analysis*, Prentice Hall, Englewood Cliffs, N. J.

Marsch, E., and C.-Y. Tu (1990), On the radial evolution of MHD turbulence in the inner heliosphere, *J. Geophys. Res.*, *95*, 8211, doi:10.1029/JA095iA06p08211.

Matthaeus, W. H., and M. L. Goldstein (1982), Measurement of the rugged invariants of magnetohydrodynamic turbulence in the solar wind, *J. Geophys. Res.*, *87*, 6011, doi:10.1029/JA087iA08p06011.

Matthaeus, W. H., C. W. Smith, and J. W. Bieber (1999), Correlation lengths, the ultrascale, and the spatial structure of interplanetary turbulence, *AIP Conf. Proc.*, *471*, 511, doi:10.1063/1.58686.

McComas, D. J., S. J. Blame, P. Barker, W. C. Feldman, J. L. Phillips, P. Riley, and J. W. Griffee (1998), Solar Wind Electron Proton Alpha Monitor (SWEPAM) for the Advanced Composition Explorer, *Space Sci. Rev.*, *86*, 563, doi:10.1023/A:1005040232597.

Miao, B., B. Peng, and G. Li (2011), Current sheets from Ulysses observation, *Ann. Geophys.*, *29*, 237, doi:10.5194/angeo-29-237-2011.

Mininni, P. D., A. Alexakis, and A. Pouquet (2005), Shell to shell energy transfer in MHD, Part II: Kinematic dynamo, *Phys. Rev. E*, *72*, 046302, doi:10.1103/PhysRevE.72.046302.

Müller, W.-C., and R. Grappin (2005), Spectral energy dynamics in magnetohydrodynamic turbulence, *Phys. Rev. Lett.*, *95*, 114502, doi:10.1103/PhysRevLett.95.114502.

Mursula, K., and B. Zeiger (1996), The 13.5-day periodicity in the Sun, solar wind, and geomagnetic activity: The last three solar cycles, *J. Geophys. Res.*, *101*, 27,077, doi:10.1029/96JA02470.

Neugebauer, M. (1985), Alignment of velocity and field changes across tangential discontinuities in the solar wind, *J. Geophys. Res.*, *90*, 6627, doi:10.1029/JA090iA07p06627.

Neugebauer, M., and C. J. Alexander (1991), Shuffling foot points and magnetohydrodynamic discontinuities in the solar wind, *J. Geophys. Res.*, *96*, 9409, doi:10.1029/91JA00566.

Neugebauer, M., and J. Giacalone (2010), Progress in the study of interplanetary discontinuities, *AIP Conf. Proc.*, *1216*, 194, doi:10.1063/1.3395834.

Neugebauer, M., D. R. Clay, B. E. Goldstein, B. T. Tsurutani, and R. D. Zwickl (1984), A reexamination of rotational and tangential discontinuities in the solar wind, *J. Geophys. Res.*, *89*, 5395, doi:10.1029/JA089iA07p05395.

Neugebauer, M., C. J. Alexander, R. Schwenn, and A. K. Richter (1986), Tangential discontinuities in the solar wind: Correlated field and velocity changes and the Kelvin-Helmholz instability, *J. Geophys. Res.*, *91*, 13,694, doi:10.1029/JA091iA12p13694.

Ofman, L. (2004), The origin of the slow solar wind in coronal streamers, *Adv. Space Res.*, *33*, 681, doi:10.1016/S0273-1177(03)00235-7.

Otnes, R. K., and L. Enochson (1972), *Digital Time Series Analysis*, John Wiley, New York.

Owens, M. J., R. T. Wicks, and T. S. Horbury (2011), Magnetic discontinuities in the near-Earth solar wind: Evidence of in-transit turbulence or remnants of coronal structure?, *Sol. Phys.*, *269*, 411, doi:10.1007/s11207-010-9695-0.

Pagel, A. C., N. U. Crooker, T. H. Zurbuchen, and J. T. Gosling (2004), Correlation of solar wind entropy and oxygen ion charge state ratio, *J. Geophys. Res.*, *109*, A01113, doi:10.1029/2003JA010010.

Pallocchia, G., et al. (2002), Turbulence in the solar wind as seen by Cluster CIS experiment: Preliminary results of intermittency and scaling laws, *Eur. Space Agency Spec. Publ.*, *ESA SP-477*, 361.

Podesta, J. J. (2010), Theory of solar wind turbulence with scale-dependent alignment, anisotropy, and cross-helicity, *AIP Conf. Proc.*, *1216*, 115, doi:10.1063/1.3395814.

Podesta, J. J., and A. Bhattacharjee (2010), Theory of incompressible MHD turbulence with scale-dependent alignment and cross-helicity, *Astrophys. J.*, *718*, 1151, doi:10.1088/0004-637X/718/2/1151.

Podesta, J. J., and J. E. Borovsky (2010), Scale invariance of normalized cross-helicity in the inertial range of solar wind turbulence, *Phys. Plasmas*, *17*, 112905, doi:10.1063/1.3505092.

Podesta, J. J., D. A. Roberts, and M. L. Goldstein (2007), Spectral exponents of kinetic and magnetic energy spectra in solar wind turbulence, *Astrophys. J.*, *664*, 543, doi:10.1086/519211.

Reisenfeld, D. B., D. J. McComas, and J. T. Steinberg (1999), Evidence of a solar origin for pressure balance structures in the high-latitude solar wind, *Geophys. Res. Lett.*, *26*, 1805, doi:10.1029/1999GL900368.

Riazantseva, M. O., G. N. Zastenker, and J. D. Richardson (2005a), The characteristics of sharp (small-scale) boundaries of solar wind plasma and magnetic field structures, *Adv. Space Res.*, *35*, 2147, doi:10.1016/j.asr.2004.12.011.

Riazantseva, M. O., G. N. Zastenker, J. D. Richardson, and P. E. Eiges (2005b), Sharp boundaries of small- and middle-scale solar wind structures, *J. Geophys. Res.*, *110*, A12110, doi:10.1029/2005JA011307.

Richardson, I. G., and H. V. Cane (1995), Regions of abnormally low proton temperature in the solar wind (1965–1991) and their association with ejecta, *J. Geophys. Res.*, *100*, 23,397, doi:10.1029/95JA02684.

Roberts, D. A. (2010), The evolution of the spectrum of solar wind magnetic and velocity fluctuations from 0.3 to 5 AU, *J. Geophys. Res.*, *115*, A12101, doi:10.1029/2009JA015120.

Roberts, D. A., L. W. Klein, M. L. Goldstein, and W. H. Matthaeus (1987), Nature and evolution of magnetohydrodynamic fluctuations in the solar wind: Helios observations and Helios-Voyager comparisons, *J. Geophys. Res.*, *92*, 12,023, doi:10.1029/JA092iA11p12023.

Ruzmaikin, A., J. Feynman, and E. J. Smith (1997), Turbulence in coronal mass ejections, *J. Geophys. Res.*, *102*, 19,753, doi:10.1029/97JA01558.

Salem, C., A. Mangeney, S. D. Bale, and P. Veltri (2009), Solar wind magnetohydrodynamics turbulence: Anomalous scaling and role of intermittency, *Astrophys. J.*, *702*, 537, doi:10.1088/0004-637X/702/1/537.

Sari, J. W., and N. F. Ness (1969), Power spectra of the interplanetary magnetic field, *Sol. Phys.*, *8*, 155, doi:10.1007/BF00150667.

Schindler, K., and J. Birn (1978), Magnetospheric physics, *Phys. Rep.*, *47*, 109, doi:10.1016/0370-1573(78)90016-9.

Siscoe, G. L., L. Davis, P. J. Coleman, E. J. Smith, and D. E. Jones (1968), Power spectra and discontinuities of the interplanetary magnetic field: Mariner 4, *J. Geophys. Res.*, *73*, 61, doi:10.1029/JA073i001p00061.

Skoug, R. M., W. C. Feldman, J. T. Gosling, D. J. McComas, and C. W. Smith (2000), Solar wind electron characteristics inside and outside coronal mass ejections, *J. Geophys. Res.*, *105*, 23,069, doi:10.1029/2000JA000017.

Smith, C. W., M. H. Acuna, L. F. Burlaga, J. L'Heureux, N. F. Ness, and J. Scheifele (1998), The ACE Magnetic Fields Experiment, *Space Sci. Rev.*, *86*, 613, doi:10.1023/A:1005092216668.

Smith, C. W., K. Hamilton, B. J. Vasquez, and R. J. Leamon (2006), Dependence of the dissipation range spectrum of interplanetary magnetic fluctuations on the rate of energy cascade, *Astrophys. J.*, *645*, L85, doi:10.1086/506151.

Suess, S. T., Y.-K. Ko, R. von Steier, and R. L. Moore (2009), Quiescent current sheets in the solar wind and origins of slow wind, *J. Geophys. Res.*, *114*, A04103, doi:10.1029/2008JA013704.

Tessein, J. A., C. W. Smith, B. T. MacBride, W. H. Matthaeus, M. A. Forman, and J. E. Borovsky (2009), Spectral indices for multidimensional interplanetary turbulence at 1 AU, *Astrophys. J.*, *692*, 684, doi:10.1088/0004-637X/692/1/684.

Thieme, K. M., E. Marsch, and R. Schwenn (1988), Relationship between structures in the solar wind and their source regions in the corona, in *Proceedings of the Sixth International Solar Wind Conference*, edited by V. J. Pizzo, T. Holzer, and D. G. Sime, *Tech. Note NCAR/TN-306+STR*, p. 317, Natl. Cent. for Atmos. Res., Boulder, Colo.

Thieme, K. M., R. Schwenn, and E. Marsch (1989), Are structures in high-speed streams signatures of coronal fine structures?, *Adv. Space Res.*, *9*(4), 127, doi:10.1016/0273-1177(89)90105-1.

Thieme, K. M., E. Marsch, and R. Schwenn (1990), Spatial structures in high-speed streams as signatures of fine structures in coronal holes, *Ann. Geophys.*, *8*, 713.

Tripathi, L., A. K. Tiwari, and S. P. Agarwal (2007), Study of cosmic-ray intensity variations associated with anomalous, long-duration high-speed solar wind streams in 2003, *Sol. Phys.*, *241*, 171, doi:10.1007/s11207-006-0256-5.

Tsurutani, B. T., and C. M. Ho (1999), A review of discontinuities and Alfvén waves in interplanetary space: ULYSSES results, *Rev. Geophys.*, *37*, 517, doi:10.1029/1999RG900010.

Tsurutani, B. T., and E. J. Smith (1979), Interplanetary discontinuities: Temporal variations and the radial gradient from 1 to 8.5 AU, *J. Geophys. Res.*, *84*, 2773, doi:10.1029/JA084iA06p02773.

Tu, C.-Y., and E. Marsch (1990), Evidence for a "background" spectrum of solar wind turbulence in the inner heliosphere, *J. Geophys. Res.*, *95*, 4337, doi:10.1029/JA095iA04p04337.

Tu, C.-Y., and E. Marsch (1991), A case study of very low cross-helicity fluctuations in the solar wind, *Ann. Geophys.*, *9*, 319.

Tu, C.-Y., and E. Marsch (1994), On the nature of the compressive fluctuations in the solar wind, *J. Geophys. Res.*, *99*, 21,481, doi:10.1029/94JA00843.

Tu, C.-Y., and E. Marsch (1995a), MHD structures, waves and turbulence in the solar wind, *Space Sci. Rev.*, *73*, 1, doi:10.1007/BF00748891.

Tu, C.-Y., and E. Marsch (1995b), Comment on "Evolution of energy containing turbulent eddies in the solar wind" by W. H. Matthaeus, S. Oughton, D. H. Pontius Jr., and Y. Zhou, *J. Geophys. Res.*, *100*, 12,323, doi:10.1029/95JA01103.

Tu, C.-Y., E. Marsch, and K. M. Thieme (1989a), Basic properties of solar wind MHD turbulence near 0.3 AU analyzed by means of Elsasser variables, *J. Geophys. Res.*, *94*, 11,739, doi:10.1029/JA094iA09p11739.

Tu, C.-Y., D. A. Roberts, and M. L. Goldstein (1989b), Spectral evolution and cascade constant of solar wind Alfvénic turbulence, *J. Geophys. Res.*, *94*, 13,575, doi:10.1029/JA094iA10p13575.

Turner, J. M., and G. L. Siscoe (1971), Orientations of 'rotational' and 'tangential' discontinuities in the solar wind, *J. Geophys. Res.*, *76*, 1816, doi:10.1029/JA076i007p01816.

Vasquez, B. J., V. I. Abramenko, D. K. Haggerty, and C. W. Smith (2007), Numerous small magnetic field discontinuities of Bartels rotation 2286 and the potential role of Alfvénic turbulence, *J. Geophys. Res.*, *112*, A11102, doi:10.1029/2007JA012504.

Veltri, P. (1999), MHD turbulence in the solar wind: Self-similarity, intermittency and coherent structures, *Plasma Phys. Controlled Fusion*, *41*, A787, doi:10.1088/0741-3335/41/3A/071.

von Steiger, R., T. H. Zurbuchen, and D. J. McComas (2010), Oxygen flux in the solar wind: Ulysses observations, *Geophys. Res. Lett.*, *37*, L22101, doi:10.1029/2010GL045389.

Wang, Y.-M. (2011), Semiempirical models of the slow and fast solar wind, *Space Sci. Rev.*, doi:10.1007/s11214-010-9733-0, in press.

Wang, Y.-M., and N. R. Sheeley (2003), The solar wind and its magnetic sources at sunspot maximum, *Astrophys. J.*, *587*, 818, doi:10.1086/368302.

Welch, P. D. (1967), The use of fast Fourier transform for the estimation of power spectra: A method based on time averaging over short, modified periodograms, *IEEE Trans. Audio Electroacoust.*, *15*, 70, doi:10.1109/TAU.1967.1161901.

Wicks, R. T., M. J. Owens, and T. S. Horbury (2010), The variations of solar wind correlation lengths over three solar cycles, *Sol. Phys.*, *262*, 191, doi:10.1007/s11207-010-9509-4.

Williams, D. A. (1981), The analysis of random data, in *AGARD Flight Test Instrumentation Series*, vol. 14, edited by A. Pool and K. C. Sanderson, p. 1, Hartford House, London.

Woo, R., and S. R. Habbal (1998), Multiscale filamentary structures in the solar corona and their implications for the origin and evolution of the solar wind, *Phys. Space Plasmas*, *15*, 351.

Yamauchi, Y., S. T. Suess, and T. Sakurai (2002), Relation between pressure balance structures and polar plums from Ulysses high-latitude observations, *Geophys. Res. Lett.*, *29*(10), 1383, doi:10.1029/2001GL013820.

Yamauchi, Y., S. T. Suess, and T. Sakurai (2003), Relation between polar plums and fine structure in the solar wind from Ulysses high-latitude observations, *AIP Conf. Proc.*, *679*, 255, doi:10.1063/1.1618589.

Yordanova, E., A. Balogh, A. Nouyllez, and R. von Steiger (2009), Turbulence and intermittency in the heliospheric magnetic field in fast and slow wind, *J. Geophys. Res.*, *114*, A08101, doi:10.1029/2009JA014067.

Yoshizawa, A., and N. Yokoi (1996), Stationary large-scale magnetic fields generated by turbulent motion in a spherical region, *Phys. Plasmas*, *3*, 3604, doi:10.1063/1.871952.

Zank, G. P., W. H. Matthaeus, and L. W. Klein (1990), Temperature and density anti-correlations in solar-wind fluctuations, *Geophys. Res. Lett.*, *17*, 1239, doi:10.1029/GL017i009p01239.

Zhao, L., T. H. Zurbuchen, and L. A. Fisk (2009), Global distribution of the solar wind during solar cycle 23: ACE observations, *Geophys. Res. Lett.*, *36*, L14104, doi:10.1029/2009GL039181.

Zurbuchen, T. H., L. A. Fisk, G. Gloeckler, and R. von Steiger (2002), The solar wind composition through the solar cycle: A continuum of dynamic states, *Geophys. Res. Lett.*, *29*(9), 1352, doi:10.1029/2001GL013946.